Deutsches Zentrum
DLR für Luft- und Raumfahrt
Institut für
Vernetzte Energiesysteme

CARL
VON
OSSIETZKY
universität
OLDENBURG

Semi-empirical aging model for predicting the capacity loss of lithium-ion batteries in stationary storage systems

Von der Fakultät für Mathematik und Naturwissenschaften der Carl von Ossietzky Universität Oldenburg zur Erlangung des akademischen Grades eines Doktors der Naturwissenschaften (Dr. rer. nat.) angenommene Dissertation

von Frau

Amelie Krupp

1. Gutachter Professor Carsten Agert
Institut für Physik
Carl von Ossietzky Universität Oldenburg

2. Gutachter Professor Michael Wark
Institut für Chemie
Carl von Ossietzky Universität Oldenburg

Betreuer Professor Ernst Ferg and Dr. Robert Beckmann

May 29, 2023

Abstract

Predicting battery lifetime is essential for the safe, sustainable, and profitable operation of battery systems. Reducing the measurement and parameterization effort and increasing model accuracy and extrapolation capability are current challenges for efficient battery aging modeling. This thesis presents an innovative semi-empirical battery aging model and applies it to optimize the operation of a hybrid system providing frequency containment reserve. The system consists of a lithium-ion battery coupled with a power-to-heat module. The defined holistic model includes physically based calendar and cyclic model equations describing selected aging mechanisms at the graphite anode. A focus was set on improving the parameterization of the model equations to increase the model extrapolation capability. First, the influence of the characterization measurement was quantified and considered. Second, a multi-step parameterization method is introduced for the cyclic aging model based on identifying aging modes via incremental capacity analysis. The success of the targeted parameterization was approved, for example, in identifying various stress factor dependencies of individual aging mechanisms. The model's applicability to frequency containment reserve operation is validated on a dynamically aged cell with an application-related power profile. The economic analysis shows that operating the system at medium or high target state of charge and small to medium system sizes achieves the highest net present values. Furthermore, the battery lifetime is confirmed as the most critical factor influencing the system revenues at high FCR prices, which underlines the importance of optimizing operating strategies considering battery aging.

Kurzfassung

Die Vorhersage der Batterielebensdauer ist entscheidend für den sicheren, nachhaltigen und rentablen Betrieb von Batteriesystemen. Die Verringerung des Mess- und Parametrierungsaufwandes, sowie die Erhöhung der Modellgenauigkeit und der Extrapolationsfähigkeit sind aktuelle Herausforderungen für eine effiziente Modellierung der Batteriealterung. In dieser Arbeit wird ein innovatives semi-empirisches Batteriealterungsmodell vorgestellt und zur Optimierung des Betriebs eines Hybridsystems angewendet, welches Primärregelleistung erbringt. Das System besteht aus einer Lithium-Ionen-Batterie kombiniert mit einem Power-to-Heat-Modul. Das ganzheitliche Modell beinhaltet physikalisch basierte kalendarische und zyklische Modellgleichungen, die ausgewählte Alterungsmechanismen an der Graphitanode beschreiben. Zur Erhöhung der Extrapolationsfähigkeit des Modells wird ein Schwerpunkt auf die gezielte Parametrisierung der Modellgleichungen gelegt. Zunächst wird der Einfluss der Charakterisierungsmessung quantifiziert und berücksichtigt. Des Weiteren wird eine mehrstufige Parametrierungsmethode für das zyklische Alterungsmodell eingeführt, die auf der Identifikation von Alterungsmodi auf der Analyse der differenziellen Kapazität basiert. Der Erfolg der gezielten Parametrisierung wurde beispielsweise an der Identifikation verschiedener Stressfaktorabhängigkeiten einzelner Alterungsmechanismen bestätigt. Die Anwendbarkeit des Modells auf den Primärregelleistungsbetrieb wird an einer dynamisch mit einem anwendungsbezogenen Leistungsprofil gealterten Zelle validiert. Die wirtschaftliche Analyse zeigt, dass der Betrieb des Systems bei mittlerem oder hohem Zielladezustand und kleinen bis mittleren Batteriesystemgrößen die höchsten Kapitalwerte erzielt. Darüber hinaus wird bestätigt, dass die Batterielebensdauer der kritischste Faktor ist, der die Einnahmen bei hohen Primärregelleistungspreisen beeinflusst. Die Ergebnisse unterstreichen die Bedeutung der Optimierung von Betriebsstrategien unter Berücksichtigung der Batteriealterung.

Danksagung

Ich bedanke mich an dieser Stelle bei allen, die mich auf dem lehrreichen Weg der Promotion begleitet und unterstützt haben. Einige Personen, ohne die diese Arbeit in der hier vorliegenden Form nicht entstanden wäre, möchte ich im Folgenden direkt ansprechen.

Mein besonderer Dank gilt meiner Familie. Danke für euer bedingungsloses Vertrauen und die mentale Unterstützung. Allen voran danke ich meiner Großmutter Frau Dr. Marianne Krupp – du bist für mich ein besonderes Vorbild für Stärke und Willenskraft.

Die Promovierenden des Institutes für vernetzte Energiesysteme, die mit mir die Höhen und Tiefen der Promotionszeit durchlebt haben. Insbesondere Elena, Nailya, Stefan, Karo, Henning und Gerd. Dich Gerd habe ich, auch wenn du es nicht offiziell warst, immer als eine Art fachlichen Mentor betrachtet und geschätzt. Danke für die vielen unterhaltsamen und informativen Kaffeerunden und Diskussionen.

Den Laborleiter von E11 Leon Uhse, für die vielen belebten gemeinsamen Stunden im Labor. Weiterhin Karen Derendorf, die mich seit meiner Zeit als wissenschaftliche Hilfskraft im DLR als Batterie-Ansprechpartnerin begleitet hat. Es war mir jeden Tag eine große Freude mit euch ein Büro zu teilen!

Meinen Fachbetreuer Robert Beckmann, der viele Stunden geduldig zugehört und mit mir diskutiert hat, ohne jemals die Motivation zu verlieren. Ich habe viel von dir gelernt und die gemeinsame Arbeit war stets produktiv und unterhaltsam – danke dafür!

Mein Gruppenleiter Frank Schuldt. Danke für dein Vertrauen in meine Arbeit und die Förderung auch abseits des direkten Promotionskontextes.

Professor Ernst Ferg - Du hast meinen Forschergeist seit der Masterarbeit mit interessanten Diskussionen und Anstößen unterstützt, ob in Oldenburg oder aus Südafrika. Ich hoffe, dass wir auch zukünftig in gutem Kontakt bleiben.

Abschließend bedanke ich mich bei meinem Doktorvater und Erstgutachter Herrn Professor Carsten Agert, sowie bei Herrn Professor Michael Wark, als Zweitgutachter. Danke für die Ermöglichung dieser Dissertation und die stetige Unterstützung während der Bearbeitung.

Contents

Abbreviations

Abbreviation	Description
BESS	battery energy storage systems
CCCV	constant current constant voltage
CV	constant voltage
DV	differential voltage
EFC	equivalent full cycles
EoD	end of discharge
EoL	end of life
FCR	frequency containment reserve
FOI	features of interest
IC	incremental capacity
ICA	incremental capacity analysis
LAM	loss of active material
LLI	loss of lithium inventory
NMC	lithium nickel manganese cobalt oxide
NPV	net present value
OCV	open circuit voltage
PtH	power-to-heat
RES	renewable energy sources
RI	resistance increase
RPT	reference performance test
SEI	solid electrolyte interphase
SoC	state of charge
SoE	state of energy
TLC	taxes, levies, and charges
TSO	transmission grid operators
UC	under charge
UD	under discharge

1 Introduction

1.1 Motivation

To achieve the ambitious targets of the European Union towards a climate-neutral economy in 2050, measures including a transformation of the energy and transport sector are necessary [1]. Associated with this, the number of lithium-ion batteries used in stationary and mobile applications increased rapidly in the past few years. Germany's installed capacity in stationary large-scale storage systems supporting grid stability increased from about 50 MWh in 2015 to 1.2 GWh in 2022 [2]. The number of battery electric cars increased from 19,000 to 690,000 between 2015 and 2021 [3]. The European Union is investing heavily in research programs to promote the establishment of a sustainable and competitive European battery value chain, including battery production, use in an application, and recycling [4]. One essential strategic research goal is the development of simple and reliable methods to diagnose and predict battery aging, indicated by a change in battery capacity and internal resistance [5]. In research and development, the understanding of battery aging is used to develop improved battery technologies regarding safety, efficiency, and costs. Furthermore, predicting the battery lifetime is used to optimize operating strategies and system configurations or make a well-founded decision about maintenance and replacement intervals. Therefore, analyzing and forecasting battery aging is essential for increasing the economic and environmental profitability and safety of battery systems.

Methods of battery aging modeling include empirical approaches based purely on aging measurement data, physically based semi-empirical models, and detailed physical-electrochemical models. The method used determines parametrization effort, model accuracy, and needed computational capability. The semi-empirical approach chosen for this work offers the advantage of a lower computational demand than electrochemical models. Furthermore, physically based model equations make it parameterizable with less measurement effort and provide more extrapolation capability than purely empirical models [6, 7]. In the face of continuously evolving battery cell chemistries, battery aging models must be progressively extended and adapted. For battery storage operators that aim to improve their system design and

operation without having access to detailed cell internal properties, the need for efficient modeling methods that still provide sufficient accuracy is high. The cost and time efficiency of parameterization and the extrapolation capability are important model properties to be optimized.

An important application for stationary large-scale battery storage systems is frequency containment reserve (FCR) provision on the grid level [8, 9]. FCR is an ancillary service, that supports the integrity and stability of the power grid through frequency control [10]. The grid frequency fluctuates when there is a disbalance between generation and load in the interconnected grid. Systems that can ensure the grid frequency's maintenance through targeted energy consumption and release are, for example, pumped hydro storages, supercapacitors, compressed air energy storages, flywheels, sector coupling power-to-X solutions, or batteries. In recent years, the number of stationary battery storages in ancillary services increased rapidly. This can be attributed to their high efficiency, fast response time, flexible installation, and falling lithium-ion battery costs. Smaller home storage systems are primarily used to increase the self-consumption of photovoltaic energy. In the future, they could provide additional ancillary services as connected virtual plants. The digitalization required to control decentralized virtual plants is an important element in designing sustainable future energy systems [8, 10]. In addition, sector coupling, especially coupling the power and heat sector, has become a widely discussed topic [11, 12]. A possible sector coupling FCR system is the combination of a battery storage coupled with a power-to-heat module [13, 14]. The latter contributes to grid frequency maintenance by converting surplus electrical energy into thermal energy for district heating. The battery storage can provide positive and negative control power by storing and releasing energy.

In this work, an improved semi-empirical battery aging model is developed to model the capacity loss of graphite-based lithium-ion batteries in a stationary sector coupling FCR application. Thereby, the **main objectives** are the

1. development of new parameterization methods to reduce measurement effort and increase model accuracy.

2. development of model equations for the efficient description of graphite anode aging mechanisms in the calendar and cyclic battery aging.

3. assessment of the economic profitability of different operating strategies and system dimensions of a FCR battery storage system coupled with a power-to-heat module under consideration of battery aging.

The scientific contributions developed to achieve these goals were published in papers that are combined and framed in this cumulative dissertation. To clarify the contribution of this work, section 1.2 presents the current state of the art in semi-empirical battery aging modeling. Afterwards, the structure of the thesis, including introductory sections, scientific publications, and overall discussion, is explained in section 1.3.

1.2 State-of-the-art in battery aging modeling

Battery aging models can be divided into three categories: empirical, semi-empirical, and physical-electrochemical models. The latter are particularly suitable for understanding chemical and physical processes within the battery, from microscopic processes at the atomic level up to macroscopic interactions [15, 16]. Empirical models describe battery aging based purely on statistical description of measured data [17, 18]. This model category also includes machine learning-based approaches, which have been increasingly used in the recent years [19–21]. Semi-empirical models combine the aging measurement data based parameterization with simplified, physically based model approaches. They thus offer a higher extrapolation capability than empirical models and are computationally less complex than electrochemical models [6, 7]. These properties make them suitable for feasibility or cost analyses in industrial application areas where a potential new battery cell aging must be evaluated in a limited time with as little measurement and parameterization effort as possible. Furthermore, due to the low computational effort, they can be used for battery management system online aging evaluation [22, 23].

Semi-empirical models usually distinguish between calendar and cyclic aging. These are summed up according to the superposition approach to determine the total capacity loss. This procedure neglects the mutual interaction of calendar and cyclic aging mechanisms but significantly simplifies model development and parameterization and is, therefore, commonly applied [24]. Calendar aging models for graphite-based batteries mostly describe the dominant aging mechanism of SEI growth. The literature widely agrees on modeling the SEI growth temperature dependence using the Arrhenius equation [25–28]. The SEI formation rate increases with the battery SoC following the characteristics of the anode potential [28, 29], but is often empirically described [25, 27, 30]. There is a broad agreement about this simplified modeling of SEI- growth. In contrast, the efficient generation of parameterization data still poses a challenge. Capacity loss occurs only slowly during the battery's resting periods, so the calendar aging is usually accelerated at elevated temperatures and

then extrapolated to lower temperatures. Despite accelerated aging, calendar aging tests in the literature last one to two years [27, 28, 30]. Between the aging phases, characterization measurements are performed in which the battery is subjected to various reference performance tests (RPT). These provide additional battery aging by cyclization depending on the composition and frequency of the RPT, which differ significantly in different aging studies (see table 3.2). The influence of characterization measurement on calendar aging results is an open question, which is investigated in this thesis.

In cyclic aging, the possible aging mechanisms and their interaction become more diverse and complex. Aging model development faces the challenge of including as many stress factors and aging mechanisms as possible while keeping the model simple. Only a few models consider all the stress factors commonly used for cyclic aging, including temperature, current rate, average SoC, and DOD (see table 4.1). In literature models that accounted for all stress factors, the model equations were supplemented by empirical model equations without a physical background [31, 32]. On the other hand, exclusively physics-based models are limited in the number of stress factors included [33–35]. Another challenge is the targeted parameterization of the model equations. Different aging trends, which can roughly be divided into initial capacity gain and loss, followed by a stable irreversible capacity loss and finally rapid cell failure [36], should be assigned to their related aging mechanism model equations in the parameterization process. Schimpe et al. [37] differentiated between aging behavior at high and low temperatures and SoC but did not analyze the related aging mechanisms. The described challenges concerning cyclic aging modeling and model parameterization are addressed in this work by developing a physics-based aging model describing graphite anode aging mechanisms and a method for the targeted parameterization of the model equations based on ICA.

1.3 Outline

The thesis is structured as follows: First, the introductory chapter 2 provides important theoretical fundamentals regarding lithium-ion battery aging. It includes the general operating principle of lithium-ion batteries, important battery aging mechanisms and associated aging modes. The provided overview focuses on lithium-ion batteries with a graphite anode.

The scientific contributions to achieve the defined objectives of this thesis are divided into three sections, each published in a separate article. In the first two sections,

a holistic semi-empirical aging model was developed, including an independent calendar and cyclic model. They describe stress factor-dependent capacity loss due to graphite anode aging mechanisms. A comprehensive aging test series was carried out on NMC lithium-ion battery cells to parameterize the overall model. This included calendar and cyclic battery aging tests at constant stress factors and a regularly applied characterization measurement. The model was validated on a dynamic aging profile based on FCR operation. In the third section, the model was used in an economic dimension and operating strategy assessment of a sector coupling FCR system under consideration of battery aging. The content of the scientific contributions is described in more detail below.

Calendar aging model

Chapter 3 introduces the calendar aging model. It represents the aging mechanism of solid electrolyte interface (SEI) growth at varying battery temperatures and states of charge. In the model parameterization, the influence of the characterization measurement is quantified and explained. The correction of the characterization effects allows more accurate battery aging evaluation. It thus contributes to the first goal of the work - an increased accuracy of the model parameterized on measurement data. The main features of the related scientific work are summarized in Figure 1.1.

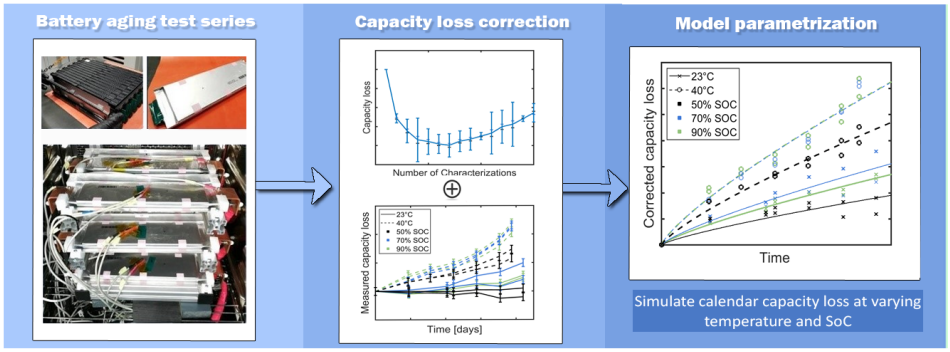

Figure 1.1: Calendar aging study structure including battery aging test series, characterization effect investigation and correction and parametrization of the SoC- and temperature-dependend capacity loss model. The graphical abstract is based on content from [38].

Cyclic aging model

Chapter 4 presents the developed innovative cyclic aging model, which describes the aging mechanisms SEI cracking and reforming and cracking of the anode active material. For its parametrization, a multi-step method is defined. First, active aging modes are analyzed using non-invasive incremental capacity analysis. The results are used to conclude the presence of the respective aging mechanism in the cyclic

aging tests. In the subsequent parameterization, only measurement data in which the aging mechanism modeled dominates were used. The holistic model capacity loss prognosis is validated on dynamic FCR aging data to ensure the transferability of the model results to the considered FCR application. Figure 1.2 shows the graphical abstract of the corresponding publication, which describes the model structure with input stress factors, represented aging mechanisms, associated aging modes, and output capacity loss. The scientific work contributes to each of the defined thesis objectives by defining an innovative model with an advanced parametrization method and validating the model results for the FCR use case as preparation for the economic system profitability assessment.

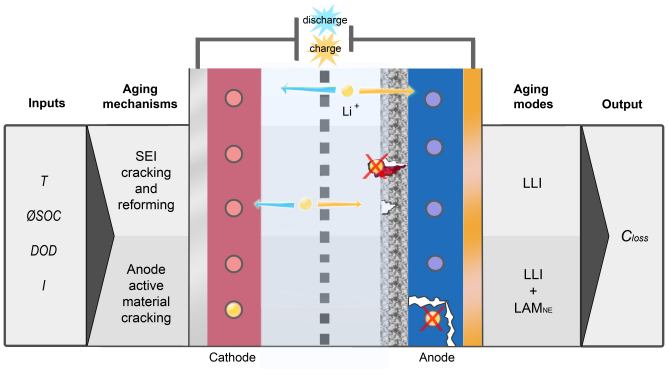

Figure 1.2: Structure of the cyclic aging model with input stress factors, described aging mechanisms, associated aging modes, and model output, published in [39].

Economic Assessment

In chapter 5 the aging model is used to optimize the storage dimension and operating strategy of a stationary, sector coupling FCR system. The system considered consists of a battery storage coupled with a power-to-heat module. Figure 1.3 shows the methodology used. It includes load simulation in FCR application, aging modeling, and a final economic analysis. The study assesses the economic profitability of the overall sector-coupled system, considering battery aging, which corresponds to the third thesis objective.

The results of the publications are summarized at the end of each chapter. The conclusion in chapter 6 presents the core results of the overall study. It contributes to the advancement of calendar and cyclic semi-empirical battery aging models and their parametrization, which are essential to meet the challenges of improving the usage and safety of future battery systems. Furthermore, concrete operating strategies of a stationary sector-coupling FCR storage system are introduced. The related outlook gives motivations for follow-up studies and further developments of the proposed semi-empirical aging model.

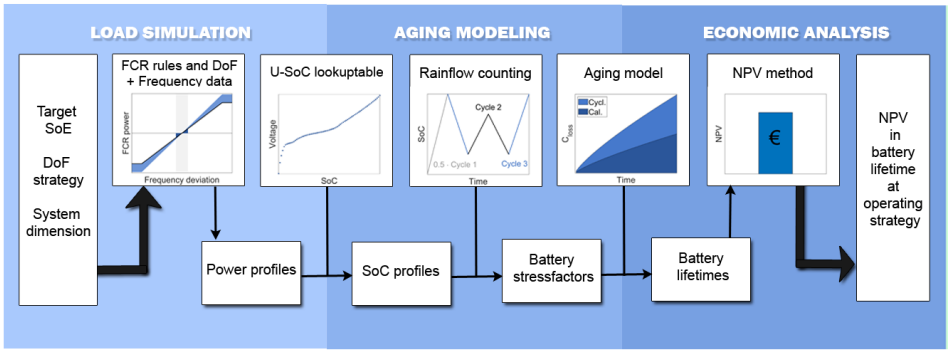

Figure 1.3: Methodology of economic assessment in different operation strategies and system dimensions of a stationary frequency containment reserve (FCR) storage considering battery aging. The load profile modeling considers the rules and degrees of freedom (DoF) of FCR generation. The net present value (NPV) is analyzed in the economic analysis as a measure of system profitability. The Graphical Abstract is taken from the related publication [].

References

[1] European Parliament. *Regulation (EU) 2021/1119 of the European Parliament and of the Council of 30 June 2021 establishing the framework for achieving climate neutrality and amending Regulations (EC) No 401/2009 and (EU) 2018/1999 ('European Climate Law')*. 2021. URL: https://eur-lex.europa.eu/legal-content/EN/TXT/?uri=CELEX:32021R1119 (visited on 10/21/2022).

[2] Jan Figgener et al. *The development of battery storage systems in Germany: A market review (status 2023)*. 2022. DOI: 10.48550/arXiv.2203.06762.

[3] International Energy Agency. "Global EV Outlook 2022: Securing supplies for an electric future". In: (2022).

[4] European Commission. *Horizon Europe Work Programme 2023-2024: 8. Climate, Energy and Mobility*. 2023.

[5] Batteries Europe WG6 ST3 et al. "ST3 Interoperable advanced BMS". In: *Roadmap on Stationary Applications for Batteries*, pp. 25–27.

[6] Xing Jin et al. "Applicability of available Li-ion battery degradation models for system and control algorithm design". In: *Control Engineering Practice* 71 (2018), pp. 1–9. ISSN: 09670661. DOI: 10.1016/j.conengprac.2017.10.002.

[7] Bolun Xu et al. "Modeling of Lithium-Ion Battery Degradation for Cell Life Assessment". In: *IEEE Transactions on Smart Grid* 9.2 (2018), pp. 1131–1140. ISSN: 1949-3053. DOI: 10.1109/TSG.2016.2578950.

[8] Jan Figgener et al. “The development of stationary battery storage systems in Germany – A market review”. In: *Journal of Energy Storage* 29 (2020), p. 101153. ISSN: 2352152X. DOI: 10.1016/j.est.2019.101153.

[9] Jan Figgener et al. “The influence of frequency containment reserve flexibilization on the economics of electric vehicle fleet operation”. In: *Journal of Energy Storage* 53 (2022), p. 105138. ISSN: 2352152X. DOI: 10.1016/j.est.2022.105138.

[10] Deutsche Energie-Agentur GmbH. *Systemsicherheit 2050: Systemdienstleistungen und Aspekte der Stabilität im zukünftigen Stromsystem*. 2020.

[11] Julien Garcia Arenas, Patrick Hendrick, and Pierre Henneaux. “Optimisation of Integrated Systems: The Potential of Power and Residential Heat Sectors Coupling in Decarbonisation Strategies”. In: *Energies* 15.7 (2022), p. 2638. DOI: 10.3390/en15072638.

[12] Jasmine Ramsebner et al. “The sector coupling concept: A critical review”. In: *WIREs Energy and Environment* 10.4 (2021). ISSN: 2041-8396. DOI: 10.1002/wene.396.

[13] Patrick Draheim et al. “Business case analysis of hybrid systems consisting of battery storage and power-to-heat on the German energy market”. In: *Utilities Policy* 67 (2020), p. 101110. ISSN: 09571787. DOI: 10.1016/j.jup.2020.101110.

[14] Alena Worschech et al. “Analysis of taxation and framework conditions for hybrid power plants consisting of battery storage and power-to-heat providing frequency containment reserve in selected European countries”. In: *Energy Strategy Reviews* 38 (2021), p. 100744. ISSN: 2211467X. DOI: 10.1016/j.esr.2021.100744.

[15] Xi Zhang et al. “A novel quantitative electrochemical aging model considering side reactions for lithium-ion batteries”. In: *Electrochimica Acta* 343 (2020), p. 136070. ISSN: 00134686. DOI: 10.1016/j.electacta.2020.136070.

[16] Lars von Kolzenberg, Arnulf Latz, and Birger Horstmann. “Solid-Electrolyte Interphase During Battery Cycling: Theory of Growth Regimes”. In: *cssc* (2020). DOI: 10.1002/cssc.202000867.

[17] Daniel Werner, Sabine Paarmann, and Thomas Wetzel. “Calendar Aging of Li-Ion Cells—Experimental Investigation and Empirical Correlation”. In: *Batteries* 7.2 (2021), p. 28. DOI: 10.3390/batteries7020028.

[18] Martin Petit, Eric Prada, and Valérie Sauvant-Moynot. “Development of an empirical aging model for Li-ion batteries and application to assess the impact of Vehicle-to-Grid strategies on battery lifetime”. In: *Applied Energy* 172 (2016), pp. 398–407. ISSN: 03062619. DOI: 10.1016/j.apenergy.2016.03.119.

[19] Bor-Rong Chen et al. “Battery aging mode identification across NMC compositions and designs using machine learning”. In: *Joule* 6.12 (2022), pp. 2776–2793. ISSN: 25424351. DOI: 10.1016/j.joule.2022.10.016.

[20] Xiaopeng Tang et al. “Recovering large-scale battery aging dataset with machine learning”. In: *Patterns (New York, N.Y.)* 2.8 (2021), p. 100302. DOI: 10.1016/j.patter.2021.100302.

[21] Shunli Wang et al. “A critical review of improved deep learning methods for the remaining useful life prediction of lithium-ion batteries”. In: *Energy Reports* 7 (2021), pp. 5562–5574. ISSN: 23524847. DOI: 10.1016/j.egyr.2021.08.182.

[22] Antoine Laurin, Vincent Heiries, and Maxime Montaru. “State-of-Charge and State-of-Health online estimation of Li-ion battery for the More Electrical Aircraft based on semi-empirical ageing model and Sigma-Point Kalman Filtering”. In: *2021 Smart Systems Integration (SSI)*. IEEE, 2021, pp. 1–4. ISBN: 978-1-6654-4092-9. DOI: 10.1109/SSI52265.2021.9466997.

[23] Xiaojuan Han, Zuran Wang, and Zixuan Wei. “A novel approach for health management online-monitoring of lithium-ion batteries based on model-data fusion”. In: *Applied Energy* 302 (2021), p. 117511. ISSN: 03062619. DOI: 10.1016/j.apenergy.2021.117511.

[24] Tanja Gewald et al. “Accelerated Aging Characterization of Lithium-ion Cells: Using Sensitivity Analysis to Identify the Stress Factors Relevant to Cyclic Aging”. In: *Batteries* 6.1 (2020), p. 6. DOI: 10.3390/batteries6010006.

[25] Madeleine Ecker et al. “Development of a lifetime prediction model for lithium-ion batteries based on extended accelerated aging test data”. In: *Journal of Power Sources* 215 (2012), pp. 248–257. ISSN: 03787753. DOI: 10.1016/j.jpowsour.2012.05.012.

[26] Sébastien Grolleau et al. “Calendar aging of commercial graphite/LiFePO4 cell – Predicting capacity fade under time dependent storage conditions”. In: *Journal of The Electrochemical Society* 255 (2014), pp. 450–458. ISSN: 0378-7753. DOI: 10.1016/j.jpowsour.2013.11.098.

[27] Severin Lukas Hahn et al. “Quantitative validation of calendar aging models for lithium-ion batteries”. In: *Journal of Power Sources* 400 (2018), pp. 402–414. ISSN: 03787753. DOI: 10.1016/j.jpowsour.2018.08.019.

[28] Björn Rumberg et al. “Holistic calendar aging model parametrization concept for lifetime prediction of graphite/NMC lithium-ion cells”. In: *Journal of Energy Storage* 30 (2020), p. 101510. ISSN: 2352152X. DOI: 10.1016/j.est.2020.101510.

[29] Peter Keil and Andreas Jossen. “Calendar Aging of NCA Lithium-Ion Batteries Investigated by Differential Voltage Analysis and Coulomb Tracking”. In: *Journal of The Electrochemical Society* 164.1 (2017), A6066–A6074. ISSN: 0378-7753. DOI: 10.1149/2.0091701jes.

[30] Johannes Schmalstieg et al. “A holistic aging model for Li(NiMnCo)O2 based 18650 lithium-ion batteries”. In: *Journal of Power Sources* 257 (2014), pp. 325–334. ISSN: 03787753. DOI: 10.1016/j.jpowsour.2014.02.012.

[31] Yingzhi Cui et al. “Multi-stress factor model for cycle lifetime prediction of lithium ion batteries with shallow-depth discharge”. In: *Journal of Power Sources* 279 (2015), pp. 123–132. ISSN: 03787753. DOI: 10.1016/j.jpowsour.2015.01.003.

[32] Md Sazzad Hosen et al. “Electro-aging model development of nickel-manganese-cobalt lithium-ion technology validated with light and heavy-duty real-life profiles”. In: *Journal of Energy Storage* 28 (2020), p. 101265. ISSN: 2352152X. DOI: 10.1016/j.est.2020.101265.

[33] Andrea Marongiu, Marco Roscher, and Dirk Uwe Sauer. “Influence of the vehicle-to-grid strategy on the aging behavior of lithium battery electric vehicles”. In: *Applied Energy* 137 (2015), pp. 899–912. ISSN: 03062619. DOI: 10.1016/j.apenergy.2014.06.063.

[34] Kandler Smith et al. “Comparison of Plug-In Hybrid Electric Vehicle Battery Life Across Geographies and Drive Cycles”. In: *SAE Technical Paper Series*. SAE Technical Paper Series. SAE International400 Commonwealth Drive, Warrendale, PA, United States, 2012. DOI: 10.4271/2012-01-0666.

[35] Alan Millner. “Modeling Lithium Ion battery degradation in electric vehicles”. In: *2010 IEEE Conference on Innovative Technologies for an Efficient and Reliable Electricity Supply*. IEEE, 27.09.2010 - 29.09.2010, pp. 349–356. ISBN: 978-1-4244-6076-2. DOI: 10.1109/CITRES.2010.5619782.

[36] R. Spotnitz. “Simulation of capacity fade in lithium-ion batteries”. In: *Journal of The Electrochemical Society* 113.1 (2003), pp. 72–80. ISSN: 0378-7753. DOI: 10.1016/S0378-7753(02)00490-1.

[37] M. Schimpe et al. “Comprehensive Modeling of Temperature-Dependent Degradation Mechanisms in Lithium Iron Phosphate Batteries”. In: *Journal of The Electrochemical Society* 165.2 (2018), A181–A193. ISSN: 0378-7753. DOI: 10.1149/2.1181714jes.

[38] Amelie Krupp et al. “Incremental Capacity Analysis as a State of Health Estimation Method for Lithium-Ion Battery Modules with Series-Connected Cells”. In: *Batteries* 7.1 (2021), p. 2. DOI: 10.3390/batteries7010002.

[39] Amelie Krupp et al. “Semi-empirical cyclic aging model for stationary storages based on graphite anode aging mechanisms”. In: *Journal of Power Sources* 561 (2023), p. 232721. ISSN: 03787753. DOI: 10.1016/j.jpowsour.2023.232721.

2 Fundamentals of Lithium-ion battery aging

During operation, the performance properties of the battery change, which is, in simplified terms, referred to as aging. Aging mechanisms, such as electrolyte decomposition or active material cracking, determine battery aging. According to the cause-effect principle, these lead to various aging modes, such as loss of lithium inventory, which in turn cause a change in cell capacity and available power. Understanding the battery aging model and the parameterization methods defined in this thesis requires knowledge of how the lithium-ion battery works, an insight into important aging mechanisms of the considered cell chemistry, and an overview of the associated aging modes and methods to identify them. The following chapter provides corresponding informations. Finally, it briefly reviews the state-of-the-art and current challenges in semi-empirical battery aging modeling.

2.1 Lithium-ion battery working principle

Lithium-ion batteries have a high energy density, long service life, and low self-discharge, which is why they are increasingly used in a wide range of applications. Furthermore, the cost of lithium-ion batteries has been progressively reduced, which is linked to the further development of high-volume production, improved module and cell concepts, and decreased raw material costs [1]. Widely used cathode materials in stationary and mobile applications today are lithium nickel manganese cobalt oxide (NMC), lithium nickel cobalt aluminum oxide (NCA), and lithium iron phosphate (LFP). The materials are typically combined with a graphite anode. Furthermore, the combination with lithium titanium oxide (LTO) anodes is used, especially for high-performance and high-safety applications [2–4]. Figure 2.1 shows a schematic illustration of a lithium-ion battery cell with graphite anode and layered transition metal oxide cathode.

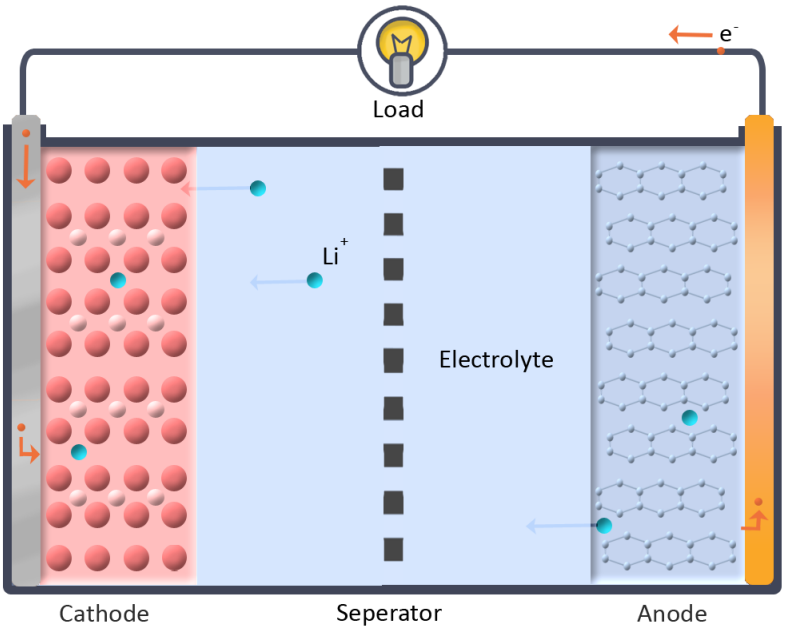

Figure 2.1: Schematic illustration of the lithium-ion battery components.

The lithium-ion battery consists of two electrodes in which lithium can be reversibly stored. They are electrically isolated from each other by a separator. An electrolyte allows the exchange of ions between the electrodes. The active electrode materials are deposited on current conductors, usually copper and aluminum foils, which are connected to an external conductor. As soon as electrical contact is created between the electrodes, lithium in the anode releases electrons in an oxidation reaction. This process is triggered by a difference in the electrochemical electrode potentials, which are connected to the electron energy in the material. The lithium-ions released pass through the electrolyte and intercalate into the cathode, which accepts the electrons from the external current path in a reduction reaction. The separation of oxidation and reduction enables the released electrical energy to be used by connected loads. The discharge process of the electrochemical cell ends as soon as the anode cannot provide more lithium-ions or the cathode is filled. When the battery is recharged, the reaction direction is reversed by applying an external potential. Chemically, in this case, the designations of the anode (site of oxidation) and cathode (site of reduction) change. However, historically, the electrodes in the field of batteries are consistently named after the discharge process [5, 6]. This nomenclature is adopted in this work.

2.2 Battery aging mechanisms

Depending on the cell chemistry and the aging stress factors in an application, various physical and chemical changes occur in lithium-ion battery components. These changes are called aging mechanisms. The following section introduces important aging mechanisms on different battery components. In the experimental work of this thesis, commercial NMC lithium-ion batteries are used. Accordingly, the overview focuses on NMC cathode and graphite anode electrode materials. Figure 2.2 gives an overview of the included aging mechanisms and an insight into their complex interaction.

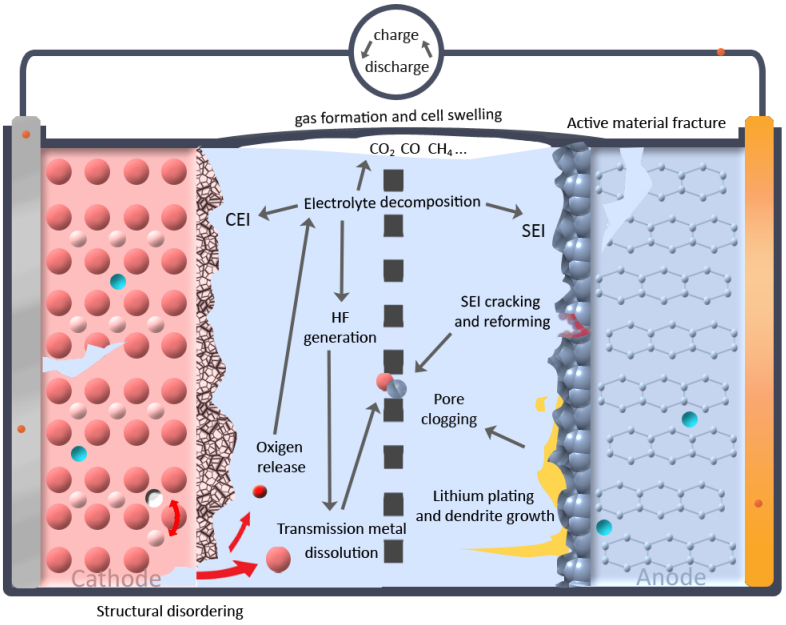

Figure 2.2: Illustration of selected aging mechanisms on lithium-ion battery components and parts of their interaction. Inspired by Birkl et al. [7].

2.2.1 Electrolyte

If the electrode surface potentials are outside the electrolyte's stability window, electrolyte decomposition reactions occur. The electrolyte in lithium-ion batteries usually consists of a solution of the conducting salt $LiPF_6$ in organic solvent mixtures, such as ethylene carbonate (EC) and dimethyl carbonate (DMC) [8]. Electrolyte reduction at the anode and oxidation at the cathode lead to surface layer formation and release of gases like CO, CO_2, and CH_4 [9, 10]. The stability and impedance of

the surface layers strongly depend on the electrolyte's composition. Therefore, it is modified with additives to influence the electrode layer structure and increase its ionic conductivity [11, 12]. The formation of the solid electrolyte interface (SEI) and cathode electrolyte interface (CEI), which lead to capacity loss and resistance increase, are described in detail in the associated electrode paragraphs. The consumption of electrolyte material in parasitic reactions additionally leads to the cells dry-out. Electrode sections are cut off from the electrolyte's ionic conduction, which decreases the electrode capacity and increases the current density for the remaining electrode area [13–15].

2.2.2 Graphite anode

The graphite anode has dominated the anode materials in lithium-ion batteries since their commercialization in 1991 [16]. Aging at the anode is determined by layer growth on the anode surface in the form of SEI and metallic lithium. Furthermore, mechanical stress leads to surface and active material cracking.

Active material cracking

In the graphite electrode, the carbon atoms form a planar network with hexagonal symmetry. Lithium can be reversibly intercalated between the superimposed graphite layers. The opening of the graphite layers occurs in several successive phase transitions, which are associated with a stepwise volume change of the anode. A total volume expansion of about 13% is observed in a complete charge or discharge cycle [17, 18]. The volume change causes mechanical stress in the active material and corresponding surface layer. Additionally, the formation of local mechanical stress due to lithium concentration gradients is favored at high lithium (de-)intercalation rates and low temperatures [19, 20]. Consequences include active material detachment of the current collector and cracking of active material and SEI on its surface. Without an intact passivating SEI, solvent co-intercalation can occur at the electrode surface, leading to graphite exfoliation. Active material isolated from the electric and ionic conduction no longer participates in cyclization and contributes to long-term capacity loss [21–23].

Solid electrolyte interface growth

At almost all battery SoC, the graphite anode potential lies below 1 V vs. Li/Li^+. This potential is outside the stability window of organic electrolytes. Therefore, reduction of the electrolyte occurs [12, 24]. The reduction products deposited on the anode surface form the SEI. It allows lithium-ions to pass but acts as an electrical insulator, which inhibits further electrolyte decomposition. The SEI is composed of a complex, multi-layered structure depending on the reactants contained in the electrolyte, the graphite anode surface area structure, and the formation conditions. In the widely accepted SEI mosaic structure, a distinction is made between an inner, compact layer of inorganic lithium compounds like Li_2O and LiF and an outer, more porous layer of organic components like semi-carbonates and polyolefins [12, 25–27].

In cell production, the initial SEI formation is systematically induced by slow charge and discharge cycles under controlled current densities, cutoff voltages, and temperatures to generate a stable and uniform SEI [12, 25, 26]. During the battery lifetime, it continues to grow. The SEI growth depends on cell temperature and anode potential in calendar aging [28, 29]. At cycling, the active material's volume change damages the SEI. The active material is exposed and new SEI is formed immediately [23, 30, 31]. The SEI growth mechanisms at cyclization may change from diffusion to migration limitation with increasing SEI thickness, as modeled by Kolzenberg et al. [32]. Also, the SEI growth and composition can be affected by dissoluted transition metals from the cathode (see section 2.2.3). The formation of the SEI layer, which is less permeable to lithium-ions than the electrolyte, increases the resistance of the battery. Furthermore, lithium is incorporated in the SEI layer, leading to capacity loss [12, 33].

Lithium plating

If the anode potential falls below 0 V vs. Li/Li^+, lithium deposits on the anode instead of intercalating. The fulfillment of this condition depends on the open circuit anode potential and the overvoltage, which is higher at charging with high current rates and at low temperatures [34, 35]. The deposition of metallic lithium on the anode is usually called lithium plating in the literature. Waldmann et al. [35] differentiate between the morphologies of the deposited lithium and only refer to the deposition of lithium as a homogeneous film as lithium plating. Deposited lithium is partly reversible and can dissolve (lithium stripping) and chemically intercalate into the graphite anode during a rest period or cycling after the plating process [36–38]. The residual metallic lithium reacts with the electrolyte, forming

new SEI. Furthermore, deposited lithium can lose contact with the anode. Both results in electrically isolated lithium that is no longer available for cyclization [35, 39]. Deposited lithium that forms dendrites can damage the separator and cause an internal short circuit followed by a thermal runaway. Therefore, uncontrolled lithium plating represents a high safety risk [34, 40].

2.2.3 NMC cathode

The $Li[Ni_{1-x-y}Co_xMn_y]O_2$ (NMC) cathode consists of a layered structure of mixed transition metal oxides. Between them, reversible lithium layers can form by changing the oxidation states of the transition metals. The nickel, manganese, and cobalt ratio determines electrode performance characteristics such as energy density, power density, and cycle life. A higher nickel content contributes significantly to the higher specific electrode capacity. Cobalt provides charge compensation at higher cathode potentials and reduces cation mixing and manganese stabilizes the lattice structure [41, 42]. Examples of commercialized compositions include NMC 111, NMC 523, and NMC 622 [43]. The mole fraction ratios of Ni, Mn, and Co indicated by the numbers may vary slightly depending on the manufacturer. The next-generation nickel-rich composition NMC 811 has an exceptionally high energy density and is considered to be cost-effective. However, the high nickel content is associated with accelerated battery aging [42, 44–47]. A summary of important NMC cathode aging mechanisms is given below.

Cracking and structural degradation

During battery discharging, lithium ions are inserted into the NMC interstitial sites. The oxidation states of the transition metals change, and the crystal structure expands continuously. The volume change is about 2% for NMC with low nickel content but increases with increasing nickel concentration [48, 49]. Expansion and contraction cause mechanical stress on the crystal lattice, which leads to inter- and intragranular active material fracture and particle disintegration in cyclic operation [44, 50]. Furthermore, the active material can transform irreversibly. For example, Ni^{2+} can enter the lithium layer of the delithiated cathode to reach a preferred thermodynamic energy state. This cation mixing and other multiple-step phase transitions lead to the formation of rock salt phases with poor ionic conductivity [44, 45, 51]. Each phase transformation relates to volume changes, leading to internal mechanical stresses and crack formation. The structural transformations

further include reactions releasing oxygen from the cathode lattice, increasingly for electrodes with higher nickel content [50, 52]. When the battery is overcharged, the NMC cathode collapses under the release of oxygen since a certain amount of lithium must always remain in the layered structure for stability. Released oxygen can oxidize the electrolyte leading to solvent decomposition and further degradation reactions [52, 53].

Transmission metal dissolution

Structural changes in the cathode and decomposition reactions in the electrolyte promote the dissolution of the transition metals nickel, manganese, and cobalt. Especially on cracked particles with a high surface area exposed to the electrolyte, the transition metals can separate from the cathode composite and dissolve in the electrolyte [54]. Transmission metal dissolution is triggered by the attack of hydrofluoric acid HF formed by decomposing the conductive salt $LiPF_6$ in a reaction with water. The water, in turn, mainly arises from reactions of electrolyte components with oxygen [45, 55]. Due to the dissolution of transition metals, active cathode material is lost. The released transmission metals can react with the electrolyte to form cathode electrolyte interface [56]. Furthermore, they can be transported to the anode, where they are incorporated into the SEI. A particularly increased lithium loss due to SEI growth is observed when Mn^{2+} is released [47, 57].

Cathode electrolyte interface

When the electrolyte is oxidized at the cathode, the CEI is formed. Analogous to the SEI it consists of an outer layer of predominantly organic components and an inorganic-rich inner layer [58, 59]. Oxidation of organic carbonate solvents, leading to CO_2, CO, and H_2O formation, is elevated at high temperatures and high cathode potentials [9, 60]. Furthermore, residual lithium compounds left over from battery synthesis, like Li_2O and Li_2CO_3, catalyze electrolyte reactions, especially in Ni-rich cathodes [45, 61]. Migration of SEI components can also contribute to CEI formation [62, 63]. In contrast to the SEI, no additional lithium is trapped in the CEI. Instead, CEI growth evokes lithium-ion intercalation into the cathode, leading to a drop in cathode potential [29, 64]. As a result, the maximum cell voltage is reached later at charging, and the amount of mobile lithium available at discharging is extended. Various calendar aging studies have already detected and discussed an associated capacity gain coupled with resistance increase due to CEI layer formation [28, 29].

2.2.4 Seperator

Various aging mechanisms were introduced in the previous subsections, including layer formation on the electrodes and cracking, restructuring, and dissolution of the electrode active materials. These processes release particles into the electrolyte that may clog the pores of the separator [56, 65]. Furthermore, the separator structure can change due to mechanical deformation at cyclization or thermal stress [66, 67]. Consequences are resistance increase, an uneven distribution of the current density in the cell (which in turn favors aging mechanisms like lithium plating [68]), and isolation of electrode active material area [66].

2.3 Battery aging modes

In the previous section, various possible lithium-ion battery aging mechanisms were introduced. Depending on cell chemistry and operating conditions, they cause a change in the battery performance indicators. Between the aging mechanisms and the measurable change in battery capacity and provided power, there is another level of abstraction: the aging modes. These include loss of lithium inventory (LLI) and loss of active material (LAM). The latter can be divided into four categories, depending on the electrode affected (anode/cathode) and the predominant degree of lithiation of the lost active material (lithiated/delithiated). Moreover, the resistance increase (RI) is considered as aging mode [69, 70]. For a more precise separation of capacity fade aging modes, Dubarry et al. [71] additionally defined under discharge (UD) and under charge (UC). These describe the capacity loss resulting from increased polarization resistance due to reaching the discharge and charge end voltages faster. Figure 2.3 shows an overview of possible stress factor-induced aging mechanisms and the linked fundamental aging modes LLI, LAM and RI.

To identify and quantify aging mechanisms, usually, post-mortem cell openings in combination with intensive physicochemical analyses (transmission electron microscopy, X-ray diffraction, chromatography, etc.) are necessary [24, 73]. In contrast, there are non-invasive methods to characterize active aging modes. These mainly rely on electrochemical impedance spectroscopy and quasi-open circuit voltage (OVC) measurements. The latter are evaluated regarding the differential voltage (DV) or incremental capacity (IC) [69, 74, 75]. The IC is defined by the derivative of the capacity dQ with respect to the voltage dV

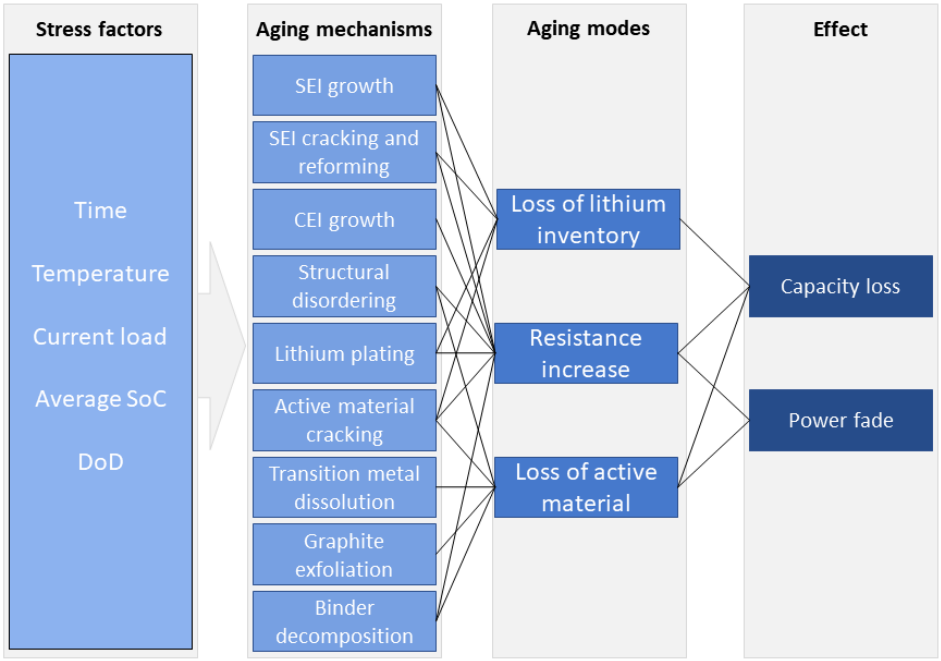

Figure 2.3: Aging modes connected to stressfactordependent aging mechanisms. Adapted from [7, 72].

$$IC = \frac{dQ}{dV} \approx \frac{\Delta Q}{\Delta V}. \tag{2.1}$$

In practical application, the increment of capacity ΔQ in a fixed voltage interval ΔV is used [76–78]. The IC curve shows voltage plateaus as peaks. These are associated with phase equilibria during intercalation and deintercalation of lithium in the anode and cathode and therefore indicate changes in cell chemistry and kinetics. If the electrochemical processes within the battery cell change due to aging, this can be seen in a shift in the height, area, and position of the IC peaks. The so-called features of interest (FOI) are used to conclude which aging modes were involved in the aging process. The peak area corresponds to the capacity charged or discharged in the associated voltage range. A smaller peak area can also implie a smaller peak height. Furthermore, the height decreases due to a peak broadening if the reaction kinetics within the cell slows down. A change in polarization resistance shifts the peaks to higher voltages during charging and lower voltages during discharging. The change in FOI with different aging modes is shown schematically in Figure 2.4 using a graphite-based LFP battery as an example. Due to the flat iron phosphate half-cell potential, the three shown prominent peaks are related to graphite anode's phase equilibria. The aging mode LLI results in a drop of the last IC peak at high cell voltages. If the cathode active material loss is limiting the cell capacity, LAM_{PE} could

also be detected as a decrease of the third peak. In contrast, LAM_{NE} results in a reduction of all peak areas. A detailed description of why the effects of the aging modes appear in this form is given in the intensive ICA study of Krupp et al. [79] that preceded this thesis. Additionally, the formation of the graphite anode peaks, mostly identifiable in the ICA of graphite-based lithium-ion batteries, is described in depth here. In the parameterization of the cyclic aging model of this thesis, the IC peak area evaluation is applied to separate the acting aging modes LLI and LAM and thus the expected associated aging mechanisms (see section 4).

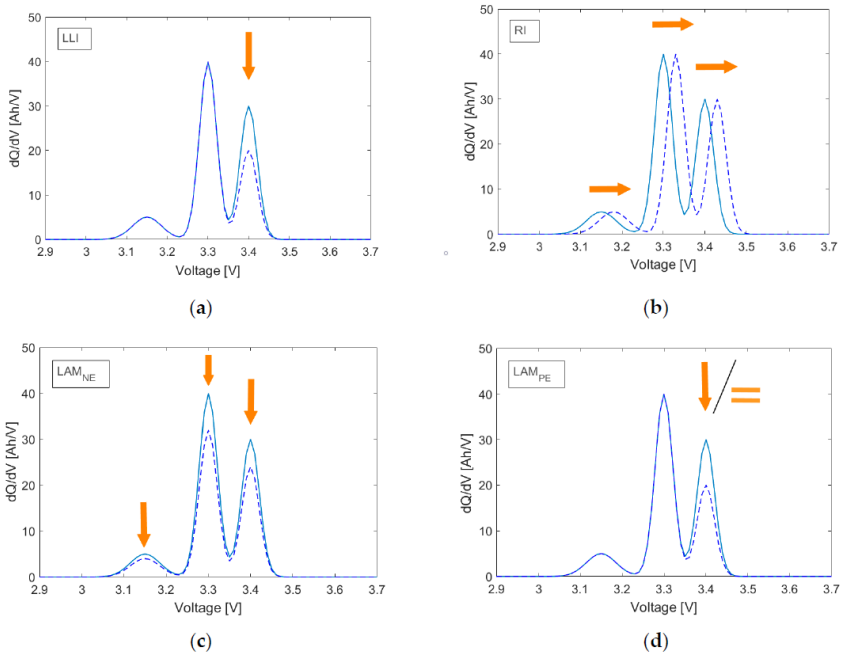

Figure 2.4: Shematic of the influence of loss of lithium inventory (LLI) (a), resistance increase (RI) (b), loss of active material at anode (LAM_{NE}) (c), and loss of active material at cathode (LAM_{PE}) (d) on the charge IC peaks of a LPF-graphite battery cell. Adopted from [79].

References

[1] Lukas Mauler et al. “Battery cost forecasting: a review of methods and results with an outlook to 2050”. In: *Energy & Environmental Science* 14.9 (2021), pp. 4712–4739. ISSN: 1754-5692. DOI: 10.1039/D1EE01530C.

[2] Nourhan Mohamed and Nageh K. Allam. “Recent advances in the design of cathode materials for Li-ion batteries”. In: *RSC Advances* 10.37 (2020), pp. 21662–21685. DOI: 10.1039/d0ra03314f.

[3] Hui Cheng et al. “Recent progress of advanced anode materials of lithium-ion batteries”. In: *Journal of Energy Chemistry* 57 (2021), pp. 451–468. ISSN: 20954956. DOI: 10.1016/j.jechem.2020.08.056.

[4] Yu Miao et al. “Current Li-Ion Battery Technologies in Electric Vehicles and Opportunities for Advancements”. In: *Energies* 12.6 (2019), p. 1074. DOI: 10.3390/en12061074.

[5] John Newman and Karen E. Thomas-Alyea. *Electrochemical systems*. 3. ed. Electrochemical Society series. Hoboken, NJ: Wiley-Interscience, 2004, p. 12. ISBN: 978-0471477563. URL: http://www.loc.gov/catdir/bios/wiley047/2004005207.html.

[6] Andreas Jossen and Wolfgang Weydanz. *Moderne Akkumulatoren richtig einsetzen*. 1. Auflage. Neusäß: Ubooks-Verlag, 2006, p. 100 et seqq. ISBN: 978-3939359111.

[7] Christoph R. Birkl et al. “Degradation diagnostics for lithium ion cells”. In: *Journal of Power Sources* 341 (2017), pp. 373–386. ISSN: 03787753. DOI: 10.1016/j.jpowsour.2016.12.011.

[8] Qingsong Wang et al. “Progress of enhancing the safety of lithium ion battery from the electrolyte aspect”. In: *Nano Energy* 55 (2019), pp. 93–114. ISSN: 22112855. DOI: 10.1016/j.nanoen.2018.10.035.

[9] Bernardine L. D. Rinkel et al. “Electrolyte Oxidation Pathways in Lithium-Ion Batteries”. In: *Journal of the American Chemical Society* 142.35 (2020), pp. 15058–15074. DOI: 10.1021/jacs.0c06363.

[10] Xin Teng et al. “In Situ Analysis of Gas Generation in Lithium-Ion Batteries with Different Carbonate-Based Electrolytes”. In: *ACS applied materials & interfaces* 7.41 (2015), pp. 22751–22755. DOI: 10.1021/acsami.5b08399.

[11] Xingwen Yu and Arumugam Manthiram. “Electrode–electrolyte interfaces in lithium-based batteries”. In: *Energy & Environmental Science* 11.3 (2018), pp. 527–543. ISSN: 1754-5692. DOI: 10.1039/c7ee02555f.

[12] Seong Jin An et al. “The state of understanding of the lithium-ion-battery graphite solid electrolyte interphase (SEI) and its relationship to formation cycling”. In: *Carbon* 105 (2016), pp. 52–76. ISSN: 00086223. DOI: 10.1016/j.carbon.2016.04.008.

[13] Christian Kupper et al. “End-of-Life Prediction of a Lithium-Ion Battery Cell Based on Mechanistic Aging Models of the Graphite Electrode”. In: *Journal of The Electrochemical Society* 165.14 (2018), A3468–A3480. ISSN: 0378-7753. DOI: 10.1149/2.0941814jes.

[14] Z. Mao et al. “Calendar Aging and Gas Generation in Commercial Graphite/NMC-LMO Lithium-Ion Pouch Cell”. In: *Journal of The Electrochemical Society* 164.14 (2017), A3469–A3483. ISSN: 0378-7753. DOI: 10.1149/2.0241714jes.

[15] Ruihe Li et al. “Modelling Solvent Consumption from SEI Layer Growth in Lithium-Ion Batteries”. In: *Journal of The Electrochemical Society* 169.6 (2022), p. 060516. ISSN: 0378-7753. DOI: 10.1149/1945-7111/ac6f84.

[16] Hao Zhang et al. “Graphite as anode materials: Fundamental mechanism, recent progress and advances”. In: *Energy Storage Materials* 36 (2021), pp. 147–170. ISSN: 24058297. DOI: 10.1016/j.ensm.2020.12.027.

[17] Simon Schweidler et al. “Volume Changes of Graphite Anodes Revisited: A Combined Operando X-ray Diffraction and In Situ Pressure Analysis Study”. In: *The Journal of Physical Chemistry C* 122.16 (2018), pp. 8829–8835. ISSN: 1932-7447. DOI: 10.1021/acs.jpcc.8b01873.

[18] J. R. Dahn. “Phase diagram of LixC6”. In: *Physical Review B* 44 (1991), pp. 9170–9177.

[19] Justin Purewal et al. “Degradation of lithium ion batteries employing graphite negatives and nickel–cobalt–manganese oxide + spinel manganese oxide positives: Part 2, chemical–mechanical degradation model”. In: *Journal of Power Sources* 272 (2014), pp. 1154–1161. ISSN: 03787753. DOI: 10.1016/j.jpowsour.2014.07.028.

[20] Kenji Takahashi and Venkat Srinivasan. “Examination of Graphite Particle Cracking as a Failure Mode in Lithium-Ion Batteries: A Model-Experimental Study”. In: *Journal of The Electrochemical Society* 162.4 (2015), A635–A645. ISSN: 0378-7753. DOI: 10.1149/2.0281504jes.

[21] Dietrich Goers et al. “The influence of the local current density on the electrochemical exfoliation of graphite in lithium-ion battery negative electrodes”. In: *Electrochimica Acta* 56.11 (2011), pp. 3799–3808. ISSN: 00134686. DOI: 10.1016/j.electacta.2011.02.046.

[22] Jia Guo et al. “Unravelling and quantifying the aging processes of commercial Li(Ni 0.5 Co 0.2 Mn 0.3)O 2 /graphite lithium-ion batteries under constant current cycling”. In: *Journal of Materials Chemistry A* 11.1 (2022), pp. 41–52. ISSN: 2050-7488. DOI: 10.1039/D2TA05960F.

[23] Josefine D. McBrayer et al. “Mechanical studies of the solid electrolyte interphase on anodes in lithium and lithium ion batteries”. In: *Nanotechnology* 32.50 (2021). DOI: 10.1088/1361-6528/ac17fe.

[24] Rui Xiong et al. “Lithium-ion battery aging mechanisms and diagnosis method for automotive applications: Recent advances and perspectives”. In: *Renewable and Sustainable Energy Reviews* 131 (2020), p. 110048. ISSN: 13640321. DOI: 10.1016/j.rser.2020.110048.

[25] Satu Kristiina Heiskanen, Jongjung Kim, and Brett L. Lucht. “Generation and Evolution of the Solid Electrolyte Interphase of Lithium-Ion Batteries”. In: *Joule* 3.10 (2019), pp. 2322–2333. ISSN: 25424351. DOI: 10.1016/j.joule.2019.08.018.

[26] E. Peled and S. Menkin. “Review—SEI: Past, Present and Future”. In: *Journal of The Electrochemical Society* 164.7 (2017), A1703–A1719. ISSN: 0378-7753. DOI: 10.1149/2.1441707jes.

[27] Aiping Wang et al. “Review on modeling of the anode solid electrolyte interphase (SEI) for lithium-ion batteries”. In: *npj Computational Materials* 4.1 (2018). DOI: 10.1038/s41524-018-0064-0.

[28] Björn Rumberg et al. “Holistic calendar aging model parametrization concept for lifetime prediction of graphite/NMC lithium-ion cells”. In: *Journal of Energy Storage* 30 (2020), p. 101510. ISSN: 2352152X. DOI: 10.1016/j.est.2020.101510.

[29] Peter Keil and Andreas Jossen. “Calendar Aging of NCA Lithium-Ion Batteries Investigated by Differential Voltage Analysis and Coulomb Tracking”. In: *Journal of The Electrochemical Society* 164.1 (2017), A6066–A6074. ISSN: 0378-7753. DOI: 10.1149/2.0091701jes.

[30] Izaro Laresgoiti et al. “Modeling mechanical degradation in lithium ion batteries during cycling: Solid electrolyte interphase fracture”. In: *Journal of Power Sources* 300 (2015), pp. 112–122. ISSN: 03787753. DOI: 10.1016/j.jpowsour.2015.09.033.

[31] Rutooj D. Deshpande and Dawn M. Bernardi. “Modeling Solid-Electrolyte Interphase (SEI) Fracture: Coupled Mechanical/Chemical Degradation of the Lithium Ion Battery”. In: *Journal of The Electrochemical Society* 164.2 (2017), A461–A474. ISSN: 0378-7753. DOI: 10.1149/2.0841702jes.

[32] Lars von Kolzenberg, Arnulf Latz, and Birger Horstmann. “Solid-Electrolyte Interphase During Battery Cycling: Theory of Growth Regimes”. In: *cssc* (2020). DOI: 10.1002/cssc.202000867.

[33] Yikang Yu et al. “Achieving SEI preformed graphite in flow cell to mitigate initial lithium loss”. In: *Carbon* 196 (2022), pp. 589–595. ISSN: 00086223. DOI: 10.1016/j.carbon.2022.05.024.

[34] Wenlong Cai et al. “The Boundary of Lithium Plating in Graphite Electrode for Safe Lithium-Ion Batteries”. In: *Angewandte Chemie (International ed. in English)* 60.23 (2021), pp. 13007–13012. DOI: 10.1002/anie.202102593.

[35] Thomas Waldmann, Björn-Ingo Hogg, and Margret Wohlfahrt-Mehrens. “Li plating as unwanted side reaction in commercial Li-ion cells – A review”. In: *Electrochemical and Solid-State Letters* 384 (2018), pp. 107–124. ISSN: 0378-7753. DOI: 10.1016/j.jpowsour.2018.02.063.

[36] Thomas Waldmann and Margret Wohlfahrt-Mehrens. “Effects of rest time after Li plating on safety behavior—ARC tests with commercial high-energy 18650 Li-ion cells”. In: *Electrochimica Acta* 230 (2017), pp. 454–460. ISSN: 00134686. DOI: 10.1016/j.electacta.2017.02.036.

[37] Simon Hein, Timo Danner, and Arnulf Latz. “An Electrochemical Model of Lithium Plating and Stripping in Lithium Ion Batteries”. In: *ACS Applied Energy Materials* 3.9 (2020), pp. 8519–8531. ISSN: 2574-0962. DOI: 10.1021/acsaem.0c01155.

[38] Mathias Petzl, Michael Kasper, and Michael A. Danzer. “Lithium plating in a commercial lithium-ion battery – A low-temperature aging study”. In: *Electrochemical and Solid-State Letters* 275 (2015), pp. 799–807. ISSN: 0378-7753. DOI: 10.1016/J.JPOWSOUR.2014.11.065.

[39] Xin-Bing Cheng et al. “Toward Safe Lithium Metal Anode in Rechargeable Batteries: A Review”. In: *Chemical reviews* 117.15 (2017), pp. 10403–10473. DOI: 10.1021/acs.chemrev.7b00115.

[40] Xiangwen Gao et al. “Thermodynamic Understanding of Li-Dendrite Formation”. In: *Joule* 4.9 (2020), pp. 1864–1879. ISSN: 25424351. DOI: 10.1016/j.joule.2020.06.016.

[41] O. Dolotko et al. “Understanding structural changes in NMC Li-ion cells by in situ neutron diffraction”. In: *Electrochemical and Solid-State Letters* 255 (2014), pp. 197–203. ISSN: 0378-7753. DOI: 10.1016/j.jpowsour.2014.01.010.

[42] Simon Schweidler et al. “Investigation into Mechanical Degradation and Fatigue of High-Ni NCM Cathode Material: A Long-Term Cycling Study of Full Cells”. In: *ACS Applied Energy Materials* 2.10 (2019), pp. 7375–7384. ISSN: 2574-0962. DOI: 10.1021/acsaem.9b01354.

[43] Xiaoqiao Zeng et al. “Commercialization of Lithium Battery Technologies for Electric Vehicles”. In: *Advanced Energy Materials* 9.27 (2019), p. 1900161. ISSN: 1614-6832. DOI: 10.1002/aenm.201900161.

[44] Chao Xu et al. “Phase Behavior during Electrochemical Cycling of Ni–Rich Cathode Materials for Li–Ion Batteries”. In: *Advanced Energy Materials* 11.7 (2021), p. 2003404. ISSN: 1614-6832. DOI: 10.1002/aenm.202003404.

[45] Philipp Teichert et al. “Degradation and Aging Routes of Ni-Rich Cathode Based Li-Ion Batteries”. In: *Batteries* 6.1 (2020), p. 8. DOI: 10.3390/batteries6010008.

[46] Tianyu Li et al. “Degradation Mechanisms and Mitigation Strategies of Nickel-Rich NMC-Based Lithium-Ion Batteries”. In: *Electrochemical Energy Reviews* 3.1 (2020), pp. 43–80. ISSN: 2520-8489. DOI: 10.1007/s41918-019-00053-3.

[47] Roland Jung et al. “Nickel, Manganese, and Cobalt Dissolution from Ni-Rich NMC and Their Effects on NMC622-Graphite Cells”. In: *Journal of The Electrochemical Society* 166.2 (2019), A378–A389. ISSN: 0378-7753. DOI: 10.1149/2.1151902jes.

[48] Aleksandr O. Kondrakov et al. “Anisotropic Lattice Strain and Mechanical Degradation of High- and Low-Nickel NCM Cathode Materials for Li-Ion Batteries”. In: *The Journal of Physical Chemistry C* 121.6 (2017), pp. 3286–3294. ISSN: 1932-7447. DOI: 10.1021/ACS.JPCC.6B12885.

[49] Lea de Biasi et al. “Between Scylla and Charybdis: Balancing Among Structural Stability and Energy Density of Layered NCM Cathode Materials for Advanced Lithium-Ion Batteries”. In: *The Journal of Physical Chemistry C* 121.47 (2017), pp. 26163–26171. ISSN: 1932-7447. DOI: 10.1021/acs.jpcc.7b06363.

[50] Soroosh Sharifi–Asl et al. “Oxygen Release Degradation in Li–Ion Battery Cathode Materials: Mechanisms and Mitigating Approaches”. In: *Advanced Energy Materials* 9.22 (2019), p. 1900551. ISSN: 1614-6832. DOI: 10.1002/aenm.201900551.

[51] Pengfei Yan et al. “Atomic Resolution Structural and Chemical Imaging Revealing the Sequential Migration of Ni, Co, and Mn upon the Battery Cycling of Layered Cathode”. In: *Nano letters* 17.6 (2017), pp. 3946–3951. DOI: 10.1021/acs.nanolett.7b01546.

[52] Roland Jung et al. “Oxygen Release and Its Effect on the Cycling Stability of LiNi x Mn y Co z O 2 (NMC) Cathode Materials for Li-Ion Batteries”. In: *Journal of The Electrochemical Society* 164.7 (2017), A1361–A1377. ISSN: 0378-7753. DOI: 10.1149/2.0021707jes.

[53] Naoaki Yabuuchi et al. “Detailed studies of a high-capacity electrode material for rechargeable batteries, Li2MnO3-LiCo(1/3)Ni(1/3)Mn(1/3)O2”. In: *Journal of the American Chemical Society* 133.12 (2011), pp. 4404–4419. DOI: 10.1021/ja108588y.

[54] Dong-Su Ko et al. “Microstructural visualization of compositional changes induced by transition metal dissolution in Ni-rich layered cathode materials by high-resolution particle analysis”. In: *Nano Energy* 56 (2019), pp. 434–442. ISSN: 22112855. DOI: 10.1016/j.nanoen.2018.11.046.

[55] Yonas Tesfamhret et al. “On the Manganese Dissolution Process from LiMn 2 O 4 Cathode Materials”. In: *ChemElectroChem* 8.8 (2021), pp. 1516–1523. ISSN: 2196-0216. DOI: 10.1002/celc.202001496.

[56] Jacqueline S. Edge et al. “Lithium ion battery degradation: what you need to know”. In: *Physical chemistry chemical physics : PCCP* 23.14 (2021), pp. 8200–8221. DOI: 10.1039/d1cp00359c.

[57] James A. Gilbert, Ilya A. Shkrob, and Daniel P. Abraham. “Transition Metal Dissolution, Ion Migration, Electrocatalytic Reduction and Capacity Loss in Lithium-Ion Full Cells”. In: *Journal of The Electrochemical Society* 164.2 (2017), A389–A399. ISSN: 0378-7753. DOI: 10.1149/2.1111702jes.

[58] Joshua P. Pender et al. “Electrode Degradation in Lithium-Ion Batteries”. In: *ACS nano* 14.2 (2020), pp. 1243–1295. DOI: 10.1021/acsnano.9b04365.

[59] K. Edström, T. Gustafsson, and J. O. Thomas. “The cathode–electrolyte interface in the Li-ion battery”. In: *Electrochimica Acta* 50.2-3 (2004), pp. 397–403. ISSN: 00134686. DOI: 10.1016/j.electacta.2004.03.049.

[60] Wesley M. Dose et al. “Electrolyte Reactivity at the Charged Ni-Rich Cathode Interface and Degradation in Li-Ion Batteries”. In: *ACS applied materials & interfaces* 14.11 (2022), pp. 13206–13222. DOI: 10.1021/acsami.1c22812.

[61] Yadong Wang, Junwei Jiang, and J. R. Dahn. “The reactivity of delithiated Li(Ni1/3Co1/3Mn1/3)O2, Li(Ni0.8Co0.15Al0.05)O2 or LiCoO2 with non-aqueous electrolyte”. In: *Electrochemistry Communications* 9.10 (2007), pp. 2534–2540. ISSN: 13882481. DOI: 10.1016/J.ELECOM.2007.07.033.

[62] Shuyu Fang et al. “Anode-originated SEI migration contributes to formation of cathode-electrolyte interphase layer”. In: *Electrochemical and Solid-State Letters* 373 (2018), pp. 184–192. ISSN: 0378-7753. DOI: 10.1016/j.jpowsour.2017.09.050.

[63] Jiagang Xu et al. “Electrode Side Reactions, Capacity Loss and Mechanical Degradation in Lithium-Ion Batteries”. In: *Journal of The Electrochemical Society* 162.10 (2015), A2026–A2035. ISSN: 0378-7753. DOI: 10.1149/2.0291510jes.

[64] N. N. Sinha et al. “The Use of Elevated Temperature Storage Experiments to Learn about Parasitic Reactions in Wound LiCoO2 Graphite Cells”. In: *Journal of The Electrochemical Society* 158.11 (2011), A1194. ISSN: 0378-7753. DOI: 10.1149/2.007111jes.

[65] X. Zhang, J. Zhu, and E. Sahraei. “Degradation of battery separators under charge–discharge cycles”. In: *RSC Advances* 7.88 (2017), pp. 56099–56107. DOI: 10.1039/c7ra11585g.

[66] Ao Li et al. “A Review on Lithium-Ion Battery Separators towards Enhanced Safety Performances and Modelling Approaches”. In: *Molecules (Basel, Switzerland)* 26.2 (2021). DOI: 10.3390/molecules26020478.

[67] Christina Peabody and Craig B. Arnold. “The role of mechanically induced separator creep in lithium-ion battery capacity fade”. In: *Electrochemical and Solid-State Letters* 196.19 (2011), pp. 8147–8153. ISSN: 0378-7753. DOI: 10.1016/j.jpowsour.2011.05.023.

[68] Xiao-Guang Yang et al. “Modeling of lithium plating induced aging of lithium-ion batteries: Transition from linear to nonlinear aging”. In: *Electrochemical and Solid-State Letters* 360 (2017), pp. 28–40. ISSN: 0378-7753. DOI: 10.1016/j.jpowsour.2017.05.110.

[69] Matthieu Dubarry, Cyril Truchot, and Bor Yann Liaw. “Synthesize battery degradation modes via a diagnostic and prognostic model”. In: *Electrochemical and Solid-State Letters* 219 (2012), pp. 204–216. ISSN: 0378-7753. DOI: 10.1016/j.jpowsour.2012.07.016.

[70] Anthony Barré et al. “A review on lithium-ion battery ageing mechanisms and estimations for automotive applications”. In: *Journal of The Electrochemical Society* 241 (2013), pp. 680–689. ISSN: 0378-7753. DOI: 10.1016/j.jpowsour.2013.05.040.

[71] Matthieu Dubarry et al. “Incremental Capacity Analysis and Close-to-Equilibrium OCV Measurements to Quantify Capacity Fade in Commercial Rechargeable Lithium Batteries”. In: *Electrochemical and Solid-State Letters* 9.10 (2006), A454. ISSN: 0378-7753. DOI: 10.1149/1.2221767.

[72] Wiljan Vermeer, Gautham Ram Chandra Mouli, and Pavol Bauer. “A Comprehensive Review on the Characteristics and Modeling of Lithium-Ion Battery Aging”. In: *IEEE Transactions on Transportation Electrification* 8.2 (2022), pp. 2205–2232. DOI: 10.1109/TTE.2021.3138357.

[73] Thomas Waldmann et al. “Review—Post-Mortem Analysis of Aged Lithium-Ion Batteries: Disassembly Methodology and Physico-Chemical Analysis Techniques”. In: *Journal of The Electrochemical Society* 163.10 (2016), A2149–A2164. ISSN: 0378-7753. DOI: 10.1149/2.1211609jes.

[74] Yang Gao et al. “The Mechanism and Characterization of Accelerated Capacity Deterioration for Lithium-Ion Battery with Li(NiMnCo) O 2 Cathode”. In: *Journal of The Electrochemical Society* 166.8 (2019), A1623–A1635. ISSN: 0378-7753. DOI: 10.1149/2.1001908jes.

[75] David Ansean et al. “Lithium-Ion Battery Degradation Indicators Via Incremental Capacity Analysis”. In: *IEEE Transactions on Industry Applications* 55.3 (2019), pp. 2992–3002. ISSN: 0093-9994. DOI: 10.1109/TIA.2019.2891213.

[76] Linfeng Zheng et al. “Incremental capacity analysis and differential voltage analysis based state of charge and capacity estimation for lithium-ion batteries”. In: *Energy* 150 (2018), pp. 759–769. ISSN: 03605442. DOI: 10.1016/j.energy.2018.03.023.

[77] Caihao Weng et al. “State-of-health monitoring of lithium-ion battery modules and packs via incremental capacity peak tracking”. In: *Applied Energy* 180 (2016), pp. 360–368. ISSN: 03062619. DOI: 10.1016/j.apenergy.2016.07.126.

[78] Zhongkai Zhou et al. “Practical State of Health Estimation for LiFePO 4 Batteries Based on Gaussian Mixture Regression and Incremental Capacity Analysis”. In: *IEEE Transactions on Industrial Electronics* 70.3 (2023), pp. 2576–2585. ISSN: 0278-0046. DOI: 10.1109/TIE.2022.3167142.

[79] Amelie Krupp et al. “Incremental Capacity Analysis as a State of Health Estimation Method for Lithium-Ion Battery Modules with Series-Connected Cells”. In: *Batteries* 7.1 (2021), p. 2. DOI: 10.3390/batteries7010002.

3 Calendar aging model

This chapter is based on the publication „Calendar Aging Model for Lithium-Ion Batteries Considering the Influence of Cell Characterization“ by Amelie Krupp, Robert Beckmann, Theys Diekmann, Ernst Ferg, Frank Schuldt, and Carsten Agert [1]. It includes minor changes compared to the original, for example, the adaptation of the headings in terms of the overall thesis structure. The use of the article in the thesis for non comercial purposes is permitted by the publisher Elsevier.

Abstract

To optimize costs and ensure safety, investigation and modeling of battery aging is very important. Calendar aging analysis consist of a periodic sequence of calendar aging and cell characterization. The influence of the characterization on the results of the calendar aging investigation has been assumed to be negligible so far. Nevertheless, the characterization measurements of different studies, especially the important capacity measurement, differ fundamentally. This could have an impact on the results of capacity and resistance change in calendar aging. In this paper, the effect of characterization is quantified for the first time, using periodic characterization measurements. A significant influence in the form of capacity increase and resistance decrease is found. It can be explained by an increase in the active electrode surface area caused by the characterization measurement. Therefore, the cell characterization is a new possible source for capacity increase in calendar aging. As an important result, in future studies capacity measurements should be performed with small currents below 1C to reduce the influence of characterization on the results. Additionally, a correction of the characterization effect can be done according to the presented method.

3.1 Introduction

Diagnosis and prognosis of battery aging is essential not only to ensure safety but also to optimize profitability of battery storage systems. Battery aging can be detected by a decrease in capacity and an increase in internal resistance. In aging models, a distinction is made between calendar aging during rest times of the battery and cyclic aging due to cyclization.

Many approaches exist for modeling battery aging. Theoretical models calculate the aging of batteries based on physical relationships. The model scale varies from macro- to micro-scale, including the modeling of processes at the atomic level. Since a wide variety of aging mechanisms influence the battery aging, these models quickly become complex and require high computing effort. They are particularly suitable for understanding chemical and physical processes within the battery cell. In contrast to that, empirical models are based on a statistical description of measured data. There is no need for knowledge of the processes taking place in the cell. They are usually related to a specific application and limited by the experimental data, which results in a considerable measurement effort. Semi-empirical models represent a hybrid form of these approaches. The model equations are based on theoretical relationships and are parameterized using empirical measurement data. They offer the advantage of lower computational effort and easier parameterization compared to theoretical models. Furthermore, due to the physical background, they can be better extrapolated and require less measurement effort than empirical models [2–4].

In applications with many rest periods or predominant cyclization with small currents and small depth of discharge, the analysis of calendar aging is particularly important. A wide variety of model approaches can be found to describe calendar aging. A literature review on the cell chemistry and target values considered in different semi-empirical aging models is provided in Table 1. It is to be noted that many of the publications included model not only calendar but also cyclic aging, which is not listed separately.

3.1.1 Battery cell characterization tests

Calendar aging measurements are used to parametrize semi-empirical models. They consist of a periodic sequence of a calendar aging step and a characterization measurement. Battery cell characterization usually includes a capacity measurement and a pulse test, to determine the cells capacity C and resistance R. Optionally, other

Source	Cell Chemistry	Target Value	
		C	R
Baghdadi et al. 2016 [5]	NCA, NMC	x	x
Ecker et al. 2012 [6]	NMC	x	x
Grolleau et al. 2014 [7]	LFP	x	-
Hahn et al. 2018 [8]	NMC	x	-
Hoog et al. 2017 [9]	NMC	x	-
Marongiu et al. 2015 [10]	NMC, LFP	x	x
Naumann et al. 2018 [11]	LFP	x	x
Rumberg et al. 2020 [12]	NMC	x	x
Schmalstieg et al. 2014 [2]	NMC	x	x
Smith et al., 2012 [13]	NCA	x	x
Xu et al. 2018 [4]	LMO, LFP, NMC	x	-

Table 3.1: Literature review on cell chemistry and target value (capacity C and resistance R) of semi-empirical calendar aging models.

supplementary measurements such as an Electrochemical Impedance Spectroscopy (EIS) or charge/discharge cycles at small current rates are added. The latter can be used to perform an Incremental Capacity Analysis (ICA) or Differential Voltage Analysis (DVA).

In the capacity measurement the battery cells are charged and discharged within their maximum voltage range. At the end of charging, after the maximum voltage is reached, typically a Constant Voltage (CV) phase follows until the current reaches a lower limit (mostly 1/20C). This ensures better comparability of the measured capacities since the lithium ions got more time to rearrange in the electrodes. Afterwards, the cells are discharged at Constant Current (CC) to their final discharge voltage to determine the discharge capacity.

The internal resistance is often determined using a pulse test at different states of charge. In this procedure, the cell is charged or discharged to a fixed SOC with a constant current. After a pause, a charge and/or discharge pulse at a high current rate (usually above 1C) follows. When a charge and discharge pulse are performed, a short rest is inserted between them. Under load, the voltage of the battery deviates from the voltage at rest due to voltage drop on the polarization resistance. The polarization resistance is made up of different components that affect the overvoltage on different time scales. The ohmic resistance causes the initial voltage drop. The charge transfer resistance, which is influenced by the double layer capacitance at the border between electrode and electrolyte, produces the flattening voltage drop in the time range of a few seconds. The final voltage drop is provided by the limited diffusion speed of the lithium ions in the electrolyte and the electrode material [14,

15]. Accordingly, the pulse time and current determine which and how intense components of the polarization resistance are considered. The resistance is then determined by Eq. (3.1):

$$R_t = \frac{U_t - U_{t_0}}{I}. \tag{3.1}$$

Thereby $U_t - U_{t_0}$ is the voltage difference caused by the current I, evaluated after the time t.

Table 3.2 shows the main components of the characterization measurements used in the calendar aging studies introduced in Table 4.1, provided they presented detailed information about their measurement process.

Performing a capacity measurement is a fundamental commonality of the characterizations listed in Table 3.2. However, the individual capacity measurements are significantly different. The most important differences are the number and the current rate of the measurement cycles. Most capacity measurements are performed at a current rate of 1C. Hahn et al. [8] determine the capacity at 1C and at C/10. Since the transport processes in the battery only take place at a limited speed, the capacity increases with decreasing discharge current. In addition to a higher capacity, the C/10 measurement showed fewer outliers compared to the 1C measurement. Furthermore, at a lower current a smaller capacity increase was measured at the beginning of aging. Since both aspects are beneficial for model fitting, Hahn et al. [8] decided to use the C/10 capacity measurement to evaluate the capacity decrease in their calendar aging study. Barai et al. [16] summarized the commonly used charge and discharge current rates in recent literature and international standards in capacity measurements in their discussion of non-invasive characterization methods. Most commonly, the capacity measurement is performed with a current rate of 1C or C/3. The latter is often used in an automotive application context and is adapted to the average discharge current of a cell in a battery electric vehicle [16, 17]. Consistent with this, Hoog [9] and Rumberg [12] used a smaller current rate of C/3 in their capacity test.

3.1.2 Aging mechanism in calendar aging and characterization cycling

The main causes of calendar aging are parasitic reactions between electrolyte and electrode. They can be classified into three categories: anode reactions (electrolyte

Source	Capacity Measurement			Pulse Test			Other
	ch.	disch.	cycl.	pulse time ch/disch	pulse C-rate ch/disch	SOC steps	
Baghdadi et al. [5]	CC/CV 1C	CC 1C	2	-/ n.a.	-/1C	1	Pseudo OCV, EIS
Ecker et al. [6]	CC/CV 1C	CC 1C	1	10s/ 18s	3C/ 4C	n.a.	EIS
Grolleau et al. [7]	CC/CV 1C	CC 1C	3	720s/ 720s	1C/ 1C	5	EIS
Hahn et al. [8]	CC/CV 1C and CC/CV 1C	CC 1C and CC $\frac{C}{10}$	3 and 1	-/30s	-/4C	3	Charge CC/CV $\frac{C}{10}$
Hoog et al. [9]	CC $\frac{C}{3}$	CC $\frac{C}{3}$	3	-	-	-	-
Marongiu et al. [10]	CC/CV 1C	CC 1C	1	n.a.	n.a.	n.a.	-
Naumann et al. [11]	CC/CV 1C	CC 1C	2	10s/ 10s	$\frac{C}{3}/\frac{C}{3}$ and $\frac{2}{3}$C/$\frac{2}{3}$C and 1C/1C	1	EIS, low rate ch/disch
Rumberg et al. [12]	CC/CV $\frac{C}{3}$	CC $\frac{C}{3}$	3	-/18s	-/3C	1	OCV
Schmalstieg et al. [2]	CC/CV 1C	CC 1C	1	10s/ 18s	1C/ 2C	9	-

Table 3.2: Main components of the characterization measurements in calendar aging experiments. For the capacity measurement the charge (ch.) and discharge (disch.) current rate and the number of cycles (cycl.) are shown. For the pulse test pulse time and C-rate of the charge and discharge pulse and the number of SOC steps are listed. The abbreviation n.a. means, that the information was not available in the cited source.

reduction leads to Solid Electrolyte Interface (SEI) growth), cathode reactions (including electrolyte oxidation and transition metal dissolution), and coupled reactions (e.g. transition metals dissolved from the cathode affect SEI growth at the anode) [12, 18]. SEI growth is assumed to be the dominant aging mechanism and causes irreversible decrease in capacity due to loss of lithium inventory. Reversible capacity loss and gain can be caused by the Passive Anode Effect (PAE). Usually, the anode in lithium-ion batteries is oversized for example due to positioning tolerances in manufacturing when stacking electrodes. Furthermore, in double-sided coatings, the externally located anode has no cathode counterpart [19, 20]. Thus, the anode is not fully utilized during charging and discharging processes. When potential differences occur between the active and passive part of the anode, lithium ions slowly enter and leave the overhang by diffusion. After lithium ions entered the overhang, they are in the short term not available for cyclization and therefore the cell capacity reversibly decreases. If lithium ions are released from the overhang, the cell capacity increases. The equalization of the lithium-ion concentration in the active and passive part of the anode happens on large time scales in the range of a few days to several months [19, 21].

In addition, reversible capacity gain can also be caused by cathodic side reactions, which lead to a reintercalation of lithium ions back into the cathode [12, 18].

In contrast to that, during cycling additional aging mechanisms occur due to the expansion and contraction of the electrode materials caused by the lithium-ion (de-) intercalation. Thereby, the current rate that the cell is subjected to has an influence on the dominant aging mechanisms. At cycling with small currents, cracking in the solid electrolyte interface predominates [22]. Concentration gradients in the electrodes are kept to a minimum at low current rates, therefore less internal stress is exerted on individual particles, which reduces cracking in the active material. When cycling with higher current rates cracking in the anode and cathode active material becomes more relevant. Furthermore, the probability of lithium plating increases due to accumulating lithium ions at the anode [23, 24]. Interestingly, also the SEI growth rate increases with higher current during cyclization. This can be explained not only by increased fracture and regeneration of the SEI layer, but also by the electrochemistry of diffusion- and migration-limited SEI growth itself [25]. The mentioned aging mechanism typically cause capacity loss and resistance increase. Contrary to this, Dubarry et al. [26] found an improvement in the cell kinetics of high energy cells cycled with current rates higher than C/5. It is likely caused by an increase in the active surface area due to deformation and cracking in the cathode material resulting from volume changes of the electrode particles during lithium-ion insertion and extraction which is referred to by the authors as

an 'electrochemical milling' process. With this, the local effective current density decreases, which leads to a smaller voltage polarization at a fixed current rate. As a final result the discharge voltage, which interrupts the discharging process, is reached later and the capacity of the cell increases.

3.1.3 Open questions in calendar aging studies

Although the characterization measurements in calendar aging studies differ significantly (see Table 3.2), the influence of characterization on the measured change in battery capacity and resistance was assumed to be negligible so far. However, depending on the choice of measurement settings, the additional aging mechanisms in cycling may significantly affect the loss of capacity and increase in the internal cell resistance that occurs in the calendar aging measurement.

Some findings in published calendar aging studies could so far not be explained by calendar aging mechanisms or the PAE. Rumberg et al. [12] attributed a capacity gain of a cell aged at 10% SOC and 45°C to the effect of the anode overhang, since the cells were stored at 30% SOC prior to the start of aging. However, they could not relate an observed capacity gain at 25°C and 100% SOC to the PAE. In this case, capacity should be decreased by absorption of lithium ions through the overhang during calendar aging. Since it was only a single cell behavior, they did not further search for an explanation. Naumann et al. [11] also assumed a superposition of lithium gain from the overhang and lithium loss due to SEI formation as the cause for the observed capacity gain of their calendar aged cells. They further observed a drop in resistance which could not be explained directly with PAE, since no SOC dependence of the effect was found. They assumed the influence of measurement uncertainties as a possible cause. Lewerenz et al. [20] also noted a drop in resistance on LFP cells calendar aged at 25°C. They suggested that this may be due to better lithium and electrolyte distribution after initial cycling of the cell in the checkup after a long storage period.

In the discussed literature, a decrease in resistance or an increase in capacity was found in calendar aged cells that could not be related to the passive anode effect or calendar aging mechanisms. From this, the central research question of this paper follows:

- Is there a significant effect of the characterization measurement on capacity and resistance in calendar aging studies?

To answer this question, this study focused on quantifying the influence of the characterization on capacity loss during calendar aging of commercial NMC cells. For this purpose, a method was developed using periodic characterization measurements. Considering the effect of the characterization, the reversible and irreversible capacity loss which belongs to the calendar aging was determined. The corrected data are finally used to parameterize a semi-empirical calendar aging model.

3.2 Material and methods

This section provides a detailed description of the used cells, measurement systems and methods to allow reproduction of the results.

3.2.1 Cell specification and testing system

The cells studied were commercial Li(NiMnCo)O_2 (NMC)/graphite pouch cells with a nominal capacity of 64 Ah. The voltage limits are 3.0 V minimum and 4.2 V maximum voltage according to the data sheet provided by the manufacturer. The cells were shipped as a module with about 40% SOC and after a few cycles stored at room temperature. For the aging tests they were removed from the module with about 50% SOC. At this time, the cells were three years old and accordingly already pre-aged.
The measurements are performed with a Maccor series 4000 automated test system with 0 A-150 A current and 0 V-8 V voltage range measuring channels. The current error specified by the manufacturer is 0.05% of full scale current (ΔI = 0.075 A), the voltage error is 0.02% of full scale voltage (ΔU = 1.6 mV). During the measurements, the cells were acclimatized at a constant temperature in a Vötsch VC 7018 climatic chamber.

3.2.2 Error analysis

The error of the capacity loss is calculated using the Gaussian error propagation law for uncorrelated quantities [27]

$$\Delta F = \pm\sqrt{\left(\frac{\delta F}{\delta x}\cdot\Delta x\right)^2+\left(\frac{\delta F}{\delta y}\cdot\Delta y\right)^2+....} \tag{3.2}$$

Here $F = F(x, y, ...)$ is a functional relation between different directly measurable quantities x, y and the error of the corresponding quantity $\Delta x, \Delta y$. According to this, the measurement error of the capacity is calculated over

$$\Delta C = \Delta I \cdot t_c \tag{3.3}$$

with the capcity measurement time t_c assumed to be error-free. The error of the capacity equals $\Delta C = \pm 0.075$ Ah for a measuring time of one hour. This corresponds to a relative error of 0.1% with respect to the nominal cell capacity of 64 Ah.

3.2.3 Calendar aging

At the start of the test series a preconditioning was performed. It consisted of five charge and discharge cycles with 1C. This was followed by an initial characterization of the cells. For the investigation of the calendar aging, the cells were charged to a fixed SOC with 1C at 23°C. The SOC is related to the actual cell capacity C_{act}:

$$SOC\ [\%] = \frac{\int I dt}{C_{act}} \cdot 100\%. \tag{3.4}$$

Subsequently, the cells were climatized for 3h to the defined aging temperature. In calendar aging, they rested for 60 days before a re-characterization was performed. The SOC was not actively corrected, therefore a slight SOC shift occurs during aging due to the self-discharge of the cells. Aging was performed at two temperatures (23°C and 40°C) and three states of charge (50%, 70% and 90% SOC). Due to the expected Arrhenius dependence of the capacity loss on temperature (see subsection 3.3.4), to investigate two temperatures was considered to be sufficient to save measurement resources. Two cells were tested at each test condition to identify possible outliers by considering the expected dependence of the cell aging on the investigated stress factors SOC and temperature. Table 3.3 shows the test matrix of the twelve calendar aged cells.

Temperature/ SOC	50%	70%	90%
23°C	2	2	2
40°C	2	2	2

Table 3.3: Calendar aging test matrix with the number of cells for each storage condition

3.2.4 Characterization

The characterization consists of a capacity measurement, a pulse test and a discharge with a small current at 23 °C. In the capacity measurement, the cells were first CC charged with 1C (64 A) to their final charge voltage of 4.2 V. This was followed by a CV phase until the current was less than 1/20C. The cells were then CC discharged with 1C to their final discharge voltage of 3 V to determine the discharge capacity. After each charging and discharging, a 30-minute rest followed to allow cell relaxation. The procedure is repeated twice and the second measurement is used to determine the discharge capacity.

The resistance was determined in a Hybrid Pulse Power Characterization (HPPC) test at three SOC (10%, 50% and 90% SOC). Thereby, the cells were first charged with 1C to the smallest SOC. After a one hour rest, a 10 s discharge pulse was performed with 1C. The change in voltage at the beginning and after the end of the pulse was recorded with a high resolution of 10 ms. The cells rested for 60 s before a 10 s charge pulse of 1C was applied. After another 60 s pause, the cells were charged to the next SOC. When the 90% SOC measurement was completed, the cells were fully charged with 1C CC/CV. Finally, after another 30 minute rest, a CC discharge with C/10 completes the characterization measurement.

To investigate the influence of the characterization on the calendar aging study, a periodic characterization was performed with two additional cells. It consists of continuous characterizations with a 3h rest in between. A complete characterization procedure is shown in Fig. 3.1.

3.3 Results and discussion

3.3.1 Aging results

The capacity loss of the batteries during the calendar aging measurement $C_{loss,meas}$ was calculated using

$$C_{loss,meas} = 1 - \frac{C(t)}{C(t_0)} \tag{3.5}$$

with the cell capacity $C(t)$ at measurement time t and the initial cell capacity $C(t_0)$. Fig. 3.2 shows the capacity loss of the cells during calendar aging at different states

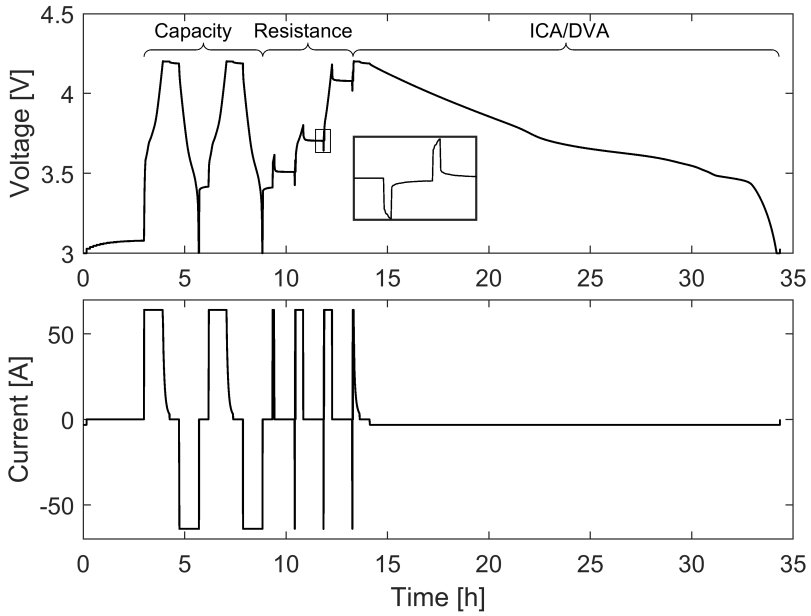

Figure 3.1: Voltage and current profile of the characterization over the measurement time.

of charge and temperatures. The error intervals are calculated using the Gaussian error propagation law according to Eq. (3.5) and (3.2). They do not fully explain the deviation between the measured values of the two individual cells at the same aging conditions. That might be caused by not considered systematic errors or by random errors like the cell-to-cell variation of the single cells. Due to a delay in the third characterization step, the second measurement interval at 23°C had to be extended from two to three months.

As expected, the capacity loss is higher at elevated temperature. Furthermore, there are differences between the the capacity losses at various storage SOC. It is noticeable, that a higher SOC does not necessarily correlate with a higher capacity loss at time t. Although the loss of capacity is lowest at 50% SOC, it is almost the same in the long term at 70% and 90% SOC. At 23°C, the capacity loss of one cell at 70% SOC is nearly twice as high compared to the 90% SOC cells after 422 days. However, this seems to be a single cell behaviour since the second cell aged at 70% SOC has a similar capacity loss as the cells aged at 90% SOC.

After the first initial increase, the capacity loss flattens out at 40°C and reaches a value of around 1% after 200 days. Subsequently, the curve turns into an exponential growth. In contrast, the capacity loss at 23°C increases more linearly towards the end of the test series. At the beginning of the aging a negative capacity loss, which means a gain in capacity, was recorded. For one of the cells aged at 50% SOC, the phase of capacity gain is not finished even after more than one year of aging.

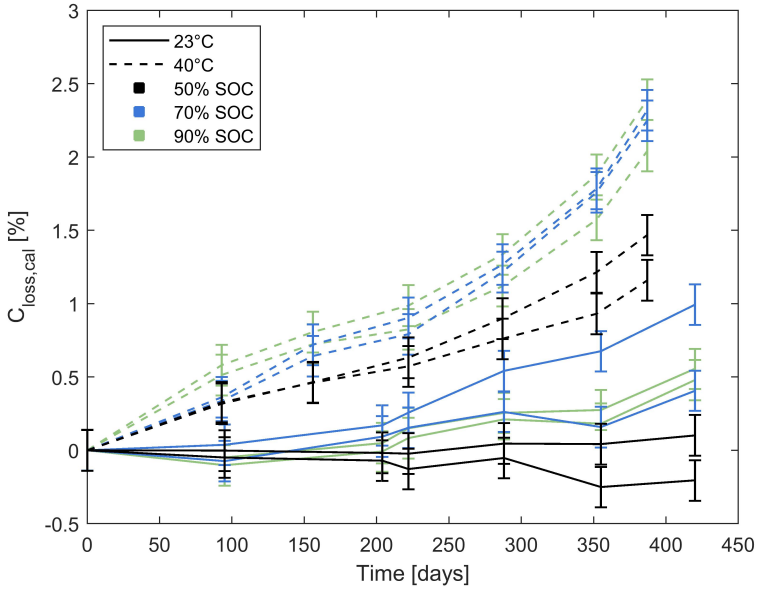

Figure 3.2: Relative capacity loss as a function of time for calendar aging at various states of charge and temperatures.

An initial gain in capacity was already observed in various calendar aging studies and is often explained by the passive anode effect [8, 9, 11]. To estimate the maximum PAE, the volumetric excess of the anode was determined in an initial cell opening. Each anode has a 5.2% larger volume than the corresponding cathode. Therefore, assuming equal volumetric capacity of the electrodes, a maximum of 5.2% of the cell capacity could be stored in the overhang. To estimate how much of this capacity can be absorbed or released in the first calendar aging phases, it is assumed that the passive and active parts of the anode are in equilibrium at the beginning of the aging tests and that their SOC corresponds to the initial cell state of charge of 50% SOC. Accordingly, the overhang absorbs lithium ions at subsequent calendar aging at a higher SOC. The SOC of the overhang slowly equalizes to the SOC of the active anode during calendar aging. Therefore, for the calendar aging at 90% SOC, it is assumed, that the overhang SOC changes by a maximum of 40% SOC, which corresponds to a fraction of 2.1% of the total cell capacity. Storage at lower SOC has a correspondingly lower maximum capacity loss due to the overhang effect: 1% of the total cell capacity at 70% storage SOC in calendar aging and 0% capacity loss at 50% storage SOC. Thus, when stored at 50% SOC, a negligible loss or gain in capacity due to the PAE is expected. Since the battery cells were characterized only every two months, the main capacity loss due to PAE should occur in the in the first one to two calendar ageing phases. This does not agree with the measured capacity gain at 50% SOC which for one cell increases even further towards the end of the

aging. Additionally, even the cells aged at higher SOC and 23°C do not show an increased capacity loss in the first months of aging. This is not in agreement with the estimated maximum effect of the PAE. For this reason, the PAE does not provide an explanation for the observed aging behavior, in particular the capacity gain of the cells aged at 23°C. There must be another superimposed effect.

3.3.2 Quantification of the characterization measurement effect

A periodic characterization measurement is used to quantify the capacity loss due to characterization $C_{loss,char}$. It is then separated from the capacity loss due to calendar aging, which can be divided into an irreversible part $C_{loss,cal,ir}$ (mainly SEI formation), and a reversible part $C_{loss,cal,rev}$ (e.g. capacity loss or gain through PAE). Consequently, the measured capacity loss in calendar aging adds up as follows

$$C_{loss,meas} = C_{loss,cal,ir} + C_{loss,cal,rev} + C_{loss,char}. \tag{3.6}$$

A capacity gain is a negative capacity loss and thus compensates capacity loss in the calendar aging measurement. Fig. 3.3a shows the capacity loss and Fig. 3.3b the discharge polarization resistance at 10% SOC over the number of characterizations of the two studied cells in the periodic characterization measurement. The resistance evaluation is done according to Eq. (3.1) ten seconds after the pulse. The SOC of 10% was chosen because the resistance is highest here and changes in resistance are best identifiable.

The capacity loss is negative at all characterizations which means that the capacity increases compared to the initial capacity. The capacity gain is a maximum of 0.8% of the initial capacity after seven characterizations. Subsequently, the capacity decreases linearly by approx. 0.3% up to the 15th characterization. Since all the results of the calendar aging at 23°C up to 300 days after the start of the tests are less than 0.5% capacity loss (Fig. 3.2), the influence of the characterization on the capacity is not negligible small. Furthermore, in Fig. 3.3b, the resistance decreases with the number of characterizations. The effect of characterization equally affects all cells in the calendar aging measurement and therefore explains a drop in resistance independent of the aging SOC and temperature. Consequently, the influence of the characterization measurement can explain the resistance decrease observed by Naumann et al. [11] and Lewerenz et al. [20].

A capacity gain in combination with the drop in resistance during cyclic aging was already observed by Dubarry et al. [26] at LFP high energy cells. The capacity gain

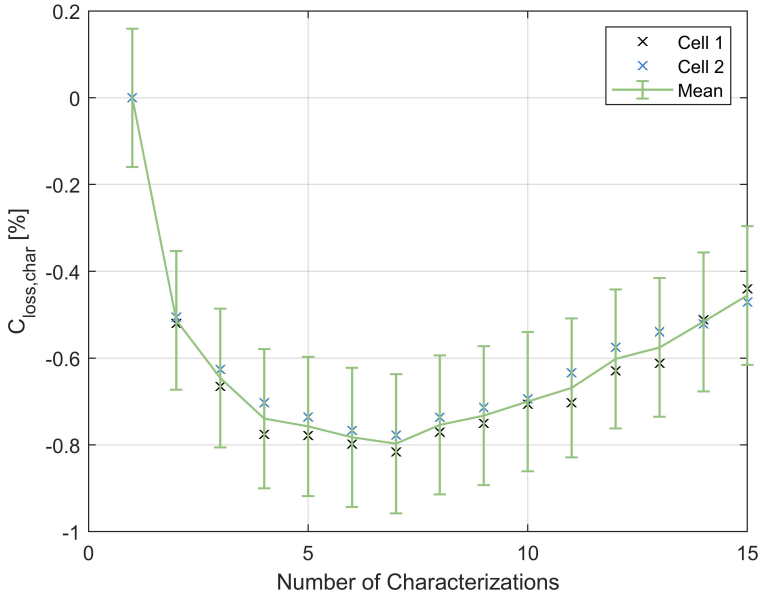

(a)

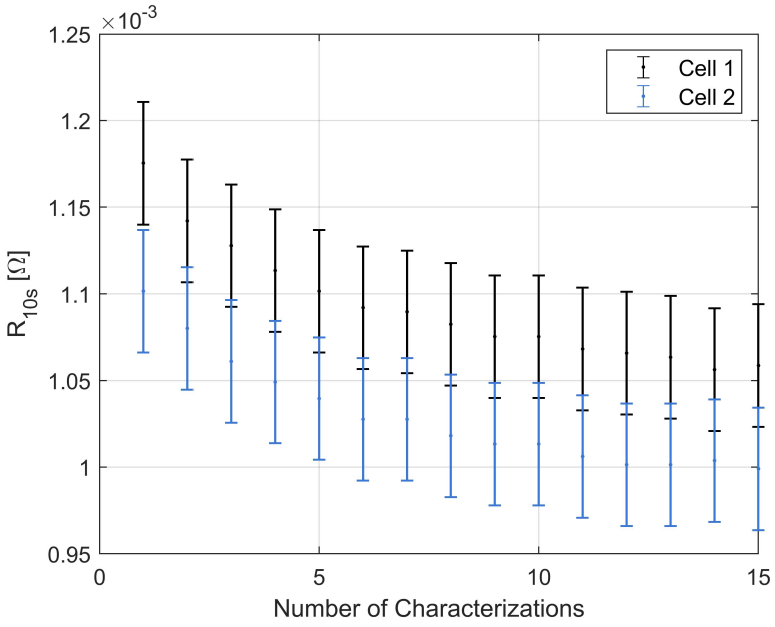

(b)

Figure 3.3: Capacity loss (a) and resistance at 10% SOC (b) over the number of characterizations in the periodic characterization measurement.

is explained by a reduced overvoltage at cyclization, which causes the discharge to terminate later, increasing the capacity of the cell. This could be the result of a reduced polarization resistance. Possible causes for a reduced polarization resistance include an improvement in the electronic conduction in the electrode material, a reduction in the charge transfer resistance at the interface between the electrode and the electrolyte, and an improvement in the diffusion of lithium ions through the active material and the electrolyte. Furthermore, an increase of the electrode surface and thus a decrease of the effective local current density at the same C-rate is a possible mechanism to reduce the overpotential at the corresponding electrode. The increase of the cathode surface was determined by Dubarry et al. [26] to be the most relevant mechanism which ultimately leads to an increase in capacity of the LFP cells considered. The influence of a kinetic effect in the periodic characterization measurement can be investigated analyzing the End Of Discharge Open Circuit Voltage (EOD OCV). Fig. 3.4a shows the EOD OCV 30 minutes after the battery is discharged with 1C and C/10 over the number of characterization cycles. The EOD OCV after discharge with 1C is significantly higher than after discharge with C/10. A higher open circuit voltage generally means a higher state of charge of the battery. Thus, the cell was discharged less at 1C discharge due to the higher voltage drop on the polarization resistance.

The relative EOD OCV for a discharge with 1C and C/10 is shown in Fig. 3.4b. At both current rates the EOD OCV reduces with the number of characterizations. The decrease at C/10 is about 0.5% after 15 characterizations while at 1C it is three times larger. A decreasing EOD OCV indicates a deeper discharge of the cell, which in turn is connected to an increase in capacity. Since the voltage losses on the polarization resistance rise with higher current rates, the decreasing resistance has a stronger influence on the capacity measurement carried out with a higher current and the capacity gain is more prominent here. This also supports the results of Hahn et al. [8] who found a smaller increase in capacity in the C/10 comparing to the 1C capacity measurement results. To reduce the influence of kinetic effect on the capacity measurement and to limit the aging due to the characterization itself, a capacity measurement with a smaller current is preferable to a 1C capacity measurement. The current rate of C/3 offers a good compromise between reducing measurement time and minimizing the effect of the characterization measurement. It is, next to 1C, the most recommended current rate to be used in the capacity measurement by test standards and research community [16].

The influence of the characterization measurement is not equally strong in all battery cell chemistries. High-power cells, for example, are less affected by kinetic effects since they are optimized for high power capability [26].

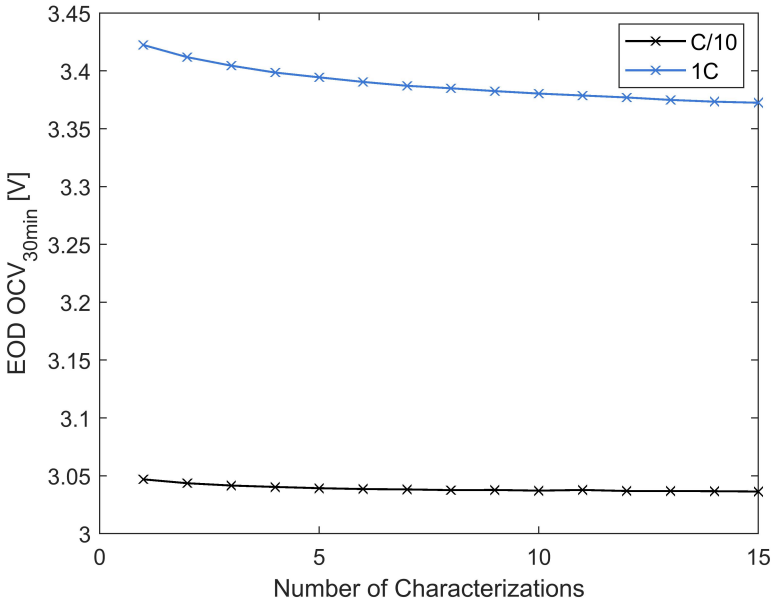

(a)

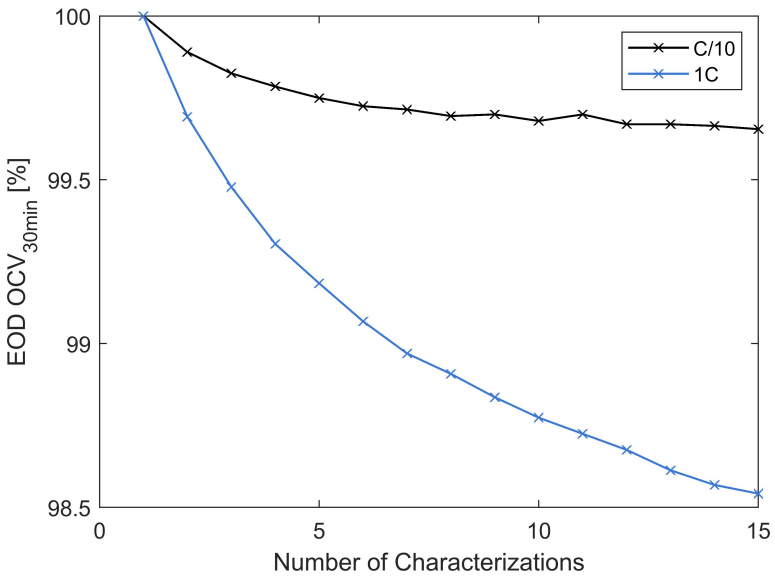

(b)

Figure 3.4: End Of Discharge Open Circuit Voltage (EOD OCV) (a) and relative EOD OCV (b) 30 minutes after discharge with 1C and C/10 plotted over the number of characterizations in the periodic characterization measurement.

3.3.3 Data correction by the characterization capacity loss

To correct the effect of characterization on the capacity in calendar aging, the mean value of the measured capacity loss during characterization is subtracted from the capacity loss measured in the calendar aging study. According to Eq. (3.6) the result is the superposition of the reversible and irreversible capacity loss in calendar aging. The corrected capacity loss $C_{loss,corr}$ is shown in Fig. 3.5. The error of $C_{loss,corr}$ is determined over Pythagorean addition of the errors of $C_{loss,meas}$ and $C_{loss,char}$.

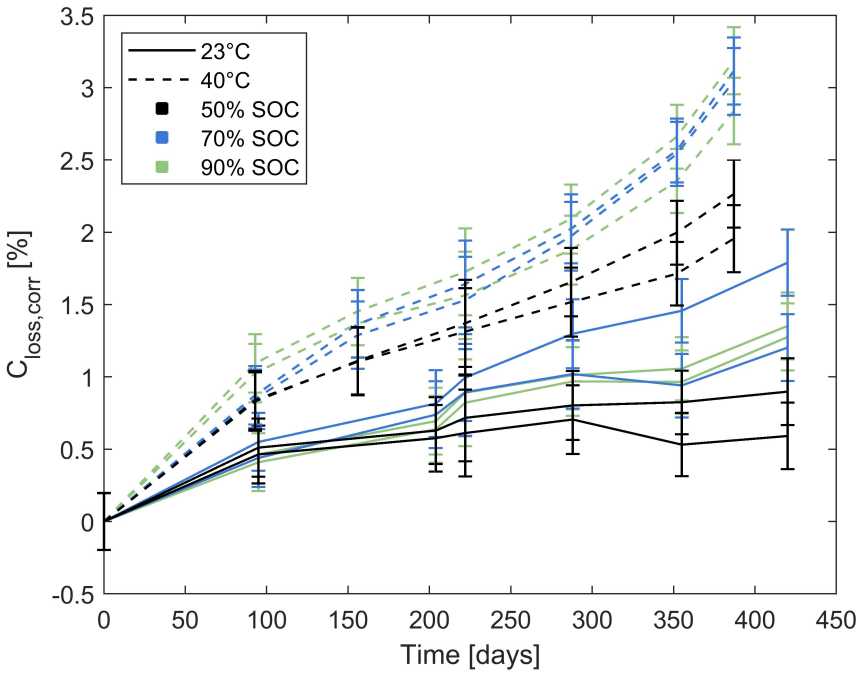

Figure 3.5: Capacity loss in calendar aging corrected by the capacity loss due to characterization as a function of time.

The correction provides a significant change in the calendar aging capacity loss. In contrast to the original capacity loss of the calendar aging measurement in Fig. 3.2, the typical flattening capacity loss with the time occurs at 23°C instead of the (initial) capacity gain. Since the correction is independent of SOC and temperature in calendar aging, the previously recognized basic relationships (1. higher temperature causes more capacity loss, 2. lower capacity loss at 50% SOC than at 70% and 90% SOC) remain. The increase in capacity loss with longer test times is weakened and can now be seen from approximately 290 days on. As the effect is more noticeable at high temperatures and high SOC, it could be attributed to dissolution of transition metals at the cathode which deposit at the anode and accelerate SEI growth. Since we focus on the effect of the characterization, the

reversible and irreversible capacity loss are not further separated and analyzed in this paper. Nevertheless, the contribution of the overhang to the initial increase in capacity loss could be estimated from the data using the method presented by Lewerenz et al. [21]. According to their theory the initial capacity loss is caused by the influence of the anode overhang and the following linear capacity loss belongs to the irreversible battery aging.

3.3.4 Model parameterization

The corrected data are now used to parameterize a semi-empirical aging model. For simplification, the functions depending on time, temperature and SOC are assumed to be independent of each other. The separated functions are first parameterized individually and then combined into an overall model.

Time dependency

For models with few fit parameters, the simple power law t^{β} time dependency approach provides a good compromise between high quality of the fit and low overfitting potential [8]. Describing the capacity loss due to SEI growth, this approach assumes that there is no SEI at time t = 0. Furthermore, the predicted capacity loss at infinite test time is infinite. To determine the exponent β of the time dependency, all measured data are fitted with the equation

$$C_{loss,corr}(SOC, T, t) = A(SOC, T) \cdot t^{\beta},\ 0 < \beta < 1. \tag{3.7}$$

The factor A(SOC,T) is determined individually for each measured temperature and SOC combination, using the mean of the capacity loss of the two aged cells. The parameter β is set to be the same for all measured data. The fitting is based on the least squares method and performed using Matlab. To find a minimum sum of the squares of the residuals, the initial value of A(SOC,T) is varied in ten steps between 0.1 and 1. The results of the fit are shown in Fig. 3.6. The factor A(T,SOC) is the same here for 70% and 90% SOC at 40°C, so only one dashed line is visible. Furthermore, in the first subplot the Root Mean Squared Error (RMSE) for the deviation of the measurements mean value from the model is shown. Below this, the exponent β that results from fitting the data up to time t is plotted. It was determined from a minimum of three measured values.

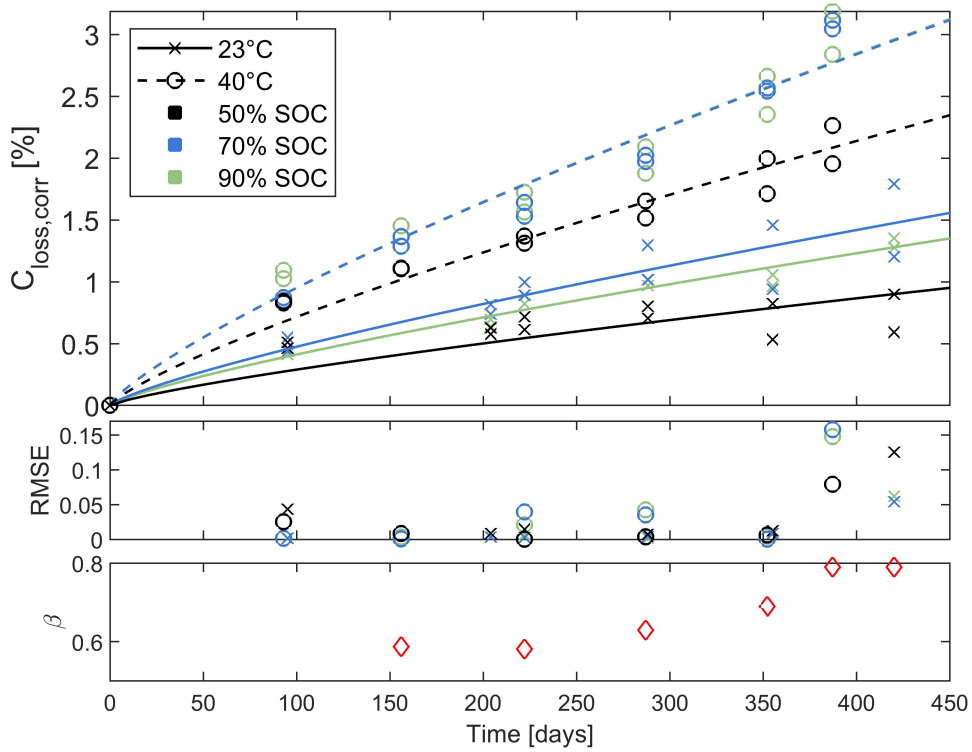

Figure 3.6: Top: Fit (line) of the measured capacity loss at different SOC and temperatures (marker) over the time with the final exponent $\beta = 0.789$. Middle: Root Mean Squared Error (RMSE) of the model up to time t. Bottom: Model exponent β when fitting data up to time t.

For the cells considered, the final model exponent is $\beta = 0.789$. It provides a compromise between the initial root-shaped calendar aging and the long-term increasing capacity loss. Fitting only data up to 220 days, β is 0.581 which is close to the square root of time dependency typical for the diffusion limited SEI growth during storage [28]. The continuously increasing exponent due to the subsequent stronger increase in capacity loss demonstrates a change in aging behavior of the cells. The final exponent provides an underestimation of the capacity loss in the first months of aging. Nevertheless, the RMSE of the model is below 0.05 for all measurements up to 350 days, which is considered to be sufficient. Afterwards, the RMSE increases significantly. The changed aging behavior, especially at high temperature and high SOC, might be due to the influence of coupled reactions between the cathode and the anode since transition metal dissolution is accelerated by high temperatures and high SOC [18]. The measurements had to be stopped after 420 days, therefore it was not possible to investigate whether this effect only occurs in the short term or continues in the long term.

Temperature dependency

The temperature dependency is modeled by the Arrhenius equation. It characterizes the change in reaction kinetics with temperature and has already been used in many aging models [6–8]. The temperature-dependent capacity loss is described by

$$C_{loss,corr}(T,t) = \alpha \cdot \exp\left(\frac{-E_a}{R \cdot T}\right) \cdot t^{0.789} \tag{3.8}$$

with the ideal gas constant R and the activation energy E_a. The model parameters are α and E_a. To parameterize the the temperature dependency, a reference SOC must be selected. The lowest RMSE of the model compared measured data at a fixed SOC and different temperatures is observed at 50% SOC. For this reason, 50% SOC is chosen as the reference SOC. Furthermore, by fitting the entire data, the lowest mean RMSE of the resulting model is achieved. If the SOC and temperature dependency would have to be evaluated at specific points in time, the best model results are obtained by using the latest possible date. However, hereby a change in aging behavior during long-term measurements should be considered. The model parameters E_a and α resulting from the fit are listed in Table 3.4.

SOC dependency

The capcity loss dependency on the SOC is evaluated at 40°C. The cells capacity losses are more clearly distinguishable at elevated temperature. The SEI growth at the anode is strongly dependent on the anode potential [18]. Thus it is also dependent on the SOC of the cell, provided that there is no shift of the electrode potentials relative to each other. Next to SEI growth, the capacity loss during calendar aging can be influenced by cathode and coupled side reactions. Their quantity and SOC dependence varies with the cathode material and electrolyte composition [23]. Consequently, it is difficult to assume a fixed SOC dependency since various behaviors are possible at different cell chemistries for the same aging conditions. Therefore, an analysis of the SOC dependency is performed. For this purpose, Fig. 3.7 shows the corrected capacity loss versus SOC at constant temperature of 40°C and fixed points in time.

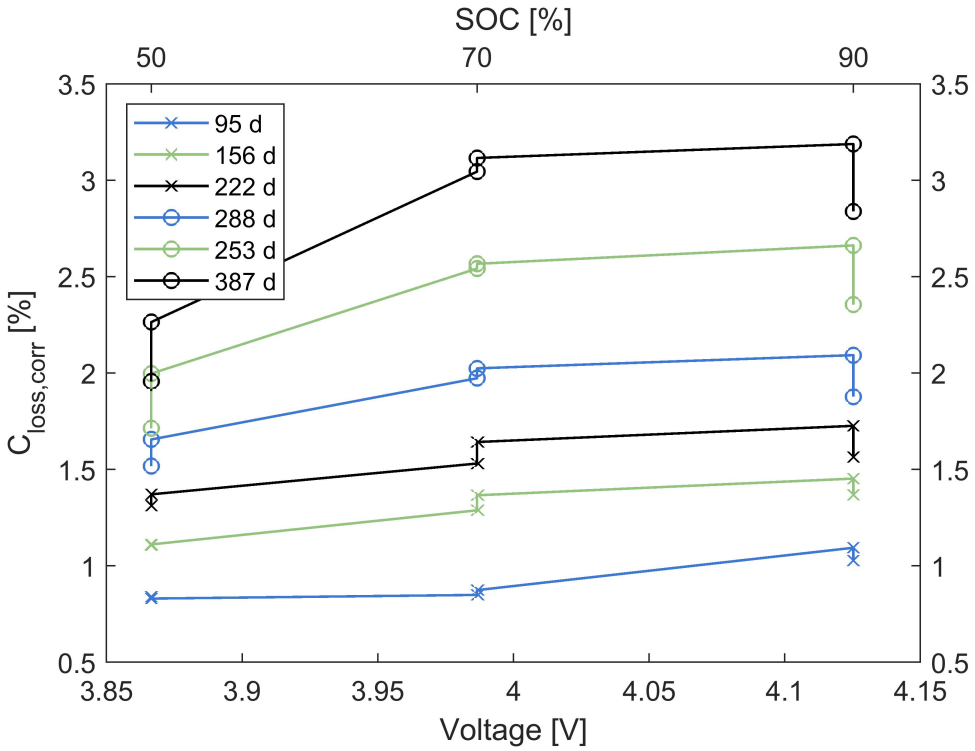

Figure 3.7: Corrected capacity loss at 40°C as a function of SOC at different times of the ageing process.

First, the capacity loss increases linearly with higher SOC. The aging behavior changes after around 288 days. The capacity loss increases more strongly towards 70% SOC and then stagnates to 90% SOC. Due to increasing side reactions at the cathode at higher SOC, lithium ions intercalate back into the cathode. This may

compensate capacity loss above 70% SOC and could be a cause for the apparently decreasing capacity loss at 90% SOC [12]. The increase in capacity loss between 50% and 70% SOC (which can also be seen in the exponential increase of the capacity loss at higher SOC in Fig. 3.5) could be due to transition metals coming from the cathode, accelerating SEI growth at the anode. These assumptions would need to be verified in a post-mortem analysis. Below 288 days, a linear SOC dependency can be assumed:

$$C_{loss,corr}(SOC,t) = (\gamma \cdot SOC + \delta) \cdot t^{0.789}. \tag{3.9}$$

The parameter γ and δ resulting from the fit of the total measured data at 40°C are shown in Table 3.4.

E_a [kJ/mol]	α	β	γ	δ
36.36	$2.15 \cdot 10^{4}$	0.789	$1.19 \cdot 10^{-4}$	0.01

Table 3.4: Model parameters determined by fitting the corrected calendar aging data.

Total calendar aging model

The seperated functions for the capacity loss dependent on SOC and temperature are finally combined into an overall model. For this purpose, a scaling of the functions (3.8) and (3.9) is performed according to Schmalstieg et al. [2]:

$$C_{loss,corr}(T,SOC,t) = \frac{C_{loss,corr}(SOC,t) \cdot C_{loss,corr}(T,t) \cdot C_{loss,corr,\varnothing}}{C_{loss,corr}(50\%\,SOC,t) \cdot C_{loss,corr}(40°C,t)} \tag{3.10}$$

with the mean value of the SOC- and temperature-dependent functions at the reference SOC (50% SOC) and reference temperature (40°C)

$$C_{loss,corr,\varnothing} = \frac{C_{loss,corr}(50\%\,SOC,t) + C_{loss,corr}(40°C,t)}{2}. \tag{3.11}$$

The model results are shown in Fig. 3.8.

At the beginning and at the end of the measurement, the final model shows larger deviations from the capacity loss of the considered NMC cells. This is due to the changing aging behavior from approximately 288 days on. The selected time dependency according to the power law approach forms a compromise between

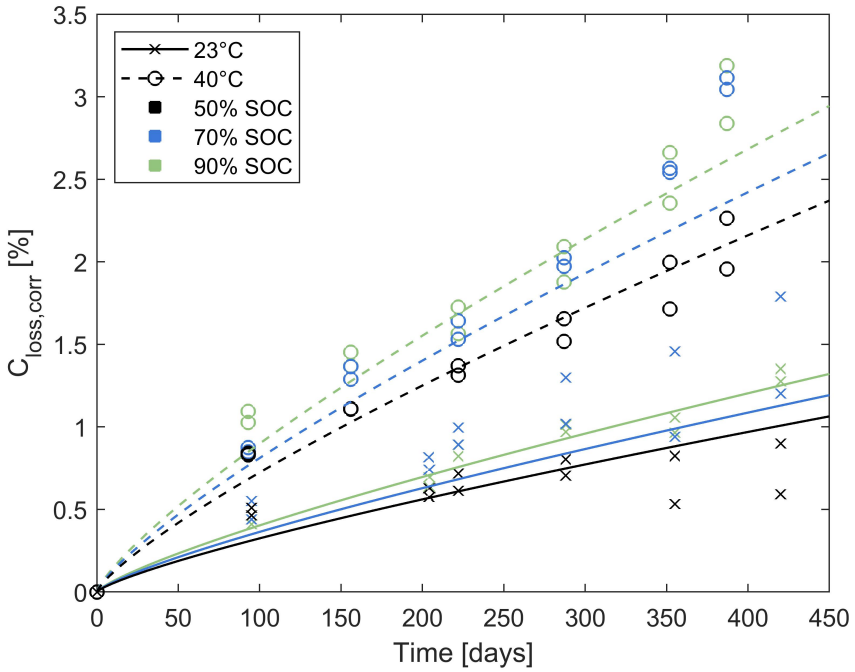

Figure 3.8: Calendar aging model results for the SOC- and temperature-dependend capacity loss over the time (line) and corrected capacity loss data (marker).

early and long-term aging. The SOC dependency was parameterized on the basis of a linear relationship, which changes to a flattening SOC relationship in the course of the aging process. In future calendar aging models the changing aging behavior should be considered separately to increase model accuracy. Rumberg et al. [12] included the effect of cathodic side reactions in their calendar aging model. To the authors' knowledge, the influence of transition metal dissolution has not yet been considered in semi-empirical calendar aging models. This is part of future research.

3.4 Conclusion

In this calendar aging study on commercial NMC cells, additional periodic characterization measurements were used to quantify and correct the effect of the checkup on the loss of capacity due to calendar aging. A gain in capacity due to the characterization measurement has been detected. It was attributed to an improvement in cell kinetics which was indicated by a decrease in cell resistance. Due to the decreasing resistance, the end-of-discharge voltage is reached later, the cell is discharged further and the capacity increases. A stronger discharge of the cell was proven by the

evaluation of the end of discharge open circuit voltage. Based on literature research, the cause of the decreasing resistance was assigned to an increase of the cathode surface due to cracking and structural disordering. The capacity gain caused by the kinetic effect and the electrode degradation itself increase with increasing current rate in the capacity measurement cycles. To ensure that the capacity fade results of future aging studies are comparable, the findings lead to the recommendation to perform the capacity measurement in cell characterizations with a lower current rate than 1C. The current rate of C/3, already often used in literature, provides a good compromise between saving measurement time and gentle cycling. The corrected measurement data showed the typical root-shaped capacity loss expected from SEI growth in the first nine months of ageing. Subsequently, a change in the aging behavior has been found. It was characterized by an exponential increase in capacity loss over time, especially at elevated temperature and SOC. Furthermore, a constant capacity loss was observed between 70% SOC and 90% SOC instead of a previous linear SOC dependency. This may be attributed to the influence of cathodic and coupled side reactions. The exact cause of the changed ageing behavior would have to be further analyzed, for example by a post-mortem analysis. Finally, the corrected calendar aging data were successfully used to parameterize a semi-empirical calendar aging model for the capacity loss. The presented aging model is well suited for an estimation of calendar aging. Nevertheless, for a more detailed capacity loss model, the change in the aging behavior of the batteries with long-term aging should be addressed in future investigations.

Author Contributions

Amelie Krupp: Main author of manuscript. Conceptualization, Methodology, Software, Validation, Formal analysis, Investigation, Data Curation, Visualization, Writing - Original Draft, Writing - Review and Editing, *Robert Beckmann*: Conceptualization, Methodology, Software, Formal analysis, Supervision, Writing - Original Draft, Writing - Review and Editing, *Theys Diekmann*: Investigation, Resources, Writing - Review and Editing, Funding acquisition, *Ernst Ferg*: Conceptualization, Methodology, Supervision, Writing - Review and Editing, *Frank Schuldt*: Conceptualization, Resources, Supervision, Writing - Review and Editing, Funding acquisition, *Carsten Agert*: Conceptualization, Resources, Supervision, Writing - Review and Editing

Acknowledgments

The results were generated in the framework of the project HyReK 2.0 (grant no. 03ET6147C). We thank the German Federal Ministry for Economic Affairs and Climate Action (BMWK) for funding.

References

[1] Amelie Krupp et al. “Incremental Capacity Analysis as a State of Health Estimation Method for Lithium-Ion Battery Modules with Series-Connected Cells”. In: *Batteries* 7.1 (2021), p. 2. DOI: 10.3390/batteries7010002.

[2] Johannes Schmalstieg et al. “A holistic aging model for Li(NiMnCo)O2 based 18650 lithium-ion batteries”. In: *Journal of Power Sources* 257 (2014), pp. 325–334. ISSN: 03787753. DOI: 10.1016/j.jpowsour.2014.02.012.

[3] Xing Jin et al. “Applicability of available Li-ion battery degradation models for system and control algorithm design”. In: *Control Engineering Practice* 71 (2018), pp. 1–9. ISSN: 09670661. DOI: 10.1016/j.conengprac.2017.10.002.

[4] Bolun Xu et al. “Modeling of Lithium-Ion Battery Degradation for Cell Life Assessment”. In: *IEEE Transactions on Smart Grid* 9.2 (2018), pp. 1131–1140. ISSN: 1949-3053. DOI: 10.1109/TSG.2016.2578950.

[5] Issam Baghdadi et al. “Lithium battery aging model based on Dakin’s degradation approach”. In: *Journal of Power Sources* 325 (2016), pp. 273–285. ISSN: 03787753. DOI: 10.1016/j.jpowsour.2016.06.036.

[6] Madeleine Ecker et al. “Development of a lifetime prediction model for lithium-ion batteries based on extended accelerated aging test data”. In: *Journal of Power Sources* 215 (2012), pp. 248–257. ISSN: 03787753. DOI: 10.1016/j.jpowsour.2012.05.012.

[7] Sébastien Grolleau et al. “Calendar aging of commercial graphite/LiFePO4 cell – Predicting capacity fade under time dependent storage conditions”. In: *Journal of The Electrochemical Society* 255 (2014), pp. 450–458. ISSN: 0378-7753. DOI: 10.1016/j.jpowsour.2013.11.098.

[8] Severin Lukas Hahn et al. “Quantitative validation of calendar aging models for lithium-ion batteries”. In: *Journal of Power Sources* 400 (2018), pp. 402–414. ISSN: 03787753. DOI: 10.1016/j.jpowsour.2018.08.019.

[9] Joris de Hoog et al. “Combined cycling and calendar capacity fade modeling of a Nickel-Manganese-Cobalt Oxide Cell with real-life profile validation”. In: *Applied Energy* 200 (2017), pp. 47–61. ISSN: 03062619. DOI: 10.1016/j.apenergy.2017.05.018.

[10] Andrea Marongiu, Marco Roscher, and Dirk Uwe Sauer. “Influence of the vehicle-to-grid strategy on the aging behavior of lithium battery electric vehicles”. In: *Applied Energy* 137 (2015), pp. 899–912. ISSN: 03062619. DOI: 10.1016/j.apenergy.2014.06.063.

[11] Maik Naumann et al. “Analysis and modeling of calendar aging of a commercial LiFePO4/graphite cell”. In: *Journal of Energy Storage* 17 (2018), pp. 153–169. ISSN: 2352152X. DOI: 10.1016/j.est.2018.01.019.

[12] Björn Rumberg et al. “Holistic calendar aging model parametrization concept for lifetime prediction of graphite/NMC lithium-ion cells”. In: *Journal of Energy Storage* 30 (2020), p. 101510. ISSN: 2352152X. DOI: 10.1016/j.est.2020.101510.

[13] Kandler Smith et al. “Comparison of Plug-In Hybrid Electric Vehicle Battery Life Across Geographies and Drive Cycles”. In: *SAE Technical Paper Series*. SAE Technical Paper Series. SAE International400 Commonwealth Drive, Warrendale, PA, United States, 2012. DOI: 10.4271/2012-01-0666.

[14] Tyler DuBeshter and Jacob Jorne. “Pulse Polarization for Li-Ion Battery under Constant State of Charge: Part I. Pulse Discharge Experiments”. In: *Journal of The Electrochemical Society* 164.11 (2017), E3539–E3546. ISSN: 0378-7753. DOI: 10.1149/2.0551711jes.

[15] Anup Barai et al. “A study of the influence of measurement timescale on internal resistance characterisation methodologies for lithium-ion cells”. In: *Scientific reports* 8.1 (2018), p. 21. DOI: 10.1038/s41598-017-18424-5.

[16] Anup Barai et al. “A comparison of methodologies for the non-invasive characterisation of commercial Li-ion cells”. In: *Progress in Energy and Combustion Science* 72 (2019), pp. 1–31. ISSN: 03601285. DOI: 10.1016/j.pecs.2019.01.001.

[17] Grietus Mulder et al. “Comparison of commercial battery cells in relation to material properties”. In: *Electrochimica Acta* 87 (2013), pp. 473–488. ISSN: 00134686. DOI: 10.1016/j.electacta.2012.09.042.

[18] Peter Keil and Andreas Jossen. “Calendar Aging of NCA Lithium-Ion Batteries Investigated by Differential Voltage Analysis and Coulomb Tracking”. In: *Journal of The Electrochemical Society* 164.1 (2017), A6066–A6074. ISSN: 0378-7753. DOI: 10.1149/2.0091701jes.

[19] Balazs Gyenes et al. “Understanding Anomalous Behavior in Coulombic Efficiency Measurements on Li-Ion Batteries”. In: *Journal of The Electrochemical Society* 162.3 (2015), A278–A283. ISSN: 0378-7753. DOI: 10.1149/2.0191503jes.

[20] Meinert Lewerenz et al. “Systematic aging of commercial LiFePO 4 |Graphite cylindrical cells including a theory explaining rise of capacity during aging”. In: *Journal of Power Sources* 345 (2017), pp. 254–263. ISSN: 03787753. DOI: 10.1016/j.jpowsour.2017.01.133.

[21] Meinert Lewerenz et al. “Irreversible calendar aging and quantification of the reversible capacity loss caused by anode overhang”. In: *Journal of Energy Storage* 18 (2018), pp. 149–159. ISSN: 2352152X. DOI: 10.1016/j.est.2018.04.029.

[22] Rutooj D. Deshpande and Dawn M. Bernardi. “Modeling Solid-Electrolyte Interphase (SEI) Fracture: Coupled Mechanical/Chemical Degradation of the Lithium Ion Battery”. In: *Journal of The Electrochemical Society* 164.2 (2017), A461–A474. ISSN: 0378-7753. DOI: 10.1149/2.0841702jes.

[23] Joshua P. Pender et al. “Electrode Degradation in Lithium-Ion Batteries”. In: *ACS nano* 14.2 (2020), pp. 1243–1295. DOI: 10.1021/acsnano.9b04365.

[24] M. M. Kabir and Dervis Emre Demirocak. “Degradation mechanisms in Li-ion batteries: a state-of-the-art review”. In: *International Journal of Energy Research* 41.14 (2017), pp. 1963–1986. ISSN: 0363907X. DOI: 10.1002/er.3762.

[25] Lars von Kolzenberg, Arnulf Latz, and Birger Horstmann. “Solid-Electrolyte Interphase During Battery Cycling: Theory of Growth Regimes”. In: *cssc* (2020). DOI: 10.1002/cssc.202000867.

[26] Matthieu Dubarry, Cyril Truchot, and Bor Yann Liaw. “Cell degradation in commercial LiFePO4 cells with high-power and high-energy designs”. In: *Journal of Power Sources* 258 (2014), pp. 408–419. ISSN: 03787753. DOI: 10.1016/j.jpowsour.2014.02.052.

[27] *Fundamentals of metrology: Part 4: Evaluation of measurements; uncertainty of measurement*.

[28] Fabian Single, Arnulf Latz, and Birger Horstmann. “Identifying the Mechanism of Continued Growth of the Solid-Electrolyte Interphase”. In: *ChemSusChem* 11.12 (2018), pp. 1950–1955. DOI: 10.1002/cssc.201800077.

4 Cyclic aging model

This chapter is based on the publication „Semi-empirical Cyclic Aging Model for Stationary Storages Based on Graphite Anode Aging Mechanisms“ by Amelie Krupp, Robert Beckmann, Theys Diekmann, Gerd Liebig, Ernst Ferg, Frank Schuldt, and Carsten Agert [1]. Compared to the original publication, the introduction of the calendar aging model was shortened because it was already introduced in the thesis chapter 3. The use of the article in the thesis for non comercial purposes is permitted by the publisher Elsevier.

Abstract

Battery life prediction is steadily becoming more relevant due to the increased use of batteries in stationary and mobile applications. Current semi-empirical aging models are often supplemented by empirical model equations and parameterized on the entire available measurement data set. This practice limits their extrapolation capability and transferability. The model in this work describes the two important anode aging mechanisms, solid electrolyte interface (SEI) cracking and reforming and cracking of the active material, by completely physically based equations. A simple incremental capacity analysis (ICA) method is introduced to allow targeted parameterization of the model equations with measurement data, in which the aging modes associated with the respective aging mechanism are present. The overall model can accurately describe the battery capacity loss under dynamic frequency containment reserve loading. It is transferable to all graphite-based battery cell chemistries and provides a basis for future semi-empirical aging models, describing the capacity loss in a wide variety of applications by considering further aging mechanisms.

4.1 Introduction

In the face of a growing need for grid flexibility options and low-emission solutions, battery storages are increasingly used in a wide range of stationary and mobile applications. During its lifetime, the characteristics of a battery change because of aging mechanisms that occur at rest (calendar aging) and under load (cyclic aging). Aging progresses until the energy and power performance requirements of an application are no longer fulfilled and the battery must be replaced. Maximizing the service life of the battery system is crucial not only for its ecological but also for its economic profitability. Therefore, it is of significant interest for system manufacturers and operators to predict and minimize the aging of their battery in application which is reflected in capacity loss and resistance increase. The approach chosen for an aging model determines its accuracy and the effort involved in parameterization and computation. The relevance of the individual features depends on the modeling objective and the final application of the battery. Semi-empirical models are based on physical correlations but parametrized with battery aging data. They offer the advantage of lower computational requirements and simpler parameterization compared to detailed electrochemical models. Furthermore, due to the physical background, they are easier to extrapolate and involve less measurement effort than empirical models [2, 3]. Many approaches for cyclic semi-empirical aging models have been published in the literature. Gewald et al. [4] compiled a tabular overview of semi-empirical aging models including considered stress factors and the target values. In Table 4.1, this review is extended with additional literature sources and restricted to cyclic aging models that consider at least two stress factors. The stress factors relevant in cyclic aging are temperature, charge and discharge current, average state of charge (ØSoC), and depth of discharge (DoD). To allow comparability between individual cell sizes, the current is often represented as the C-rate, which relates the charge and discharge current to the nominal cell capacity. Furthermore, the charge throughput Q and the number of cycles N are the basic stress parameters in cyclic aging.

Considering the semi-empirical models that are summarized in Table 4.1, it is noticeable that they include different stress factors as their model input. This means that individual models have limited applicability to different use cases. An additional challenge is that semi-empirical models often include equations that are not physically based. This can result in an incomplete understanding of the role of specific stress factors on cell aging. The battery capacity loss and internal resistance increase result from a set of aging mechanisms that occur under the operating conditions of a specific application. Without an understanding of the

Source	Cell chemistry	Model input			
		T	I	$\varnothing SoC$	DoD
Baghdadi et al. 2016 [5]	NCA+LMO, NMC	✓	✓		
Cui et al. 2015 [6]	LCO	✓	✓	✓	✓
Hoog et al. 2017 [7]	NMC	✓		✓	✓
Hosen et al. 2020 [8]	NMC	✓	✓	✓	✓
Petit et al. 2016 [9]	NCA, LFP	✓	✓		
Schimpe et al. 2018 [10]	LFP	✓	✓	✓	
Schmalstieg et al. 2014 [11]	NMC			✓	✓
Wang et al. 2014 [12]	NCM + LMO	✓	✓		
Xu et al. 2018 [3]	LMO, LFP, NMC	✓		✓	✓

Table 4.1: Overview of semi-empirical cyclic aging models which consider at least two stress factors with cell chemistry used in the model parametrization and input parameters.

underlying aging processes in different cell chemistries and under different operating conditions, it is not possible to draw reliable conclusions from battery aging data that can be applied in general to other types of systems. Only a few publications include exclusively mechanistically based model equations considering selected stress factors [13–15]. Finally, most cyclic semi-empirical models are parameterized on the entire available measured data set. No distinction and verification of the actual aging mechanisms are made, although this can significantly increase the model extrapolation capability. A step in this direction was made by Schimpe et al. [10] who differentiated between aging at high temperature, low temperature, and high temperature combined with high SoC in the model parameterization. They suspected different aging mechanisms as the cause of varying observed aging processes but did not provide an analysis to confirm the assumption.

To overcome the aforementioned issues, in section 4.2 we present a cyclic battery aging model that describes the capacity loss in graphite-based lithium-ion batteries. The focus was set on the capacity loss, as it often determines when the end of life (EoL) of a battery is reached. The mechanistic model is based on the simplified description of two important aging mechanisms of the graphite anode: solid electrolyte interface (SEI) cracking and reformation as well as active anode material cracking. Thereby, the model incorporates the influence of all the above-mentioned stress factors on the respective aging mechanisms. Furthermore, in section 4.3 we propose a method for the targeted parameterization of the model equations with selected measurement data. The discussed aging mechanisms cause different aging modes: loss of lithium inventory (LLI) and loss of active material at the negative electrode ($\mathrm{LAM_{NE}}$), which have been found to be the major aging modes for capacity loss in aging studies on various graphite-based lithium-ion batteries [16–18]. Incremental capacity analysis (ICA) is used to identify measurements in which LLI is the

dominant aging mode. These exclusively parameterize the base aging mechanism model connected to SEI growth. In section 4.4 the testing procedure on commercial NMC cells providing the parametrization data is introduced. The stress factor levels of the aging measurements are restricted by the operating conditions of a stationary, temperature-controlled battery storage system. The aging mechanism model parametrization is described in section 5.5. Finally, the resulting cyclic aging model is coupled with the calendar aging model from our previous publication [19]. The holistic model is validated on data from a cell aged under a dynamic power profile oriented to the frequency containment reserve operation.

4.2 Holistic capacity loss model

To model the total lithium-ion battery capacity loss, the calendar capacity loss $C_{loss,cal}$ and cyclic capacity loss $C_{loss,cyc}$ are added up using the superposition approach:

$$C_{loss,tot} = C_{loss,cal} + C_{loss,cyc}. \tag{4.1}$$

Thus, they are assumed to be independent of each other and overlapping effects including for example the influence of the SEI thickness resulting from calendar aging on the cracking and reforming of the SEI during cyclization are neglected.
The calendar aging model was introduced and parameterized in our previous study [19] (see chapter 3). The model equations are based on modeling the aging mechanism SEI formation, which dominates the calendar aging. Rising Temperature and higher battery SoC accelerate the capacity loss. The cyclic aging model is defined below.

4.2.1 Cyclic aging model

The presented cyclic aging model describes the macroscopic capacity loss of the battery by simplified modeling of two microscopic anode aging mechanisms: SEI cracking and reforming and cracking in the anode active material. The capacity loss of the battery caused by cyclization is determined by the sum of the capacity losses due to the individual aging mechanisms

$$C_{loss,cyc} = C_{loss,SEI} + C_{loss,AM}. \tag{4.2}$$

The considered stress factors affecting cyclic aging are DoD, average SoC, current I, and temperature T. The cycled charge Q in Ah provides the cyclic aging model basis. It is used to determine the number of equivalent full cycles (EFC)

$$EFC = \frac{Q}{2 \cdot C_{nom}}, \tag{4.3}$$

which relates to the nominal cell capacity C_{nom}. One equivalent full cycle corresponds to the charge that flows in a complete charge and discharge process. Fig. 4.1 gives an overview of the model configuration. It shows the considered input stress factors, the aging mechanisms modeleled, the connected aging modes - which are relevant for the identification of parametrization data - and the model output, which is the battery capacity loss. In the following, we describe the aging mechanisms and related stress factors considered in this work and define the model equations for the cyclic capacity loss.

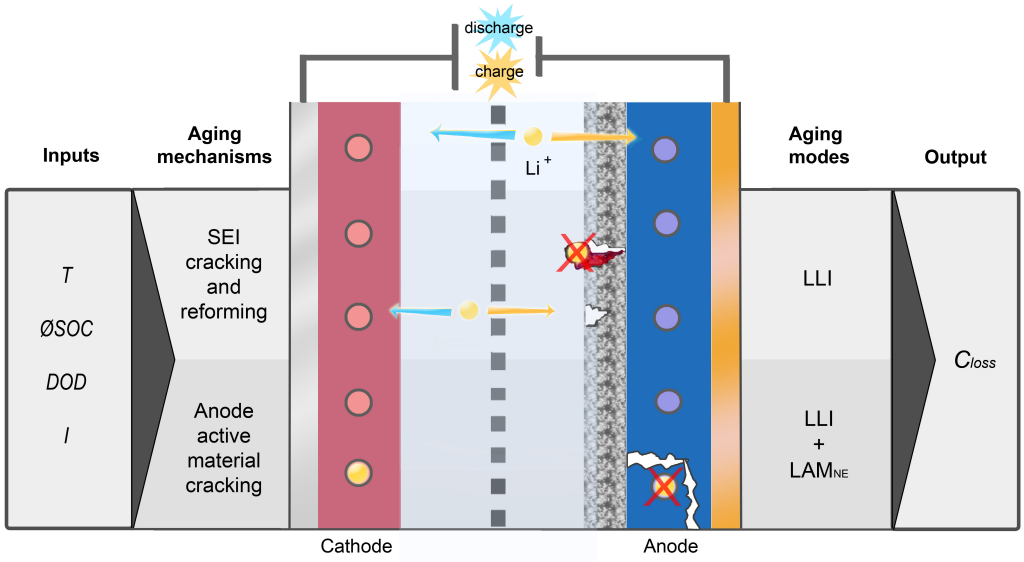

Figure 4.1: A model overview. Left: Stress factors considered in modeling the two aging mechanisms under consideration. Middle: Visualization of the anode aging mechanisms. Right: Associated aging modes which are evaluated for the targeted parameterization, and model output.

SEI cracking and reforming

The passivating SEI layer existing due to the formation process and calendar aging is subjected to mechanical stress due to the expansion and contraction of the active material during cyclization. Cracks develop, which leads to an increase in the SEI surface area. On the enlarged surface, more SEI can grow. If the cracks are deep

enough, the carbon anode surface is exposed to the electrolyte and new SEI forms instantaneously. Thus, as the cracks open and close during cyclization, further SEI is continuously formed [20, 21]. In the SEI reaction, electrolyte components irreversibly react with lithium from the anode, resulting in a loss of lithium inventory [22–24]. The quantity of this LLI and the associated capacity loss depends on several stress factors. The mechanical stress due to volume expansion of the anode changes with the DoD and average SoC of a charge and discharge cycle. In addition to mechanical effects, the chemical SEI reaction kinetics is relevant. The reaction is accelerated with higher temperature and lower anode potential, which means higher battery SoC. The SEI growth further increases with higher currents. In particular, the charging current is relevant, since the SEI growth is partially suppressed during discharge [22, 25]. The stress factor-dependent model equations for capacity loss due to SEI growth are presented below. Following recent aging studies, the effect of the current rate on capacity loss due to SEI growth can be assumed negligible [26]. It is considered indirectly by the temperature dependency due to the coupling between the current rate and temperature rise.

EFC dependency

The diffusion-limited SEI growth and associated capacity loss are proportional to the square root of time. During long-term cyclization, it is possible to observe a transition from square root dependent to linear capacity loss. This can be explained by the transition between diffusion- and migration-limited SEI growth with a certain SEI thickness [22] or repeated SEI cracking and reforming [27, 28]. To encompass this changing long-term aging behavior, the exponent of EFC dependency c_1 is determined empirically. The resulting model equation is

$$C_{loss,SEI}(T, \varnothing SoC, DoD, EFC) = \alpha(T, \varnothing SoC, DoD) \cdot EFC^{c_1} \text{ with } 0.5 \leq c_1 \leq 1. \quad (4.4)$$

The scaling function $\alpha(T, \varnothing SoC, DoD)$ is defined by the multiplicative combination of independent stress factor dependent functions.

Temperature dependency

The temperature dependency of the SEI reaction kinetics follows the Arrhenius law [7, 29]. It is added to equation 4.4 as temperature dependency of alpha, which results in

$$C_{loss,SEI}(T, \varnothing SoC, DoD, EFC) = \beta(\varnothing SoC, DoD) \cdot e^{\frac{-E_a}{R \cdot T}} \cdot EFC^{c_1}. \tag{4.5}$$

with the ideal gas constant R and the activation energy of the SEI reaction E_a. The remaining scaling function $\beta(\varnothing SoC, DoD)$ is determined in the following.

DoD and ∅SoC dependency

The DoD and average SoC at cyclization affect the volume expansion of the graphite active material and thus the mechanical stress leading to cracking of the SEI. In the following, an expansion function is defined based on the anode volume change with lithiation. An analogous function has already been used in various electrochemical and mechanical models [21, 30] and is in this work transferred to a semi-empirical model. When the battery is charged, the lithium-ions move into the gaps between the carbon layers and increase their distance by about 13% [31]. Due to the high energy required to open a layer, the lithium-ions do not distribute homogeneously, but rather leave free spaces between the occupied layers. Therefore, the lithiation happens in several consecutive phases, which are determined over periodic unoccupied layers between layers with high lithium concentrations. This stepwise intercalation of lithium in graphite is also reflected in the volume expansion of the anode. Schweidler et al. [31] investigated the change in graphite volume during lithiation and assigned individual intercalation stages and phase transformation regions to it. Fig. 4.2a shows the related percentage volume expansion of graphite as a function of the lithium concentration x in the hexagonal crystal structure of graphite Li_xC_6. Furthermore, the relative volume change is shown. Based on this, we define a SoC dependent expansion function f_{exp}. For several reasons, 100% SoC of the battery does not have to correspond to 100% lithiation of the anode. First, the graphite anode in lithium-ion batteries is usually oversized. For the cells used in this study, it was determined to be about 5% more anode than cathode capacity in an initial cell opening [19]. Second, during the aging of the battery, the anode capacity and the number of available mobile lithium-ions change. Thus, the maximum possible lithiation of the anode at a given battery SoC changes with aging. Assuming that the cells under consideration have neither LLI, nor LAM_{NE} at the beginning of the battery aging, 100% SoC of the battery is equated to 95% lithiation of the anode, corresponding to the identified overhang. The expansion

function is defined over fitting the relative volume change of the anode as a function of the SoC with a seventh-degree polynomial

$$f_{exp}(SoC) = n_1 \cdot SoC^7 + n_2 \cdot SoC^6 + n_3 \cdot SoC^5 + n_4 \cdot SoC^4 + n_5 \cdot SoC^3 + n_6 \cdot SoC^2 + n_7 \cdot SoC + n_8. \quad (4.6)$$

with the coefficients shown in Table 4.2.

Coefficient	n_1	n_2	n_3	n_4	n_5	n_6	n_7	n_8
Value	2.74	-8.39	8.38	-2.39	-5.05	9.70	0.02	-6.19
Power of 10	10^{-13}	10^{-11}	10^{-9}	10^{-7}	10^{-6}	10^{-5}	-	10^{-3}

Table 4.2: Expansion function fitting parameters.

The Graphite volume change data and the fitted SoC dependent expansion function are shown in Fig. 4.2a. The polynomial choosen, is able to describe the important parts of the volume change including the nearly linear start of the volume expansion, the plateau at medium SoC and the flattening volume change at high SoC. To allow a qualitative comparison of the mechanical stress at different operating conditions, the mechanical stress amplitude σ is defined by the difference of the expansion function values at the maximum and minimum SoC of a cycle

$$\sigma(\varnothing SoC, DoD) = f_{exp}(\varnothing SoC + \frac{DoD}{2}) - f_{exp}(\varnothing SoC - \frac{DoD}{2}). \quad (4.7)$$

Figure 4.2b illustrates the stress amplitude dependency on DoD and average SoC at 50% ∅SoC and 5% DoD respectively. It monotonically increases with the DoD. The flattening of the stress amplitude at high DoD is due to the decreasing volume expansion at high battery SoC, when nearly all graphite layers are occupied (Fig. 4.2a). The SoC dependency reflects the typical parabolic stress factor correlation in the range between 10% and 70% SoC, which has been qualitatively detected in a wide variety of aging studies [4]. At 40% SoC the stress amplitude reaches its minimum within the plateau in the graphite volume change. Furthermore, there is a maximum at around 80% SoC after which the mechanical stress decreases. This again relates to the flattening volume expansion of the graphite material at higher degrees of lithiation. The flattening of the stress amplitude below 10% SoC has no physical meaning. It is caused by the use of the chosen seventh-degree polynomial describing f_{exp}. Since batteries are in practice rarely cycled at those low states of charge, this is tolerated.
The capacity loss due SEI reformation is assumed to be proportional to the stress amplitude σ. According to the Paris Law from fracture mechanics a crack in a

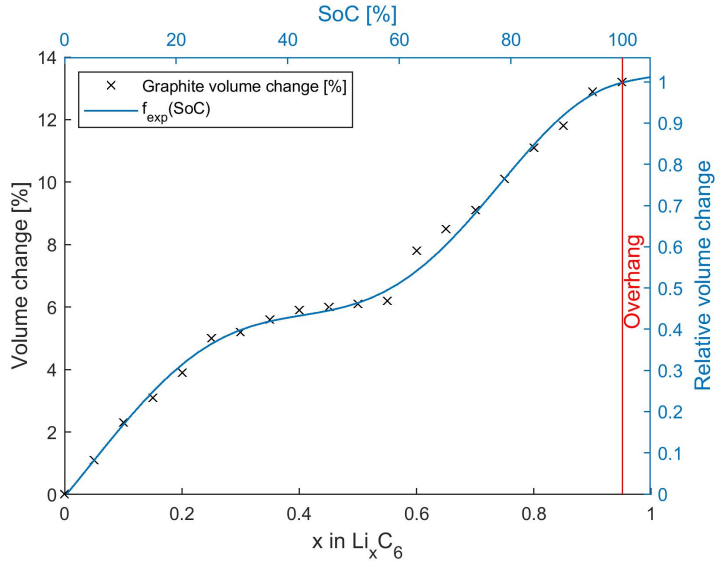

(a)

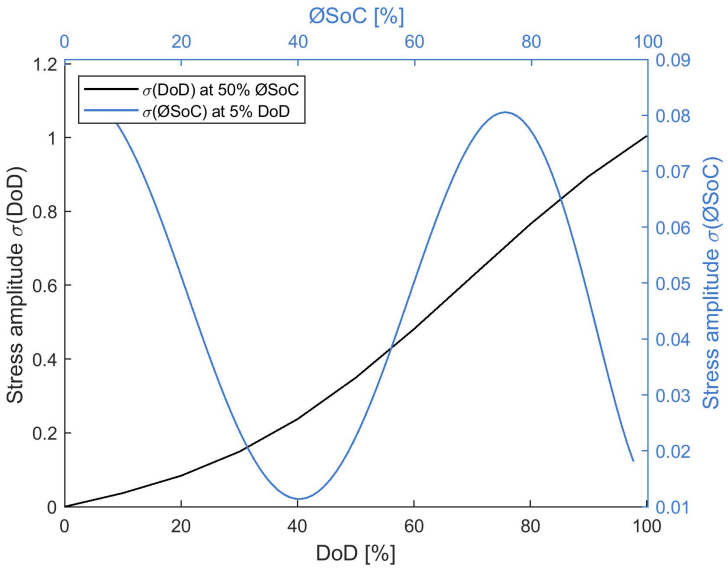

(b)

Figure 4.2: Graphite expansion function and mechanical stress amplitude σ. (a) Volume change of the graphite anode as a function of lithium concentration plotted with data from Schweidler et al. [31] and relative volume change (expansion function) versus battery SoC for a fresh battery cell. (b) DoD and ∅SoC dependent stress amplitude at 50% average SoC and 5% DoD respectively.

material grows exponentially with the number of fatigue cycles. However, the SEI crack growth is limited. If the anode material is exposed, new SEI reforms directly. Furthermore, smaller cracks can heal through reforming SEI. For this reason, it is expected that the SEI cracks only reach a certain depth under small mechanical stress. The maximum crack depth and thus the increase in SEI surface area and SEI growth are assumed to be proportional to the mechanical stress which is expressed by the stress amplitude. With that the model equation 4.5 is extended to

$$C_{loss,SEI}(T, \varnothing SoC, DoD, EFC) = c_2 \cdot \sigma(\varnothing SoC, DoD) \cdot e^{\frac{-E_a}{R \cdot T}} \cdot EFC^{c_1} \tag{4.8}$$

with the scaling coefficient c_2.
The SEI growth is also dependent on the chemical reaction kinetics. In graphite anodes, SEI formation occurs at nearly any SoC when the anode potential is below the reduction potential of the electrolyte. The reaction probability increases as the anode potential decreases [22, 23]. For this reason, various calendar aging studies have shown a capacity loss with a SoC dependency characteristic of the anode potential [23, 32]. In calendar aging, the anode potential corresponds to the anode Open Circuit Voltage (OCV). However, in cyclic aging, it is made up of the OCV and the overvoltage due to the current flow during cycling. To keep the model as simple as possible, no OCV or overvoltage models are included. Instead, it is assumed that the anode potential decreases proportionally to the SoC increase. This approximation is justified for above 20% SoC, before the steep increase of the anode potential occurs. Following the Tafel equation, the acceleration of the SEI reaction can be described by an exponential relationship

$$E(\varnothing SoC) = c_3 \cdot e^{c_4 \cdot \varnothing SoC} \tag{4.9}$$

with the model parameters c_3 and c_4. For simplification, the equation refers to the average SoC of a cycle instead of the actual SoC at cyclization. In contrast to this, some battery cells show a flattening capacity loss at higher SoC [19]. This could be attributed to parasitic cathode reactions, which cause a reversible capacity gain through re-intercalation of lithium-ions into the cathode and thus reduce the measured capacity loss at high SoC [23]. Since cathode reactions are not separately considered in this model, the SoC dependency of the SEI growth is adjusted to be able to model the measured capacity loss. To describe the transition from an exponential to a saturating process, a sigmoidal function

$$S(\varnothing SoC) = \frac{1}{1 + e^{-c_3 \cdot (\varnothing SoC - c_4)}} \tag{4.10}$$

would be suitable. The amplitude of the scaling function is one, c_3 influences the slope to reach this amplitude and c_4 is the shift of the inflection point in x-direction. When the model is restricted to a specific SoC range, a linear function

$$L(\varnothing SoC) = c_3 \cdot \varnothing SoC + c_4 \tag{4.11}$$

can also be sufficient to describe the acceleration of the SEI reaction with the battery state of charge. By coupling of the SoC dependence of the SEI reaction kinetics with equation 4.8, the final model equation for capacity loss due to SEI growth under cyclization

$$C_{loss,SEI}(T, \varnothing SoC, DoD, EFC) = c_2 \cdot \sigma(\varnothing SoC, DoD) \cdot e^{\frac{-E_a}{R \cdot T}} \cdot EFC^{c_1} \cdot \begin{cases} E(\varnothing SoC) \\ S(\varnothing SoC) \\ L(\varnothing SoC) \end{cases} \tag{4.12}$$

is obtained. The decision to choose an exponential, sigmoidal or linear SoC dependency must be made individually for each cell chemistry and stress factor range under consideration. The explicit formulation is applied in the model parameterization with data from cyclic aging tests at static stress factors. To model the capacity loss under dynamic aging conditions, the differential equation

$$\frac{\partial C_{loss,SEI}}{\partial EFC} = c_2 \cdot \sigma(\varnothing SoC, DoD) \cdot e^{\frac{-E_a}{R \cdot T}} \cdot c_1 \cdot EFC^{c_1 - 1} \cdot \begin{cases} E(\varnothing SoC) \\ S(\varnothing SoC) \\ L(\varnothing SoC) \end{cases} \tag{4.13}$$

is used.

Anode active material cracking

With repeated expansion and contraction of the anode during cycling, cracks form in the active material. These lead to areas of active material, being no longer available for the reversible storage of lithium during cycling. This is associated with a capacity loss if the affected electrode is the capacity limiting electrode. Furthermore, the inactive areas of the material can be lithiated, resulting in a combination of LAM and LLI. The capacity loss due to cracking in the anode active material caused by mechanical stress during cyclization is modeled as a function of the stress factors DoD, average SoC and current during cyclization. The dependency of the graphite anode volume change on DoD and SoC has already been explained in section 4.2.1. With higher currents, lithium concentration gradients build up in the active material, leading to increased mechanical stresses. Furthermore, the active material cracking

is accelerated by a lower temperature as the decreasing diffusion coefficient promotes the formation of lithium concentration gradients. The mechanical properties of graphite itself do not change in the temperature range between 10°C and 45°C [20]. For a temperature-controlled battery storage system, the effect of temperature is implicitly considered by investigating the current dependency.

EFC, DoD and ∅SoC dependency

The crack growth rate can be described by the Paris law of fracture mechanics for sub-critical crack growth

$$\frac{\partial a}{\partial N} = C \cdot (\Delta K)^m. \tag{4.14}$$

The power function describes the change in crack depth a with the number of fatigue cycles N. C and m are empirical material constants and ΔK corresponds to the span of the stress intensity. The latter depends not only on the stress amplitude at volume expansion, but also on the pre-existing crack depth. If the crack opening occurs perpendicular to the crack surface, the stress intensity factor K can be assumed to be proportional to the root of the crack depth [20]. The span of the stress intensity is consequently given by

$$\Delta K = \epsilon \cdot \sigma_t \cdot \sqrt{a} \tag{4.15}$$

with the empirical pre-factor ϵ and the tensile stress σ_t. The capacity loss caused by active material cracking, is assumed to be proportional to the crack depth when the number of cracks remains constant. The differential formulation of the model equation for the capacity loss due to cracking in the anode material $C_{loss,AM}$ is defined analogously to the Paris law

$$\frac{\partial C_{loss,AM}(\varnothing SoC, DoD)}{\partial EFC} = c_5 \cdot (\sigma(\varnothing SoC, DoD) \cdot \sqrt{C_{loss,AM}})^m \tag{4.16}$$

with the empirical model coefficients c_5 and m.

Current dependency

Compared to modeling the SEI growth or formation of lithium plating, there are significantly fewer validated studies modeling current rate dependent crack formation in the active material [33]. Purewal et al. [20] derived a proportionality between cell current and tensile stress at the particle surface based on Fick's second law of diffusion. Analogously, the span of the stress intensity ΔK is extended by a

linear current dependency. For the capacity loss change with the number of EFC it follows

$$\frac{\partial C_{loss,AM}(\varnothing SoC, DoD, I)}{\partial EFC} = c_5 \cdot (I \cdot \sigma(\varnothing SoC, DoD) \cdot \sqrt{C_{loss,AM}})^m \tag{4.17}$$

with the primitive function

$$C_{loss,AM}(\varnothing SoC, DoD, I) = \\ \frac{1}{I^2 \cdot \sigma(\varnothing SoC, DoD)} \cdot \left(\frac{-EFC \cdot (m-2) \cdot c_5 \cdot \sigma(\varnothing SoC, DoD)^2 \cdot I^2}{2} \right)^{\frac{-2}{m-2}} . \tag{4.18}$$

For a physically meaningful result - a capacity loss that gradually increases with the number of cycles - the parameter m must be in the range between two and zero.

Passive anode effect

In addition to the aging mechanisms, the passive anode effect (PAE) is considered in the model parametrization. The PAE can have a significant influence on the detected capacity loss depending on the cell SoC before and during aging [34, 35]. It originates from the common practice of overdimensioning of the graphite anode compared to the cathode which results in anode sections having no direct cathode counterpart. Lithium concentration differences between active and passive part of the anode (also called overhang) slowly equilibrate by diffusion. If the concentration in the active part of the anode is higher than in the passive part, lithium diffuses into the overhang region. On the other hand, if the lithium concentration in the active part of the anode is lower, it is lithiated from the overhang. The equalization process and thus the complete PAE occurs in a period of days to months depending on factors such as temperature, the potential difference between the active and passive anode parts and the dimensioning of the overhang. However, the main contribution of the PAE is detectable in the time period directly after setting a new battery SoC, when the potential difference of active and passive anode is the highest [36, 37]. The lithium diffusion processes cause a reversible capacity loss or gain. The consideration of PAE is relevant in many studies, especially when the accurate prediction of the currently available battery capacity is required [23, 29]. When modeling the overall lifetime of battery systems, the contribution of PAE to the total capacity loss is only small. Anyway, it needs to be considered in the lifetime model parametrization with experimental data. Neglecting it can lead to an over- or underestimation of SoC-dependent model parameters and thus significantly influence the results of the

lifetime modeling. Depending on the model objective, there are various options for considering the PAE: 1. Include the PAE as a part of the aging model [23], 2. Reduce the PAE on cell characterization results by storing the cell at the SoC of the following storage or average SoC for a following static cycling period [35], 3. Include the PAE as an offset in the model parameterization. In the presented work, the capacity loss or gain due to the PAE $C_{loss,PAE}$ is added to the capacity loss model as an offset:

$$C_{loss,cyc} = C_{loss,SEI} + C_{loss,AM} + C_{loss,PAE}. \tag{4.19}$$

This approach assumes that most of the capacity gain or loss due to the PAE already occurred within the time range between the first and second cell characterization in the related battery aging measurements. The exchange of lithium in a time step is proportional to the potential difference between the active and passive parts of the anode [23, 37]. The PAE capacity loss is approximated by a linear SoC-dependent function

$$C_{loss,PAE}(SoC_0, \varnothing SoC) = c_6 \cdot \varnothing SoC - c_6 \cdot SoC_0 \tag{4.20}$$

With prior knowledge of the initial cell SoC before cyclization SoC_0, the zero crossing of the capacity loss due to PAE can be specified. The slope of the linear function c_6 is empirically determined.

4.3 Aging mode identification for model parametrization

As shown in Fig. 4.1, the presented model differentiates between two aging mechanisms that are coupled to different aging modes. This distinction allows a targeted parameterization of model equations with selected measurements in which only associated aging modes occur. While aging mechanisms are difficult to separate without extensive investigations such as post-mortem analyses, different aging modes can be identified by using incremental capacity analysis [16]. The incremental capacity (IC) is determined by the ratio of the change in charge to the change in voltage in a time step. With a smaller battery voltage change the value of IC increases. Therefore, battery cell voltage plateaus are displayed as peaks in the IC curve. Fig. 4.3a shows the IC curve of a typical NMC cell. The three main peaks are marked as peak one, two and three respectively. As for most graphite-based cells, the peaks are primarily determined by the anode potential and can be related to graphite anode phase equilibria [16, 38].

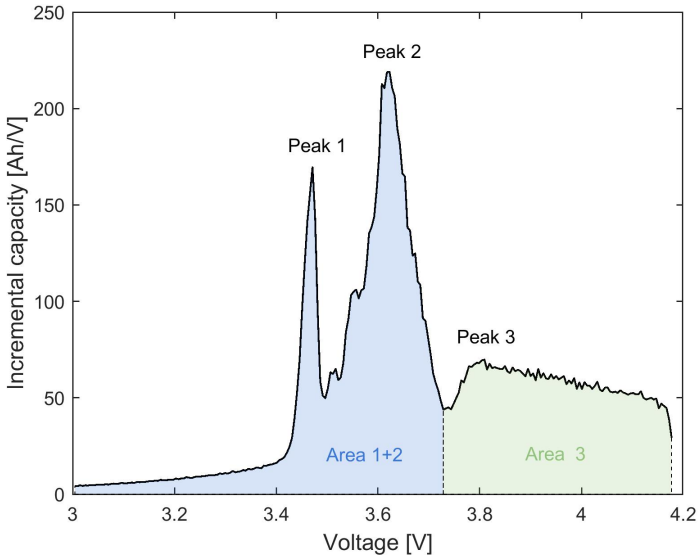

(a)

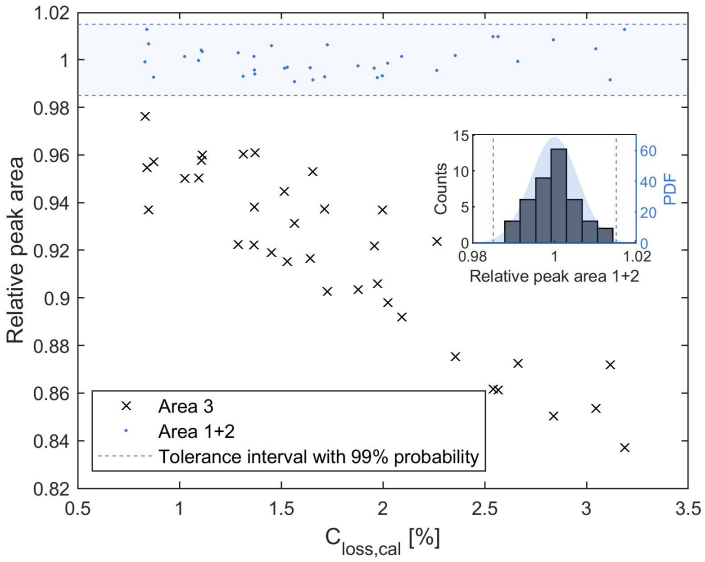

(b)

Figure 4.3: Incremental capacity analysis (ICA) method. (a) Incremental capacity plotted over the cell voltage. The peak areas evaluated in the ICA are marked as area 1+2 and area 3. (b) Relative peak area over the capacity loss of six NMC cells calendar aged at 40°C and 50%, 70%, and 90% SoC respectively. The lines indicate the range with a 98% probability, that a measured area 1+2 value lies within the tolerance interval. It was determined from the standard deviation and mean value of the probability density function (PDF) also shown.

The features of interest that include peak height, position, and area are analyzed in the ICA. The peak position is affected by a change in polarization resistance. With higher polarization resistance, the battery overvoltage increases and the IC peaks shift to higher voltages at charging and lower voltages at discharging. The area under a peak corresponds to the capacity stored in the associated voltage range. The peak height changes either as the peak area decreases or due to the broadening of the peaks as the kinetics of charge transfer reactions in the battery slow down. Therefore, the peak height is sensitive to capacity loss and an increase in resistance. Since the target variable of the presented aging model is the battery capacity, the peak area is evaluated to assess the aging modes.

Detailed modeling of the effect of aging modes on the features of interest in different cell chemistries can be found in literature [16, 39]. In the case of LAM, the anode or cathode loses active material and thus electrode capacity. Consequently, the individual phase transitions in the electrodes are reached more quickly. This leads to a decrease of the corresponding area of each peak formed by the electrode potential. For the example of an NMC battery, the anode phase equilibria can be clearly distinguished and LAM_{NE} can be identified by a decrease in the area of all IC peaks. At dominating LAM_{PE} the cathode terminates the battery discharge, which especially leads to a decrease of the first IC peak area. In the case of LLI, the graphite anode is filled with fewer lithium-ions during charging, which means that only the area of the third IC peak would show a decrease. Conversely, this implies that as soon as the area of peaks one and two decreases, another aging mechanism beyond LLI would be present. This applies until LLI has progressed so far that the third peak disappears and the LLI starts to proportionally reduce the second IC peak.

The change in the peak areas is evaluated by integrating the IC in the peak voltage interval. The respective voltage window is limited by the minimum between peaks two and three as shown in Fig. 4.3a. In the case of LLI, the area of the third peak decreases while that of the other peaks remains constant. To confirm this effect, calendar aging data can be used. In calendar aging, SEI formation is the dominant aging mechanism and thus LLI is the prevailing aging mode. In Fig. 4.3b the evolution of the relative peak areas is plotted over the capacity loss of six NMC cells calendar aged at an elevated temperature of 40°C and different SoC [19]. The data are presented without error bars since it is assumed that the measurement noise on the IC curve largely averages in the integration process. A systematic offset of the results due to measurement errors is not relevant since the area change and not the absolute area value is considered. As expected, the relative area of the third peak decreases with increasing capacity loss, while the grouped area of peaks one and two remain relatively constant. The spread of the area 1+2 around the expected value of one is influenced by random measurement errors and the cell-to-cell variation.

As shown in the histogram in Fig. 4.3b it is almost symmetrical and can assumed to be normally distributed. The corresponding standard deviation is $5.8{\cdot}10^{-3}$. The specified tolerance intervals indicate the deviation from the expected value of one, in which 98% of all measured values can be found. If additional LAM was present, all IC peaks would lose area and the marked limits of the grouped peak one and two area would continuously be exceeded by the measured relative peak areas. These criteria can be applied in all graphite-based lithium-ion battery cells, provided that the graphite peaks are clearly identifiable.

4.4 Material and methods

This section provides a detailed description of the used cells, measurement systems and methods to allow reproduction of the results.

4.4.1 Cell specification and testing system

The tested batteries were Li(NiMnCo)O_2 (NMC) /graphite pouch cells with a nominal capacity of 64 Ah. The cell voltage is limited to 3 V at discharge and 4.2 V at charge. The cells were obtained from a battery module that was subjected to a few charge and discharge cycles and one year of storage at about 50% SoC. The cycling and characterization of the cells was done with a Maccor 4000 battery tester. The corresponding measurement errors are $\Delta U = \pm 0{,}2$ mV for the voltage and $\Delta I = \pm 3$ mA for the current. The uncompressed single cells were tested in three VC 7018 Vötsch climatic chambers that maintained the ambient temperature constant with a tolerance of 1°C. The cells were randomly distributed among the individual climatic chambers and measurement channels. To reduce the deviation between results of the single cell measurements, the screws connecting the power cable and cell contacts were tightened with a fixed torque of 25 Nm and 1.2 Nm, adapted to the diameter of the used screw threads.

4.4.2 Test matrix

In the cyclic aging test series, 14 cells were cycled with constant stress factors. After every 100 capacity cycles, a cell characterization was performed. The stress factors were limited with respect to a temperature-controlled stationary storage system providing grid frequency containment reserve. Therefore, all tests were done at

23 °C climatic chamber temperature. The DoD range studied was between 0 and 100% DoD with various DoD steps. The average SoC, related to the current cell capacity, was examined especially at high SoC at three levels of 50%, 70% and, 90% SoC. The focus was set at high SoC that are particularly relevant for hybrid systems consisting of the combination of a battery storage with an energy sink. The cycling was done symmetrically with equal charging and discharging current rates at a maximum of 2C. An overview of all the stress factor combinations used in the test series is summarized in Table 4.3.

No.	DoD [%]	∅SoC [%]	C-rate [1/h]	Correction $C_{loss,char}$	Aging modes
1	5	50	0.5	✓	LLI
2	10	50	0.5	✓	LLI
3	20	50	0.5	✓	LLI
4	40	50	0.5	✓	LLI
5	50	50	0.5	✓	LLI
6	60	50	0.5	✓	LLI
7	80	50	0.5		LLI + LAM
8	90	50	0.5		LLI + LAM
9	10	70	0.5	✓	LLI
10	10	90	0.5	✓	LLI
11	10	70	1.25	✓	LLI
12	10	70	2	✓	LLI
13	100	50	2		LLI + LAM
14	30	50	0.5	Excluded*	LLI + LAM

*because of measuring channel failure

Table 4.3: Cycle aging test matrix including stress factors of the individual measuring points. The indication whether capacity loss due to the characterization measurement is corrected and the assigned aging modes are results from sections 4.5.1 and 4.5.2. They have been added here to facilitate the results assignment to individual stress factor settings.

4.4.3 Dynamic validation profile

For model validation, one cell was exposed to a dynamic power profile adapted to frequency containment reserve operation. The validation profile is based on seven days of European frequency data starting on 10 October 2019. In FCR provision, the battery power scales linearly with the grid frequency deviation of 50 Hz. At a deviation of 0.2 Hz the maximum prequalified power is demanded. For the considered system configuration, the single cell maximum power is about 300 W, which corresponds to a current rate of about 1.3C at 3.68 V nominal cell voltage. In addition, rules and degrees of freedom for the provision of FCR were considered calculating the power profile [40]. These are not the focus of this paper

and therefore will not be discussed further. The start and target battery SoC in the dynamic validation profile is 50% SoC.

4.4.4 Characterization

At the start of the test sequence, a preconditioning was performed that includes five complete charge and discharge cycles at 1C. This was followed by an initial cell characterization that includes a capacity measurement, a pulse test and a slow discharge with 1/10C to determine the IC. The capacity measurement started with a constant current (CC) charge at 1C. When the charging voltage was reached, a constant voltage (CV) step was used until the current rate was less than 1/20 C. The cell was then CC discharged again at 1C. This was repeated twice with a half hour break for relaxation after each charge or discharge step. The subsequent pulse test was performed at 10%, 50%, and 90% SoC respectively. The cells were charged at 1C until a target SoC was reached. After an hour of rest, the cells were discharged with a 1C pulse for 10s. This was followed by a 30s rest and a charging pulse with 1C over 10s. Then the cells were charged to the next target SoC and the test sequence was repeated. Finally, the cells were fully charged with a CCCV protocol. After another 30 minutes rest period, a discharge with 1/10C completed the characterization measurement.
To investigate the capacity loss due to cell characterization, a periodic characterization measurement was carried out on two cells. It consisted of 15 consecutive characterization measurements with a rest time of 30 minutes between each characterization.

4.5 Results and discussion

In this section, we present the experimental and theoretical results. At first, the experimental data processing is explained. Then, the aging mode identification is done using the IC method introduced. Afterwards, the aging mechanism model equations are parametrized with data including the corresponding aging modes. Finally, the complete model with cyclic and calendar aging is validated using dynamic FCR aging data.

4.5.1 Data processing

In data preprocessing, we correct the capacity loss measured for the capacity loss due to cell characterization by subtraction as introduced in our previous study [19]. Furthermore, the calendar aging was subtracted. The calendar aging capacity loss is modeled in one-second timesteps using the equations attached in **??** and the SoC and temperature data recorded during cyclic aging. The capacity loss due to the characterization $C_{loss,char}$ was determined from the periodic characterization measurement on two separate cells. The cells show an initial capacity gain, which reaches its maximum of 0.15% after three characterizations. It can be attributed to a reduction of the polarization resistance due to electrode surface expansion under mechanical stress in cyclization [19]. An influence of PAE is assumed to be negligible due to the agreement of the initial cell SoC (50% SoC) with the average SoC of the characterization measurement cycles. The subsequent characterization capacity loss mean value was fitted by using the linear function $C_{loss,char} = 0.04 \cdot N - 0.31$ for extrapolation. In cyclic aging, the battery is permanently exposed to mechanical stress. Hence, $C_{loss,char}$ cannot be clearly distinguished from the capacity loss due to cyclization. Nevertheless, the capacity gain and loss due to characterization can significantly influence the results of cyclic aging tests – particularly at cyclization with small DoD, where the capacity loss of the battery differs only slightly from that in calendar aging. Therefore, all measurements where the cyclic capacity loss in the third characterization was changed by more than 20% after subtracting $C_{loss,char}$(N) were corrected by the capacity loss share of the characterization measurement. For the other measurements, the influence of the characterization was assumed to be negligible. Which measurement data were corrected by the capacity loss due to characterization is noted in Table 4.3 in section 4.4.

4.5.2 Assignment of the aging modes

To select the measurements in which the basic aging mode LLI dominates, the ICA method introduced in section 4.3 is used. Fig. 4.4 shows the relative peak area of the analyzed IC peaks 1+2 and 3 plotted over the capacity loss of different cells from the cyclic aging tests. The evaluated IC curves were smoothed with a moving average filter over a sliding window of the length of three measurement values.

The cells that were cycled at 10% and 60% DoD are examples of the identified aging mode LLI. The 10% DoD cell showed only a very small capacity loss of less than one percent within the cyclic aging. No significant drop can be seen in any of the peak areas. DoD 60% is the highest cycling DoD assigned to the LLI aging mode.

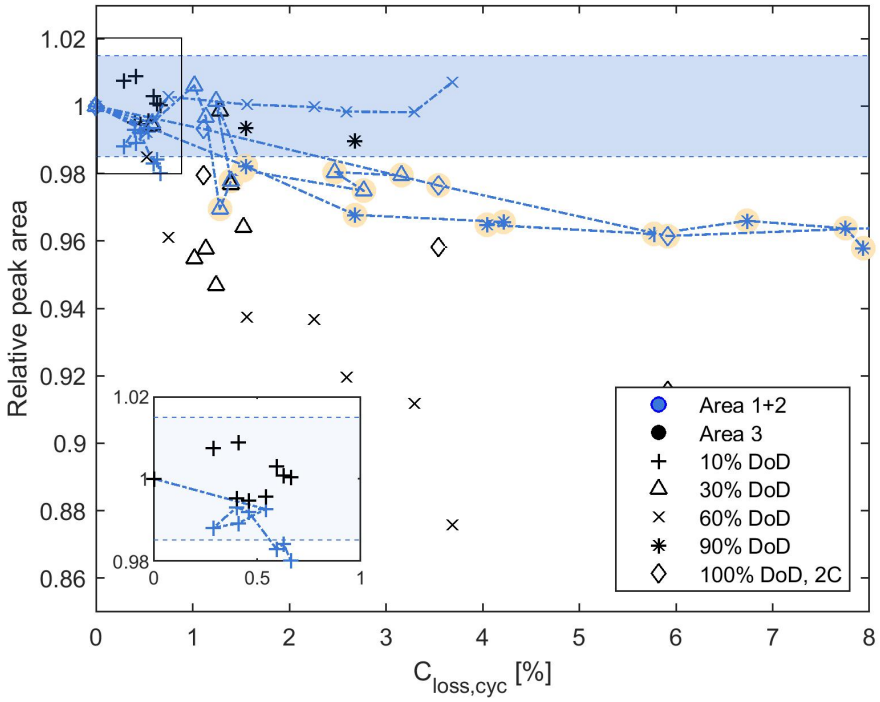

Figure 4.4: Relative IC peak area of peaks 1+2 and 3 over the capacity loss for four example cells cycled at different DoD, 50% ∅SoC , and 0.5C. Furthermore, the 100% DoD, 50% ∅SoC and 2C cell results are shown. The area marked in blue indicates the LLI tolerance interval of peak area 1+2 introduced in Figure 4.3b. A continuous decrease of the peak area 1+2 was detected at the highlighted measurement values. Here, loss of active material (LAM) was identified in addition to the loss of lithium inventory (LLI).

The area of peaks 1+2 does not drop below the area tolerance range identified for LLI until the end of the tests at a capacity loss of about 3.8%. All measurements below 60% DoD were also assigned to the LLI aging mode. An exception is the 30% DoD measurement in which additional LAM was detected in terms of a continuous drop of the peak area 1+2. The cell used for this specific cycle test showed a clear voltage noise to the end of the test series. This could be attributed to a defect of the measurement system channel, therefore the cell was excluded from all further evaluations. Measurements at more than 60% DoD also show a drop in the peak area 1+2 and therefore were assigned to additional LAM. This can be seen in the example of the 90% DoD and the 100% DoD and 2C measurements. The classification of all measurements to the aging modes is shown in Table 4.3 in section 4.4.

4.5.3 Parametrization SEI cracking and reforming

In the following, we use the measurements assigned to the aging mode LLI to parameterize the SEI cracking and reforming aging mechanism model. To reduce the influence of the PAE on the capacity loss EFC dependency, the parametrization includes two optimization steps. First, the dependence of the capacity loss on the number of EFC is determined on cells cycled at 50% average SoC, a current rate of 0.5C, and various DoD. Second, the overall SEI cracking and reforming model equation including the already determined model parameter c_1 is parameterized.

EFC dependency

In the first step, Eq. (4.8) is parametrized, which only considers the mechanical stress DoD and SoC dependency and the chemical temperature dependency. The cell temperature was determined by the mean value of the measured temperature in a cyclization period. The cells heated up only slightly to a maximum of about 24°C during cycling at 0.5C. The activation energy of the SEI reaction was already determined to be 36.36 kJ/mol in the calendar aging of the NMC cells considered [19] and is adopted for the cyclic aging model. The model parameters are determined by minimizing the sum of the squares of the residuals using the MATLAB function *lsqnonlin*. The model results and their absolute deviation from the measured data are shown in Fig. 4.5a. The determined exponent of the EFC dependency c_1 is 0.98. The capacity loss is almost linear, which can be explained by the onset of migration-limited SEI growth [22] or the permanent cracking and reforming in the SEI during cyclization [41]. The mechanical stress amplitude adequately describes the DoD dependence of the capacity loss. The absolute deviation of the modeled from the measured values is mostly below 0.5%. Only the 60% DoD measurement significantly deviates from the model forecast with 1% absolute error after around 650 EFC. The measurement data at 50% and 60% DoD almost coincide, although, according to the mechanical stress function the capacity loss should increase with higher DoD. Since the model sufficiently describes all the other DoD dependencies, this single-cell behavior is not discussed further.

SoC dependency

In the calendar aging of the NMC cells considered, a saturating capacity loss SoC dependence was observed at high SoC. It was described by a linear function in the range above 50% SoC [19]. Accordingly, the linear SoC dependency $L(\varnothing SoC)$ (Eq. (4.11)) is used in the cyclic aging model. To parametrize the SoC dependency of

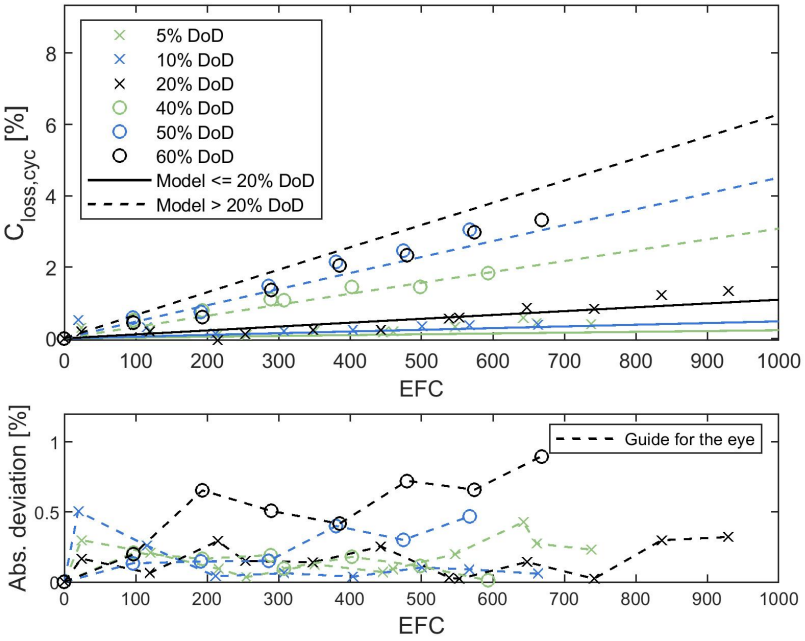

(a)

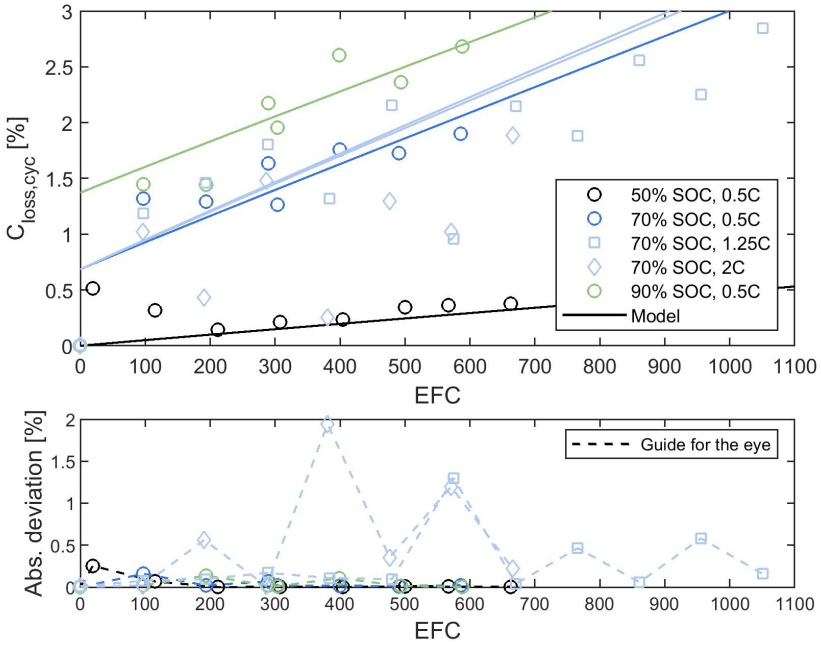

(b)

Figure 4.5: SEI growth model optimization results at (a) different DoD, 0,5C and 50% ∅SoC (b) different SoC, 10% DoD and 0.5C.

the chemical SEI growth in Eq. (4.12), all capacity loss results which were identified for LLI are used (see Table 4.3). Only the measurements at increased current rates and 70% SOC were excluded from the model parameterization due to a significantly increased measurement noise. The capacity loss offset due to the passive anode effect is added to the cyclic capacity loss according to Eq. (4.19) and (4.20). The model parameters resulting from fitting the measured data are shown in Table 4.4. In Fig. 4.5b, the model results at different SoC and 10% DoD are plotted together with the absolute model deviation. The capacity loss at elevated average SoC and a current rate of 0.5C is described with a small absolute error of less than 0.25%. The increased measurement noise at higher current rates and 70% SoC leads to significant absolute errors of the model in comparison to single datapoints. The model assumption that the current rate dependence of the SEI growth is negligible is confirmed by the measured data since no increased loss of capacity is detected with higher current rates. The remaining difference in the model results at 70% SoC is caused by the temperature increase of the cells at cycling with higher current rates.

Symbol	c_1	c_2	c_3	c_4	c_5	c_6	m	E_a
Value	0.98	9.31 $\cdot 10^4$	3.90 $\cdot 10^{-3}$	0.20	4.00 $\cdot 10^{-3}$	34.50 $\cdot 10^{-3}$	1.23	36.36
Unit		%	1/%	%	$h^m\,\%^{1-\frac{m}{2}}$			kJ/mol

Table 4.4: List of cyclic aging model parameters.

Passive anode effect

The slope c_5 of the linear $C_{loss,PAE}$ function was determined to be 34.50$\cdot 10^{-3}$. To check the plausibility of the result, an estimate of the capacity loss and gain due to the influence of the overhang was done by using the slope method presented by Lewerenz et al. 2018 [36]. They linearly extrapolated the irreversible capacity loss after compensation of the anode overhang effect. The offset due to the PAE is determined at the y-axis intercept of the fitted line. The method was verified on calendar-aged cells and is transferred to cyclic aging in this work. This is possible since the aging mechanism SEI formation dominates in the used measurements, which allows the assumption of a linear irreversible capacity loss also in cyclic aging. Fig. 4.6 shows the results of the analysis for the 50%, 70% and 90% ∅SoC measurements. The linear fit was performed on the measured data after the full compensation of the initial PAE, which is assumed to be after at least 300 EFC. That accounts to about two months of aging, depending on the average SoC and DoD of the respective cycles. At 50% SoC the offset of the identified PAE capacity loss is on average -0.02%, with a standard deviation of 0.28%. At 70% SoC and 90% SoC, a capacity loss of 0.76% and 1.49% due to PAE were determined respectively.

Measurements at 70% ∅SoC and current rates above 0.5C were not included in the analysis due to their increased measurement noise. Because of the limitation of the available measurement data, no statistical error evaluation of the could be done here. It could be expected that the error increases at SoC that derivate more from the initial SoC_0 since there are more lithium exchange processes between overhang and active anode taking place. According to Eq. (4.20), the modeled capacity loss offset with 50% initial cell SoC is 0.00% at cycling with 50% average SoC, 0.68% at 70% average SoC and 1.36% at 90% average SoC. The absolute deviation of the offsets determined by the slope method and the model optimization are 0.02%, 0.08% and 0.13% for 50%, 70% and 90% SoC respectively. The modeled values lie within the standard deviation range of about 0.28% and are therefore plausible. It must be noted that we concentrate on states of charge above 50% SoC in the para :ribe cycli

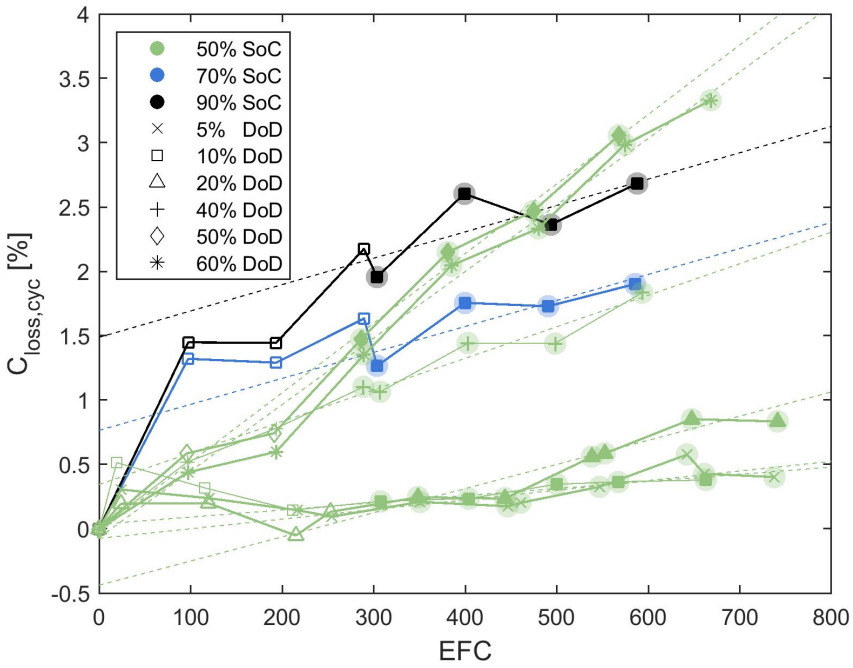

Figure 4.6: Capacity loss plotted over the number of equivalent full cycles (EFC) for cells cycled with different SoC at 10% DoD and 0.5C. The linear extrapolation to estimate the passive anode effect is done on the data with filled or highlighted markers.

4.5.4 Parametrization active anode material cracking

To parameterize the overall model including the active material cracking aging mechanism (Eq. (4.19) inserting Eq. (4.12), Eq. (4.18) and Eq. (4.20)), measurements where LAM was identified beyond LLI are used (see Table 4.3). The final model result and the parametrization data are shown in Fig. 4.7. The capacity loss due to SEI cracking and reformation is marked with a dashed line and the overall capacity loss including active material cracking is marked by a solid line. All model parameters are presented in Table 4.4.

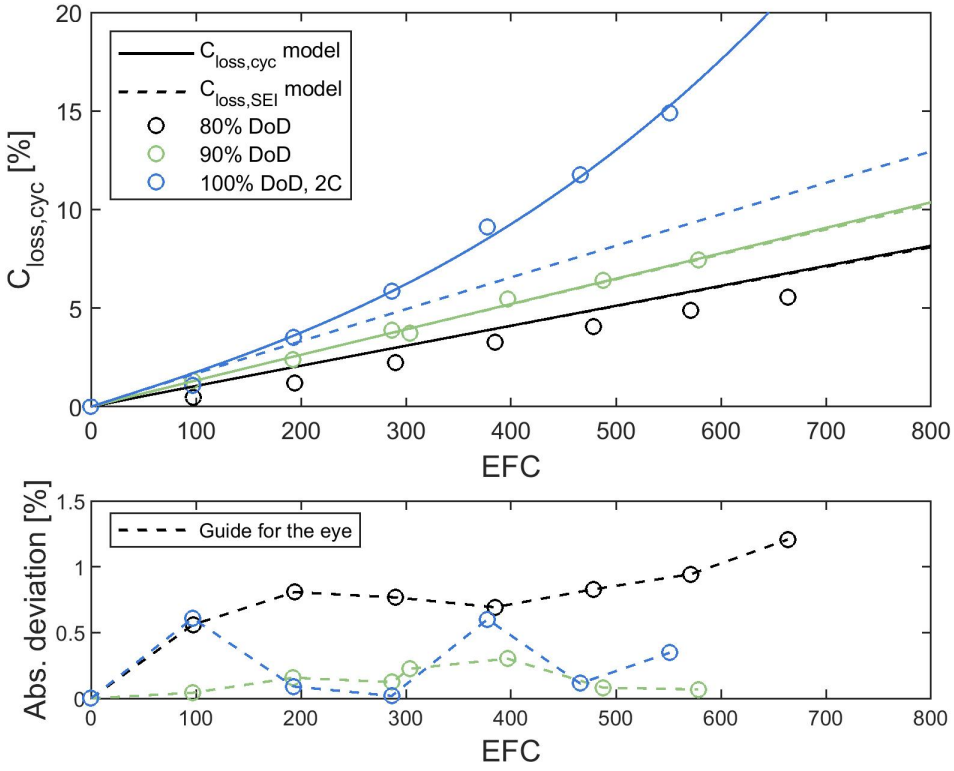

Figure 4.7: Top: Modeled and measured capacity loss at different DoD, 50% ØSoC and 0.5C (unless otherwise specified) over the number of EFC. The cells were identified with additional LAM. Bottom: Total cyclic capacity loss model absolute error over the number of EFC.

The capacity loss of the cell aged at 2C and 100% DoD is particularly striking. The cell reaches its EoL of 20% capacity loss after only about 700 EFC. In addition to the measured capacity loss, an expansion of the cell's volume was observed during and after aging. This indicates gas formation in the battery, which is coupled to electrolyte decomposition, for example in the formation of the SEI [42]. The combination of mechanical stress due to volume expansion of the anode and the lithium-ion concentration gradients building up within the electrode at a high current rate leads to pronounced cracking in the active material which might be

the cause of the rapid cell failure observed. The exponential trend of the capacity loss, which clearly deviates from the SEI model, is well described by the overall model with a mean absolute error of 0.12% capacity loss. The 80% and 90% DoD measurements do not show an exponential increase in capacity loss, although the first signs of LAM can already be detected in the ICA. The LAM is still masked by predominant LLI which is described by the SEI crack model. The capacity loss at 80% DoD is continuously overestimated by a mean absolute deviation of about 0.72% capacity loss. The absolute model error at 90% DoD is small with below 0.5% capacity loss. To further investigate the aging process at rapid cell failure, more long-term measurements at higher DoD and current rates must be carried out in future studies.

4.5.5 Validation

The overall model was validated on a cell cycled with a power profile adapted to the FCR use case. Short power pulses distributed symmetrically on charging and discharging are typical for FCR provision. To model the capacity loss, the average SoC, DoD, current and cell temperature of each cycle contained in the dynamic power profile are evaluated. Firstly, coulomb counting is used to determine the cell SoC for each timestep in the measured dynamic aging profile. Then, the SoC profile is analyzed with the rainflow counting algorithm using the *rainflow* function in MATLAB. The algorithm originates from material fatigue analysis to identify smaller stress cycles within a dynamic stress profile and was already transferred to battery cycling analysis in several battery aging studies [3, 7]. The current rate and temperature are evaluated by the mean value between the start and end times of a counted cycle. In the considered profile, the cycle charging and discharging current rate is always below 0.35C. The mean DoD of all counted cycles is very small with 0.17% DoD. The average SoC of the cycles ranges between a maximum of 65% and a minimum of 20% SoC. A number of EFC is assigned to each identified cycle by the counted charge at its starting time. Since cycles partially overlap, backsteps may occur in the identified EFC vector. To overcome this, the number of EFC is set equal to the previous value in the case of a backstep. This procedure slightly shifts the order of the cycles but simplifies the evaluation of the total calendar and cyclic aging after a certain number of EFC and a time t. Cyclic aging is modeled numerically solving the differential equations (4.13) and (4.17). The aging mechanism capacity loss is then summed up according to Eq. (4.2). The PAE is not considered in the dynamic lifetime estimation. The initial value for the active material cracking capacity loss, which represents the presence of cracks in the anode that grow during cyclization,

is set to $1{\cdot}10^{-6}\%$ $C_{loss,AM}$. The dynamic aging model results and the measured capacity loss are presented in Fig. 4.8. The measurement data were corrected by the capacity loss due to characterization (see section 4.5.1).

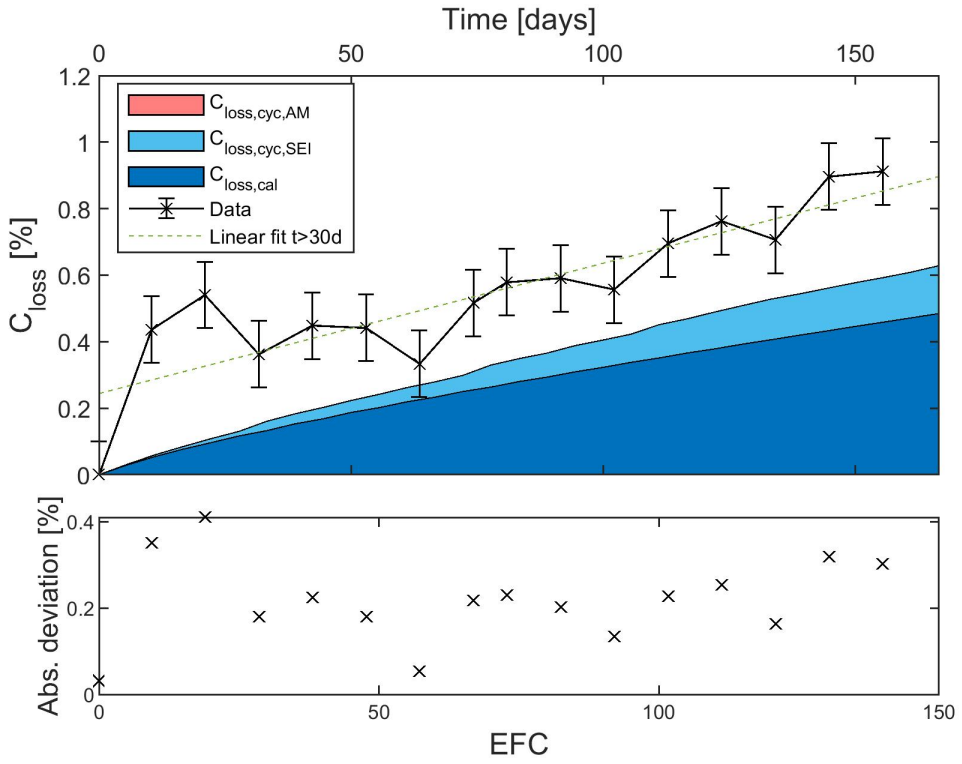

Figure 4.8: Simulated and measured capacity loss for the dynamic validation profile and absolute error over the number of EFC and the cycling time.

The modeled total capacity loss underestimates the measured data of the dynamically cycled cell with a mean absolute deviation of 0.2%. Anyway, the absolute error remains almost constant in the considered time interval. An offset of the measured capacity loss can be caused by cell-to-cell variation or overhang effects. A linear fit of the measured capacity loss after one month of cycling results in a y-axis intercept of 0.24%. An estimate of the PAE would therefore be consistent with the mean absolute error of the model. Calendar aging accounts for 70% of the total capacity loss after 150 EFC and 160 days. However, the modeled portion of cyclic aging can increase by the end of battery life. Cyclic aging is in FCR provision clearly dominated by the aging mechanism SEI cracking and reforming, as expected for cyclization with small DoD and low current rates. The modeled contribution of loss of active anode material is negligibly small with $1.12 \cdot 10^{-6}\%$ capacity loss. Depending on the operating strategy and dimensioning of the storage system, the model predicts a lifetime between 15 and over 25 years until the defined EoL with 20% capacity

loss is reached. The results frame is consistent with FCR storage lifetime estimations from literature [43, 44] and will be discussed in a follow-up publication.

4.6 Conclusion

The semi-empirical cyclic battery aging model presented in this work bases on simplified physical model equations describing the graphite anode mechanisms SEI cracking and reforming and active material cracking. The effect of the acting stress factors DoD, SoC, current, and temperature is discussed in the model derivation. A key point of the work is the targeted parameterization of the model equations. An innovative incremental capacity analysis method is introduced to identify data, in which the aging modes associated with the respective aging mechanism are present. Data in which LLI dominates are used to parameterize the basic aging mechanism coupled to SEI formation. Measurements in which further LAM was identified were used to parameterize the active material cracking model. Using only those data for the model parametrization allows a clear separation of the stress factor sensitivities of individual aging mechanisms which increases the model extrapolation capability. On the considered NMC cells, negligibility of current rate dependence of SEI growth was confirmed, while strong current rate dependence of cracking in the active material was found. The aging mechanism model can describe two phases of cyclic aging. First, the nearly linear capacity loss due to SEI cracking and reforming. Second, the strong non-linear capacity loss represented by cracking in the active material. Finally, the cyclic model was combined with the calendar aging model from our previous publication [19]. The holistic model validation was performed on a battery cell separately aged with a dynamic power profile adapted to frequency containment reserve operation. The cell aging was predicted with a nearly constant absolute deviation of about 0,2% capacity loss. In FCR provision, the capacity loss is largely determined by calendar aging. The aging mechanism SEI cracking and reforming dominates the cyclic loss of capacity. The contribution due to cracking in the active material is negligibly small for the considered cells. The presented aging model can be applied to all graphite-based lithium-ion batteries. It provides a basis for the further development of physically based semi-empirical models and can be extended by further aging mechanisms depending on the cell chemistry considered and the application-specific operating conditions. For example, in applications with high current rates and variable ambient temperature an extension with a lithium plating model is recommended. For the targeted parameterization of the extended model, ICA can also be used to differentiate between LLI, LAM_{PE} and LAM_{NE}. Fur-

thermore, the evaluation of electrochemical impedance spectroscopy or relaxation measurements can be used to support the separation of further aging mechanisms.

Author Contributions

Amelie Krupp: Main author of manuscript. Conceptualization, Methodology, Software, Validation, Formal analysis, Investigation, Data Curation, Visualization, Writing - Original Draft, Writing - Review and Editing, *Robert Beckmann*: Conceptualization, Methodology, Software, Formal analysis, Supervision, Writing - Original Draft, Writing - Review and Editing, *Theys Diekmann*: Investigation, Resources, Writing - Review and Editing, Funding acquisition, *Gerd Liebig*: Methodology, Investigation, Supervision, Writing - Review and Editing, *Ernst Ferg*: Conceptualization, Methodology, Supervision, Writing - Review and Editing, *Frank Schuldt*: Conceptualization, Resources, Supervision, Writing - Review and Editing, Funding acquisition, *Carsten Agert*: Conceptualization, Resources, Supervision, Writing - Review and Editing

Acknowledgments

The results were generated in the framework of the project HyReK 2.0 (grant no. 03ET6147C). We thank the German Federal Ministry for Economic Affairs and Climate Action (BMWK) for funding.

References

[1] Amelie Krupp et al. “Semi-empirical cyclic aging model for stationary storages based on graphite anode aging mechanisms”. In: *Journal of Power Sources* 561 (2023), p. 232721. ISSN: 03787753. DOI: 10.1016/j.jpowsour.2023.232721.

[2] Xing Jin et al. “Applicability of available Li-ion battery degradation models for system and control algorithm design”. In: *Control Engineering Practice* 71 (2018), pp. 1–9. ISSN: 09670661. DOI: 10.1016/j.conengprac.2017.10.002.

[3] Bolun Xu et al. “Modeling of Lithium-Ion Battery Degradation for Cell Life Assessment”. In: *IEEE Transactions on Smart Grid* 9.2 (2018), pp. 1131–1140. ISSN: 1949-3053. DOI: 10.1109/TSG.2016.2578950.

[4] Tanja Gewald et al. “Accelerated Aging Characterization of Lithium-ion Cells: Using Sensitivity Analysis to Identify the Stress Factors Relevant to Cyclic Aging”. In: *Batteries* 6.1 (2020), p. 6. DOI: 10.3390/batteries6010006.

[5] Issam Baghdadi et al. “Lithium battery aging model based on Dakin’s degradation approach”. In: *Journal of Power Sources* 325 (2016), pp. 273–285. ISSN: 03787753. DOI: 10.1016/j.jpowsour.2016.06.036.

[6] Yingzhi Cui et al. “Multi-stress factor model for cycle lifetime prediction of lithium ion batteries with shallow-depth discharge”. In: *Journal of Power Sources* 279 (2015), pp. 123–132. ISSN: 03787753. DOI: 10.1016/j.jpowsour.2015.01.003.

[7] Joris de Hoog et al. “Combined cycling and calendar capacity fade modeling of a Nickel-Manganese-Cobalt Oxide Cell with real-life profile validation”. In: *Applied Energy* 200 (2017), pp. 47–61. ISSN: 03062619. DOI: 10.1016/j.apenergy.2017.05.018.

[8] Md Sazzad Hosen et al. “Electro-aging model development of nickel-manganese-cobalt lithium-ion technology validated with light and heavy-duty real-life profiles”. In: *Journal of Energy Storage* 28 (2020), p. 101265. ISSN: 2352152X. DOI: 10.1016/j.est.2020.101265.

[9] Martin Petit, Eric Prada, and Valérie Sauvant-Moynot. “Development of an empirical aging model for Li-ion batteries and application to assess the impact of Vehicle-to-Grid strategies on battery lifetime”. In: *Applied Energy* 172 (2016), pp. 398–407. ISSN: 03062619. DOI: 10.1016/j.apenergy.2016.03.119.

[10] M. Schimpe et al. “Comprehensive Modeling of Temperature-Dependent Degradation Mechanisms in Lithium Iron Phosphate Batteries”. In: *Journal of The Electrochemical Society* 165.2 (2018), A181–A193. ISSN: 0378-7753. DOI: 10.1149/2.1181714jes.

[11] Johannes Schmalstieg et al. “A holistic aging model for Li(NiMnCo)O2 based 18650 lithium-ion batteries”. In: *Journal of Power Sources* 257 (2014), pp. 325–334. ISSN: 03787753. DOI: 10.1016/j.jpowsour.2014.02.012.

[12] John Wang et al. “Degradation of lithium ion batteries employing graphite negatives and nickel–cobalt–manganese oxide + spinel manganese oxide positives: Part 1, aging mechanisms and life estimation”. In: *Journal of Power Sources* 269 (2014), pp. 937–948. ISSN: 03787753. DOI: 10.1016/j.jpowsour.2014.07.030.

[13] Andrea Marongiu, Marco Roscher, and Dirk Uwe Sauer. “Influence of the vehicle-to-grid strategy on the aging behavior of lithium battery electric vehicles”. In: *Applied Energy* 137 (2015), pp. 899–912. ISSN: 03062619. DOI: 10.1016/j.apenergy.2014.06.063.

[14] Kandler Smith et al. “Comparison of Plug-In Hybrid Electric Vehicle Battery Life Across Geographies and Drive Cycles”. In: *SAE Technical Paper Series*. SAE Technical Paper Series. SAE International400 Commonwealth Drive, Warrendale, PA, United States, 2012. DOI: 10.4271/2012-01-0666.

[15] Alan Millner. “Modeling Lithium Ion battery degradation in electric vehicles”. In: *2010 IEEE Conference on Innovative Technologies for an Efficient and Reliable Electricity Supply*. IEEE, 27.09.2010 - 29.09.2010, pp. 349–356. ISBN: 978-1-4244-6076-2. DOI: 10.1109/CITRES.2010.5619782.

[16] Matthieu Dubarry, Cyril Truchot, and Bor Yann Liaw. “Cell degradation in commercial LiFePO4 cells with high-power and high-energy designs”. In: *Journal of Power Sources* 258 (2014), pp. 408–419. ISSN: 03787753. DOI: 10.1016/j.jpowsour.2014.02.052.

[17] Shriram Santhanagopalan et al. “Parameter Estimation and Life Modeling of Lithium-Ion Cells”. In: *Journal of The Electrochemical Society* 155.4 (2008), A345. ISSN: 0378-7753. DOI: 10.1149/1.2839630.

[18] G. Sikha et al. “Comparison of the capacity fade of Sony US 18650 cells charged with different protocols”. In: *Electrochemical and Solid-State Letters* 122.1 (2003), pp. 67–76. ISSN: 0378-7753. DOI: 10.1016/S0378-7753(03)00027-2.

[19] Amelie Krupp et al. “Calendar aging model for lithium-ion batteries considering the influence of cell characterization”. In: *Journal of Energy Storage* 45 (2022), p. 103506. ISSN: 2352152X. DOI: 10.1016/j.est.2021.103506.

[20] Justin Purewal et al. “Degradation of lithium ion batteries employing graphite negatives and nickel–cobalt–manganese oxide + spinel manganese oxide positives: Part 2, chemical–mechanical degradation model”. In: *Journal of Power Sources* 272 (2014), pp. 1154–1161. ISSN: 03787753. DOI: 10.1016/j.jpowsour.2014.07.028.

[21] Izaro Laresgoiti et al. “Modeling mechanical degradation in lithium ion batteries during cycling: Solid electrolyte interphase fracture”. In: *Journal of Power Sources* 300 (2015), pp. 112–122. ISSN: 03787753. DOI: 10.1016/j.jpowsour.2015.09.033.

[22] Lars von Kolzenberg, Arnulf Latz, and Birger Horstmann. “Solid-Electrolyte Interphase During Battery Cycling: Theory of Growth Regimes”. In: *cssc* (2020). DOI: 10.1002/cssc.202000867.

[23] Björn Rumberg et al. “Holistic calendar aging model parametrization concept for lifetime prediction of graphite/NMC lithium-ion cells”. In: *Journal of Energy Storage* 30 (2020), p. 101510. ISSN: 2352152X. DOI: 10.1016/j.est.2020.101510.

[24] Jorn M. Reniers, Grietus Mulder, and David A. Howey. “Review and Performance Comparison of Mechanical-Chemical Degradation Models for Lithium-Ion Batteries”. In: *Journal of The Electrochemical Society* 166.14 (2019), A3189–A3200. ISSN: 0378-7753. DOI: 10.1149/2.0281914jes.

[25] Peter M. Attia et al. “Electrochemical Kinetics of SEI Growth on Carbon Black: Part I. Experiments”. In: *Journal of The Electrochemical Society* 166.4 (2019), E97–E106. ISSN: 0378-7753. DOI: 10.1149/2.0231904jes.

[26] Lars von Kolzenberg et al. “A four parameter model for the solid-electrolyte interphase to predict battery aging during operation”. In: *Electrochemical and Solid-State Letters* 539 (2022), p. 231560. ISSN: 0378-7753. DOI: 10.1016/j.jpowsour.2022.231560.

[27] Dongjiang Li et al. “Degradation Mechanisms of C6/LiFePO4 Batteries: Experimental Analyses of Cycling-induced Aging”. In: *Electrochimica Acta* 210 (2016), pp. 445–455. ISSN: 00134686. DOI: 10.1016/j.electacta.2016.05.091.

[28] Matthew B. Pinson and Martin Z. Bazant. *Theory of SEI Formation in Rechargeable Batteries: Capacity Fade, Accelerated Aging and Lifetime Prediction*. URL: http://arxiv.org/pdf/1210.3672v3.

[29] Severin Lukas Hahn et al. “Quantitative validation of calendar aging models for lithium-ion batteries”. In: *Journal of Power Sources* 400 (2018), pp. 402–414. ISSN: 03787753. DOI: 10.1016/j.jpowsour.2018.08.019.

[30] Jonas Keil and Andreas Jossen. “Electrochemical Modeling of Linear and Nonlinear Aging of Lithium-Ion Cells”. In: *Journal of The Electrochemical Society* 167.11 (2020), p. 110535. ISSN: 0378-7753. DOI: 10.1149/1945-7111/aba44f.

[31] Simon Schweidler et al. “Volume Changes of Graphite Anodes Revisited: A Combined Operando X-ray Diffraction and In Situ Pressure Analysis Study”. In: *The Journal of Physical Chemistry C* 122.16 (2018), pp. 8829–8835. ISSN: 1932-7447. DOI: 10.1021/acs.jpcc.8b01873.

[32] Peter Keil and Andreas Jossen. “Calendar Aging of NCA Lithium-Ion Batteries Investigated by Differential Voltage Analysis and Coulomb Tracking”. In: *Journal of The Electrochemical Society* 164.1 (2017), A6066–A6074. ISSN: 0378-7753. DOI: 10.1149/2.0091701jes.

[33] Anna Tomaszewska et al. “Lithium-ion battery fast charging: A review”. In: *eTransportation* 1 (2019), p. 100011. ISSN: 25901168. DOI: 10.1016/j.etran.2019.100011.

[34] Meinert Lewerenz et al. “Systematic aging of commercial LiFePO 4 |Graphite cylindrical cells including a theory explaining rise of capacity during aging”. In: *Journal of Power Sources* 345 (2017), pp. 254–263. ISSN: 03787753. DOI: 10.1016/j.jpowsour.2017.01.133.

[35] Balazs Gyenes et al. “Understanding Anomalous Behavior in Coulombic Efficiency Measurements on Li-Ion Batteries”. In: *Journal of The Electrochemical Society* 162.3 (2015), A278–A283. ISSN: 0378-7753. DOI: 10.1149/2.0191503jes.

[36] Meinert Lewerenz et al. “Irreversible calendar aging and quantification of the reversible capacity loss caused by anode overhang”. In: *Journal of Energy Storage* 18 (2018), pp. 149–159. ISSN: 2352152X. DOI: 10.1016/j.est.2018.04.029.

[37] Johannes Philipp Fath et al. “The influence of the anode overhang effect on the capacity of lithium-ion cells – a 0D-modeling approach”. In: *Journal of Energy Storage* 29 (2020), p. 101344. ISSN: 2352152X. DOI: 10.1016/j.est.2020.101344.

[38] Amelie Krupp et al. “Incremental Capacity Analysis as a State of Health Estimation Method for Lithium-Ion Battery Modules with Series-Connected Cells”. In: *Batteries* 7.1 (2021), p. 2. DOI: 10.3390/batteries7010002.

[39] Christoph R. Birkl et al. “Degradation diagnostics for lithium ion cells”. In: *Journal of Power Sources* 341 (2017), pp. 373–386. ISSN: 03787753. DOI: 10.1016/j.jpowsour.2016.12.011.

[40] Uli Schlachter et al. “Optimised capacity and operating strategy for providing frequency containment reserve with batteries and power-to-heat”. In: *Journal of Energy Storage* 32 (2020), p. 101964. ISSN: 2352152X. DOI: 10.1016/j.est.2020.101964.

[41] Eduardo M. Perassi and Ezequiel P.M. Leiva. “Capacity fading model for a solid electrolyte interface with surface growth”. In: *Electrochimica Acta* 308 (2019), pp. 418–425. ISSN: 00134686. DOI: 10.1016/j.electacta.2019.03.202.

[42] Christian Kupper et al. “End-of-Life Prediction of a Lithium-Ion Battery Cell Based on Mechanistic Aging Models of the Graphite Electrode”. In: *Journal of The Electrochemical Society* 165.14 (2018), A3468–A3480. ISSN: 0378-7753. DOI: 10.1149/2.0941814jes.

[43] Johannes Fleer et al. “Techno-economic evaluation of battery energy storage systems on the primary control reserve market under consideration of price trends and bidding strategies”. In: *Journal of Energy Storage* 17 (2018), pp. 345–356. ISSN: 2352152X. DOI: 10.1016/j.est.2018.03.008.

[44] Daniel-Ioan Stroe et al. “Degradation behaviour of Lithium-ion batteries based on field measured frequency regulation mission profile”. In: *2015 IEEE Energy Conversion Congress and Exposition (ECCE)*. IEEE, 20.09.2015 - 24.09.2015, pp. 14–21. ISBN: 978-1-4673-7151-3. DOI: 10.1109/ECCE.2015.7309663.

5

Operating strategy optimization for a sector coupling system providing frequency containment reserve

This chapter bases on the publication „Operating strategy optimization considering battery aging for a sector coupling system providing frequency containment reserve“ by Amelie Krupp, Robert Beckmann, Patrick Draheim, Eva Meschede, Ernst Ferg, Frank Schuldt, and Carsten Agert.

Abstract

Battery storage systems are increasingly used in the frequency containment reserve (FCR) application. Coupling the battery with a power-to-heat module can further increase the system's profitability. Different studies optimized the hybrid system's operation by considering country-specific regulations. However, lithium-ion battery aging has not yet been included. This work analyses the impact of system dimension and operation on net present value, considering battery aging. The operation strategy consists of adjusting the target SoE and using the deadband degree of freedom, which allows to suspend provision of FCR for minor frequency deviations. Battery lifetime is simulated using a semi-empirical aging model describing graphite anode aging mechanisms. The highest NPV is obtained with a battery dimension of 0.5 Wh/W, 90% target SoE, and normal deadband utilization. For the considered NMC battery cells, deadband utilization contributes to battery lifetime extension when operating at high SoE. Without this cell chemistry-specific lifetime gain, a lower target SoE of 60% and a larger system size of 0.6 is economically more advantageous. In a sensitivity analysis, battery aging was detected as the most crucial parameter influencing system profitability at high FCR prices. The results highlight the importance of including reliable battery aging simulations in future FCR operation optimizations.

5.1 Introduction

The European Union aims to reduce greenhouse gas emissions and reach climate neutrality by 2050 [1]. A massive expansion of the share of renewable energy sources (RES) is necessary to achieve this goal. In the long term, the fluctuating feed-in from RES can lead to increasing frequency fluctuations in the European interconnected grid [2]. This increases the demand for ancillary services to stabilize the grid frequency. Frequency containment reserve (FCR), also called primary frequency control, is the fastest of the frequency regulation mechanisms in Europe. Various technologies, such as pumped hydro storage, power-to-X solutions, and battery storages, are used to provide FCR. Battery energy storage systems (BESS) are well suited due to their high efficiency and fast response time. A decrease in acquisition costs leads to more lithium-ion batteries used in ancillary services such as FCR provision [3]. With more FCR providers, competition increases, causing a decrease in FCR prices [4]. Under these conditions, optimizing the BESS lifetime profitability is essential for battery operators.

Many economic analyses of stand-alone battery storage systems in FCR application have already been carried out in literature. Thereby, a consideration of the respective market conditions defined by the transmission grid operators (TSO) is relevant. Thien et al. [5] evaluated the impact of different operating parameters on FCR provision considering the market specifications of the German TSO. Fleer et al. [4] modeled the revenues under different operating strategies, evaluating the sensitivity of the results to the evolution of the FCR and battery price. Other studies focused on possible operating strategies in the Danish FCR market [6–8].

Beyond optimizing the FCR operation strategy and the sizing of the battery storage unit, there are fundamentally two approaches to increase system profitability. First, in addition to FCR operation, other services, such as arbitrage trading, can be provided. Second, the battery storage can be operated in a hybrid system. This includes, for example, coupling with sector-integrating technologies such as a power-to-heat (PtH) module. The PtH module can provide negative FCR, which means taking energy from the grid. This allows the coupled battery storage to operate at a high state of charge (SoC). Therefore, the hybrid system allows innovative operating strategies and smaller battery storage sizing. It is an efficient way to increase system profitability compared to stand-alone battery storages [9–11]. Draheim et al. [12] conducted an economic analysis of this type of hybrid system under the German FCR market conditions in 2019. In particular, the taxes, levies, and charges (TLC) for the PtH module operation were identified as a critical influence on the economic

viability. Schlachter et al. [13] analyzed the hybrid system's net present value (NPV) dependence on battery dimension and SoC setpoint. Operating a small BESS at high SoC was economically feasible because of smaller initial investment and maintenance costs. However, many lithium-ion battery cell chemistries exhibit accelerated aging and, thus, reduced lifetime operating at high SoC, which was not considered in the mentioned study.

Over time, batteries suffer from capacity loss and resistance increase due to calendar and cyclic aging. Hence, when they no longer meet their application requirements, they must be replaced. This is associated with additional investment costs. It is therefore important to have a good understanding of the expected lifetime of a BESS in an application, both in terms of reducing its long-term environmental impact and ensuring economic profitability. The predicted battery lifetime in FCR application depends on cell chemistry, system dimensioning, and operation strategy. Battery aging has already been included in various economic analyses, considering the Danish [6, 7] and German [4, 10] market regulations. The studies predicted lifetimes in the range of seven to 26 years. This vast spread again demonstrates the importance of a lifetime-optimized operating strategy. In their economic analysis, Mündelein et al. [10] considered both, battery aging and the case of coupling BESS and PtH module for FCR provision. The battery storage consisted of a combination of lead–acid and lithium-ion batteries. However, the lithium-ion battery was eliminated due to its higher acquisition costs when the battery system was coupled with a PtH module. The optimization, therefore, only considered a lead–acid battery coupled with a PtH module.

In this paper, the hybrid system consisting of a lithium-ion battery storage combined with a PtH module is economically optimized for its operating strategy and battery dimension. The battery dimension is defined by the BESS energy to prequalified FCR power ratio. An intensive investigation of lithium-ion battery aging is included using the semi-empirical battery aging model introduced by Krupp et al. [14, 15]. It differs from previous studies by considering all battery stress factors in purely physically based model equations. Furthermore, the model was explicitly validated on an FCR load profile. For reliable lifetime prediction, the model is extended by a method for calculating the anode SoC during battery aging. The operational strategies comprise adjusting the battery state of energy (SoE) setpoint and using FCR degrees of freedom (DoF). The economic analysis is based on the approach of Draheim et al. [12] and is updated to the latest regulations and prices applicable to the German FCR market. The technical data of the analysis refer to the HyReK 2.0 project, in which the coupling of a 14 MWh battery storage and a PtH module providing FCR is investigated [16].

The paper is structured as follows: 5.2, describes the currently applicable regulations in the German FCR market. 5.3 outlines the battery aging model. Furthermore, the challenges of lifetime modeling based on time-limited battery test series are discussed. They are accounted for by a new method of using the anode SoC instead of the battery SoC in aging modeling. 5.4 describes the overall methodology with load profile calculation, aging modeling, and net present value analysis. Finally, 5.5 discusses the lifetime and NPV results for various operating strategies and battery dimensions.

5.2 German FCR market

The following summarizes the German FCR market framework and price development, FCR regulations and DoF, and applicable taxes, levies, and charges. In recent years, some adjustments to the FCR regulations have been made, which allow further flexibility in the market. The overview focuses on addressing recent regulatory changes.

5.2.1 Market framework and FCR prices

To promote fair competition and transparency, the TSO of Austria, Belgium, the Netherlands, France, Germany, Switzerland, Western Denmark, and Slovenia trade their primary control reserve on a common market. The time periods in which FCR is provided were shortened to four-hour slices in 2020. A minimum power of 1MW must be bid. In 2019, a uniform pricing system was established. Since then, all accepted tenders in the merit-order list have been remunerated with the highest accepted price [17]. The mean FCR- and electricity prices from 2014 to today are summarized in Figure 5.1. The FCR price has been subject to strong fluctuations in recent years. Until 2020, prices dropped by about 70%. This can be attributed to increased competition in the market [3]. Afterwards, the FCR price strongly increased. It follows the development of the energy markets, which are subject to a substantial price increase. The shown increase in electricity prices depends on various factors, such as fuel costs or different power plant operating costs, which are, in turn, influenced by political measures such as regulations, subsidy programs, or geopolitical developments [18–20]. How prices will develop in the future remains unclear [21].

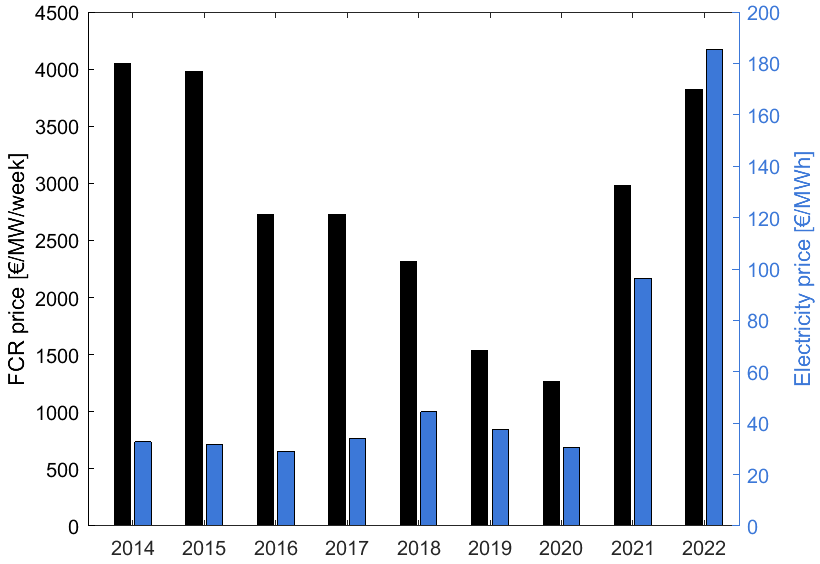

Figure 5.1: Development of the average German primary FCR and daily Power Future electricity price between 2014 and 2022 based on data from Regelleistung.net [22] and the European Energy Exchange AG [23].

5.2.2 Rules and DoF

Despite efforts by the European Network of Transmission System Operators for Electricity (ENTSO-E) for standardization, the control reserve requirements may differ across Europe. The FCR rules and degrees of freedom set by the German TSO are described in more detail below. They include the overfulfillment and deadband DoF and the 15-minutes criterion with related operating point adjustments. The reserve mode, newly introduced in June 2022, in which the system's response to frequency fluctuations changes when reaching the limits of its stored energy in the event of a grid alarm state, is not included in the model presented in this paper. For a more detailed description, the reader is referred to the latest version of the German TSO FCR prequalification conditions [24].

Systems that provide FCR respond to frequency fluctuations in the grid. The nominal grid frequency in the European interconnected grid is 50 Hz. When there is an imbalance between generation and consumption, grid frequency fluctuations occur. To minimize these, FCR providers supply power when the grid frequency decreases below 50 Hz (positive FCR) and take power from the grid when the frequency increases above 50 Hz (negative FCR). FCR power is proportional to the grid frequency fluctuation until the maximum prequalified power is supplied at a frequency deviation of 200 mHz. The FCR power is thus given by

$$P_{FCR}(\Delta f) = \begin{cases} 1 & \text{if } \Delta f \geq 200\,\text{mHz} \\ \Delta f / 200\,\text{mHz} & \text{if } |\Delta f| < 200\,\text{mHz} \\ -1 & \text{if } \Delta f \leq 200\,\text{mHz} \end{cases} \tag{5.1}$$

with the frequency deviation Δf. In Figure 5.2a the required FCR power is plotted over the frequency deviation. Within certain limits, it is allowed to deviate from this function. These limits are defined in the degrees of freedom.

Degrees of freedom

The German TSO allow FCR providers certain degrees of freedom that can be used to support the battery operating strategy. In this study, the overfullfillment and deadband DoF are considered. Overfulfillment means that at any time, 20% more FCR power than required can be provided. The frequency range up to a maximum frequency deviation of 10 mHz is called deadband. Within the deadband, no FCR power needs to be provided. The DoF ranges are marked in Figure 5.2a.

15-minutes criterion

The battery storage must be able to provide the maximum FCR power for at least 15 minutes at any time during regular operation. This is specified in the so-called 15-minutes criterion. Previously, the 30-minutes criterion was applied, but it was stopped in 2019 following a decision by the German Federal Network Agency [21]. With the adjustment, battery storages providing FCR can be dimensioned smaller. This positively impacts their profitability since battery investment costs can be reduced [5, 12, 13].

The 15-minutes criterion limits the usable energy range of the BESS. A storage with 1 MWh energy and 1 MW prequalified power needs an energy buffer of 250 kWh in charge and discharge direction. In the case of combining BESS and PtH module, the energy is only limited at low SoE, as it is possible to switch to the PtH module at high SoE. Energy ranges of a stand-alone battery storage and battery storage combined with a PtH module are shown in Figure 5.2b plotted over the battery dimension, which is defined by the BESS energy to maximum FCR power ratio.

Operating point adjustment

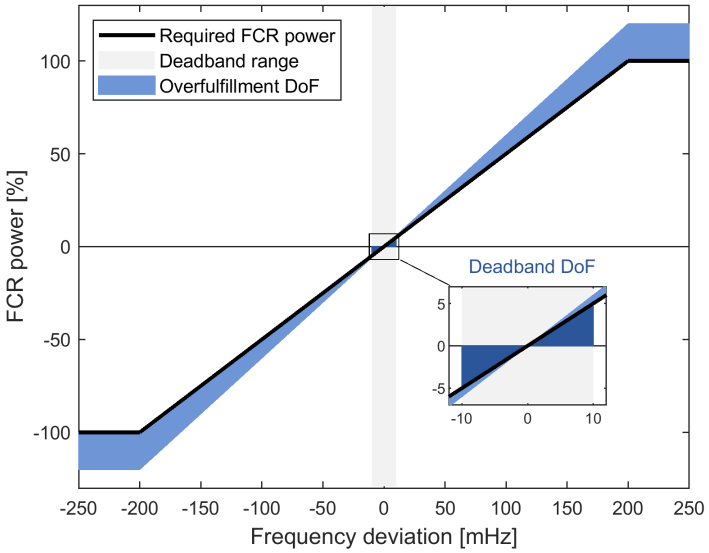

(a)

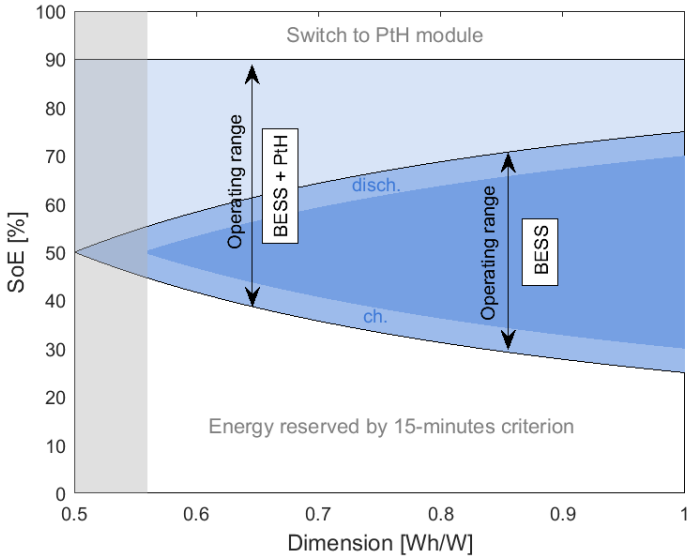

(b)

Figure 5.2: (a) FCR power provided as a function of frequency deviation from 50 Hz. The power ranges of the deadband utilization and overfulfillment DoF are marked. (b) Allowed energy range at different system dimensions for a stand-alone BESS and a BESS coupled with a PtH module, considering the 15-minutes criterion and the market lag for charging and discharging. The PtH switching was set to 90% SoE.

If there is a risk that the energy range defined by the 15-minutes criterion will be violated, the battery storage must be additionally charged or discharged. In the following, this process is referred to as operating point adjustment (OPA). Several options are available for performing an OPA. Either other technical units of the same balancing group are used, or power is bought and sold by trading on the electricity market. The shortest possible delivery interval on the continuous intraday market is 15 minutes. Power delivery starts at each 15-minute interval, resulting in a maximum delivery delay of 15 minutes. Trading can be done up to 5 minutes before delivery starts. This gate closure time introduces a further delay. In total, this results in a maximum waiting time between service triggering and power delivery of t_{lag} = 20 minutes. To guarantee compliance with the 15-minutes criterion despite the lead times, an additional energy buffer of

$$E_{lag} = 0.25 \cdot P_{pq} \cdot t_{lag} \tag{5.2}$$

with the prequalified power P_{pq} must be reserved. Thereby it is allowed to assume a frequency deviation of 50 mHz for the lag time, which results in the prefactor 0.25 considering Eq. (5.1) [24].

5.2.3 TLC for battery storages and PtH modules

Taxes, levies, and charges are significant contributors to the profitability of FCR systems. Worschech et al. [25] presented a compilation of TLC in Germany for PtH modules and BESS. The TLC charged per consumed energy are especially relevant for optimizing operation strategies. They include the electricity tax, a part of the grid fees, the concession levy, and further charges. Another part of the grid fees is levied per capacity connected to the grid and per year. The values of the TLC from 2022 are summarized in Table 5.1. The value-added tax (VAT) of 19% is levied on all TLC. Annual costs such as metering fees are not considered because they are not affected by the operating strategy. In contrast to nationwide taxes and charges, grid fees are set by the transmission system operator responsible for the system locality. We refer to the location Bremen in Germany.

With 77.55 €/MWh, the PtH module is charged with over ten times the amount of TLC than the battery storage. Until recently, PtH modules were additionally burdened with the RE charge. This has been abolished by 01 July 2022. The significantly lower cost of using the BESS is due to its exclusion from electricity tax, grid fees, and CHP charge to avoid double burden for storage and release of energy.

Name	Unit	BESS	PtH	Note/Source
Electricity tax	€/MW h	0	20.5	[26]
Grid fees	€/MW h	0	48.7	Annual utilization <2500h, Medium voltage grid [27]
RE charge	€/MW h	0	0	Abolished in 2022 [28]
§ 19 charge	€/MW h	4.37	4.37	[29]
AbLaV-charge	€/MW h	0.03	0.03	[30]
Offshore grid charge	€/MW h	0	4.19	Omission for BESS after §17f EnWG, §27b KWGK and § 61l EEG [31]
Concession levy	€/MW h	1.1	1.1	Special contract customer [32]
CHP charge	€/MW h	0	3.78	[33]
VAT	€/MW h	1.84	12.87	
Sum	**€**/MW h	**6.54**	**77.55**	
Grid fees	€/kW/year	0	9.2	Medium voltage grid [27]
VAT	€/kW/year	0	1.75	
Sum	**€**/kW/year	**0**	**10.95**	

Table 5.1: German TLC for battery storages and PtH modules in 2022.

The PtH module is classified as an end consumer. Therefore, this regulation does not apply to it, resulting in significantly increased TLC [25].

5.3 Battery aging model

Consideration of battery aging is critical for optimizing the profitability of BESS in FCR application. The aging model to simulate the battery capacity loss was introduced by Krupp et al. [14, 15]. The semi-empirical model equations describe important anode aging mechanisms. In calendar aging, SoC and temperature-dependent solid electrolyte interface (SEI) growth is modeled. In cyclic aging, SEI cracking and reforming and anode active material cracking are addressed. They depend on the depth of discharge (DoD), average SoC (∅SoC), temperature, and current rate during cycling. According to the cause-effect principle, aging mechanisms lead to different aging modes that contribute to capacity loss: loss of lithium inventory (LLI) and loss of active material at the negative and positive electrode (LAM_{NE} and LAM_{PE}) [34]. The overall model adds up the separately modeled calendar and cyclic capacity loss following the superposition approach. A schematic overview of the battery aging model with input parameters, described aging mechanisms, connected aging modes, and output is given in figure 5.3. The model was parametrized with

data from an extensive battery aging measurement campaign on 64Ah NMC battery cells from the HyReK 2.0 project [14, 15].

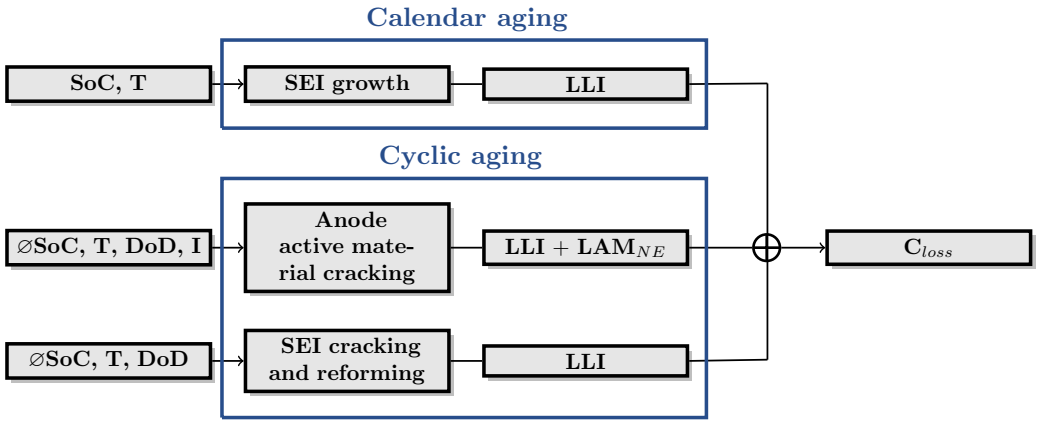

Figure 5.3: Battery aging model block diagram with input parameters, aging mechanism, connected aging modes and model output.

5.3.1 SoC adjustment

For all considered anode aging mechanisms, the anode SoC is decisive for capacity loss during cyclization [15]. While the battery SoC is determined by the ratio of battery charge to battery capacity, the anode SoC refers to the ratio of battery charge to anode capacity. The anode and battery cell SoC differ for two reasons. First, the anode overhang offsets the anode SoC at the beginning of battery life. Second, the anode and battery SoC change differently as the battery ages. The initial anode SoC offset is automatically considered in (semi-)empirical models parametrized with capacity loss data. The shift of the SoC to each other can be assumed to be negligible for small capacity losses, e.g., in model parameterization. However, differentiation between anode and battery SoC significantly impacts the simulation results when modeling the battery lifetime. The following explains the difference between battery and anode SoC and their dependence on the share of the considered aging modes LLI and $\mathrm{LAM_{NE}}$.

The battery SoC is determined by the ratio of the battery charge Q to the actual cell capacity C_{act}

$$SoC_{Bat} = \frac{Q}{C_{act}} \cdot 100\% = \frac{Q}{\frac{C_{ini}}{100\%}\left(100\% - \max\left(C_{loss,\mathrm{LAM_{NE}}}, C_{loss,LLI}\right)\right)} \cdot 100\% \quad (5.3)$$

The current cell capacity results from the initial capacity C_{ini} minus the maximum percentage capacity loss due to LLI or LAM_{NE} from cyclic and calendar aging. Loss of active material predominates either at the anode or the cathode. Since this model is specified to anode aging mechanisms, it is assumed that the loss of anode material in the batteries under consideration will predominate in the long term. If LAM_{NE} determines the capacity loss, the battery charging process is terminated by the potential decrease of the fully lithiated anode. Correspondingly, more lithium remains in the cathode at the end of charge and the cell capacity decreases [34, 35]. If the capacity loss due to LLI predominates, only a part of the available electrode capacity is used. The charge and discharge are terminated by the rising electrode potential of the lithium-delivering electrode.

The anode SoC is related to the current anode capacity C_{An}. It is influenced exclusively by capacity loss due to LAM_{NE}:

$$SoC_{An} = \frac{Q}{C_{An}} \cdot 100\% = \frac{Q}{\frac{C_{ini}}{100\%}\left(100\% - C_{loss,\text{LAM}_{\text{NE}}} + C_{Ov}\right)} \cdot 100\%. \tag{5.4}$$

Thereby, the initial capacity of the anode is the sum of the initial cell capacity and the percentage capacity of the anode overhang C_{Ov}.

With increasing capacity loss, a shift of the anode SoC to the battery SoC occurs. Combining equation (5.3) and (5.4), the anode SoC can be calculated over

$$SoC_{An} = SoC_{Bat} \cdot \frac{100\% - \max\left(C_{loss,\text{LAM}_{\text{NE}}}, C_{loss,LLI}\right)}{100\% - C_{loss,\text{LAM}_{\text{NE}}} + C_{Ov}}. \tag{5.5}$$

It must be noted that the used $C_{loss,\text{LAM}_{\text{NE}}}$ describes the actual capacity loss of the anode active material, even if this is not detectable in the battery capacity because of predominating LLI. At moderate battery loads in FCR provision, LLI is expected to dominate capacity loss over the battery lifetime [15, 36, 37]. Assuming negligible $C_{loss,\text{LAM}_{\text{NE}}}$ results in the special case of

$$SoC_{An} = SoC_{Bat} \cdot \frac{100\% - C_{loss,LLI}}{100\% + C_{Ov}}. \tag{5.6}$$

5.4 Methodology

The analysis of system rentability at different operating strategies and system dimensions is divided into three main steps. First, the BESS power profiles are simulated for each operating case using real grid frequency data. The model inputs are the battery target SoE, the system dimension, and the deadband DoF utilization strategy. The resulting power and SoE profiles are converted into SoC profiles using a voltage-SoC lookup table. In the second step, battery lifetime is determined in the aging modeling. For this purpose, load cycles in the SoC profiles are evaluated with rainflow counting. Finally, economic comparison of the considered operating strategy profitability is performed using NPV analysis. The FCR system design is based on the "HyReK 2.0" project [16]. The modeling is done with Matlab. Figure 5.4 shows an overview of the methodology. The analysis steps are described in more detail below.

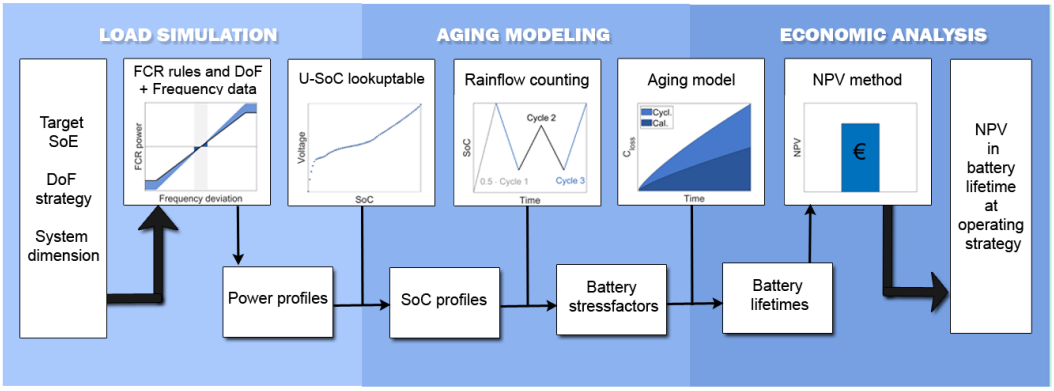

Figure 5.4: Flow chart methodology.

5.4.1 Power- and SoC profiles

The FCR power profiles are calculated over real, second-resolution frequency data from January 01, 2019, to December 09, 2019. The power profiles are determined considering the German rules for FCR provision and the DoF overfulfillment and deadband utilization. Both DoF are used to keep the battery SoE as close as possible to the start and target SoE. Deadband utilization was modeled in two different operating strategies. In normal deadband utilization (NormDb), no primary control power is provided in the deadband unless it serves to achieve the target SoE. In the second strategy, SoE10Db, all deadband power is exposed in a range of 10% SoE around the target SoE to reduce the battery operating time. Beyond that, normal

deadband usage applies. The lower battery energy limit is determined by the 15-minutes criterium and the market lag. When reached, the storage is recharged for 15 minutes with 25% of the prequalified FCR power. At 90% SoE, the energy infeed switches to the PtH module. For the battery aging modeling, the single-cell battery power is relevant. It is calculated from the total FCR power supplied, considering the interconnection in the 14MWh HyReK battery system. The prequalified FCR power and the maximum PtH module power are adapted to evaluate different battery system dimensions.

When analyzing whole systems, it is usually referred to the battery SoE. The energy change ΔE is calculated by multiplying power and time step size. In contrast, the aging modeling refers to the battery SoC. The related change of charge in ith time step $\Delta t_i = t_i \breve{} t_{i-1}$, with $i = 1, \ldots, N$ is determined over

$$\Delta Q(t_i) = P_{FCR}(t_i) \cdot \frac{\Delta t_i}{U(t_{i-1})}. \tag{5.7}$$

The battery voltage U for the previous SoC step is determined with a voltage-SoC lookup table. It was experimentally created based on a 1/10C discharge at $23°$C of one of the considered NMC cells. Since we only refer to the battery's discharge, the voltage hysteresis is not considered in the voltage-SoC assignment. In FCR provision, primarily very small power pulses and thus small battery currents occur. For this reason, it is assumed that the quasi-open-circuit voltage curve without an overvoltage model describes the actual battery voltage with sufficient accuracy. Additionally, the discharge data are used to determine the associated starting SoC for each starting SoE. The maximum deviation between SoC and SoE is 2.5% at 43.5% SoE for the considered cells. The change in battery SoC is calculated over

$$\Delta SoC(t_i) = \frac{\Delta Q(t_i)}{C_{act}} \cdot 100\% \tag{5.8}$$

with the actual battery capacity C_{act}. The initial capacity of the battery cells corresponds to the nominal capacity C_{nom}. The current profiles associated with each power profile are calculated by dividing battery cell power by voltage. The so-called C-rate relates the charge and discharge current to the nominal cell capacity.

5.4.2 Battery aging modeling

For lifetime estimation, the modeled one-year FCR load profile is repeated continuously until the battery storage reaches its end of life (EoL) at 20% capacity loss.

The EoL was defined in the HyReK 2.0 project. In principle, lower SoH are also possible for batteries in stationary applications. However, to model the capacity loss in the associated SoH range, possible additional long-term aging effects must be considered.
As the battery ages, its capacity decreases, resulting in larger DoD and a faster reaching of the upper and lower energy limits. For this reason, the power and SoC profiles are recalculated every 5% capacity loss. The anode SoC relevant for cyclic and calendar aging is determined using Eq. (5.6). The load cycles included in the SoC profile are evaluated with Rainflow Counting using the Matlab function *rainflow*. The rainflow counting algorithm identifies all cycles in variable load profiles and has already been used in various battery studies [5, 38]. The function outputs are the cycle count Cnt (full or half cycle) with DoD, average SoC, and cycle start and end time. In addition, the average current rate is determined from the current profile using the cycle start and end times. Due to predominating low current rates, the current error caused by overlapping of the identified cycles is neglected for FCR operation. Furthermore, the number of equivalent full cycles (EFC) is determined. One EFC describes the charge flowing in one complete capacity cycle of a new battery cell. The number of EFC for each counted cycle is calculated over

$$EFC = \frac{DoD[\%] \cdot C_{act} \cdot Cnt}{100\% \cdot C_{nom}}. \tag{5.9}$$

The battery aging model was introduced in section 5.3. A fixed temperature of 23 °C is assumed for the calendar and cyclic aging in the stationary temperature-controlled storage. The SoC evaluation for calendar aging is performed in 60s-time steps. Initial values for the numerical capacity loss calculation of the calendar aging $C_{loss,cal}$ and the cyclic loss of active material $C_{loss,LAM}$ are given in Table 5.2. They represent the initial presence of a SEI layer from formation and the first cracks in the active material of the anode, which grow during aging.

5.4.3 NPV analysis

The economic rentability is assessed by the widely used net present value method [4, 9, 12]. The NPV is calculated over

$$NPV = -C_o + \sum_{t=1}^{T} \frac{C_t}{(1+i)^t} \tag{5.10}$$

with the initial investment cost C_0 and the revenues and costs of the year C_t in the lifetime of the system T. The investment costs include fixed battery system investment costs C_B and the PtH module investment costs C_{PtH} per installed MW. The cash flow is discounted to the present. Discounting considers the time value of money, meaning that a specific money amount today is worth more than in the future. Revenues include FCR revenues R_{FCR} and heat revenues R_{PtH}. The costs considered are annual maintenance costs C_m, recharge costs C_r, and costs due to TLC C_{TLC}. The revenue from FCR is determined by the average of all time slice FCR prices in 2021. It is assumed that the system is surcharged for the provision of FCR in the entire year. The year 2021 was used to ensure the actuality of the results. Anyway, it is important to be aware that this may be an exceptional FCR price situation (see section 5.2.1). Table 5.2 summarizes all used model parameters. The costs due to TLC were shown in table 5.1.

Name	Variable	Value	Unit	Source
Energy battery system	$E_{nom,sys}$	14	MWh	[16]
Nominal cell capacity	C_{nom}	64	Ah	[16]
Initial calendar capacity loss	$C_{loss,cal}(1)$	$1 \cdot 10^{-4}$	%	
Initial capacity loss due to LAM$_{NE}$	$C_{loss,LAM}(1)$	$1 \cdot 10^{-6}$	%	
Anode overhang capacity	C_{Ov}	5	%	[14]
Discount rate	i	5	%	[9, 12]
Battery investment costs	C_B	10.5	million €	[16]
PtH investment costs	C_{PtH}	25,000	€/MWh	[13]
FCR revenues (2021)	R_{FCR}	153.972	€/a/MW	[22]
Heat revenues	R_{PtH}	10	€/MWh	[12]
Annual maintainance costs	C_m	110,000	€/a	[16]
Recharge costs (2021)	C_r	96.38	€/MWh	[23]

Table 5.2: Simulation parameters for the power and SoC profile calculation, the aging modeling, and the economic analysis.

5.5 Results and discussion

To analyze, how operating strategy and system dimension affect the system's profitability, this section discusses the results for the three methodology steps: load profile calculation, aging modeling, and NPV evaluation. The considered FCR operating strategies differ by target SoE and deadband utilization strategy. The two deadband strategies considered, NormDb and SoE10Db, were described in subsection 5.4.1.

5.5.1 Power profiles

The main characteristics of the modeled power profiles differ significantly. Figure 5.5a shows two example battery SoE time series for the operating cases 90% SoE with dimension 1 Wh/W and 60% SoE with dimension 0.5 Wh/W. The storage SoE moves within the lower limit defined by the 15-minutes criterion and the upper limit at 90% SoE from which power is fed into the PtH module. In case of a larger system dimension, the used energy range increases. The modeled SoE time series is strongly influenced by the target SoE. For 90% SoE, the PtH module is activated more frequently. The lower energy limit is reached less often than for 60 % target SoE which results in a lower number of OPAs. To allow comparison of all operating cases considered, figure 5.5b and 5.5c show important power profile properties plotted as a function of target SoE and system dimension for the case of not using the deadband DoF. They comprise the number of OPAs (Fig. 5.5b) and the percentage of the total operating time in which the battery rests (i.e., is not cycled) and the PtH module is used (Fig. 5.5c). The number of OPAs increases with decreasing target SoE and smaller system dimension. In both cases, the recharge limit set by the 15-minutes criterion is reached faster. Times of rest and PtH module usage increase with smaller system dimensions and higher target SoE due to faster reaching the limit where power is fed into the PtH module. Table 5.3 summarizes the qualitative correlations.

SoE	**Dimension**	**Small** ($\leq 0.6\mathrm{Wh/W}$)	**Big** ($\geq 0.9\mathrm{Wh/W}$)
Low ($\leq 60\%$)	Number of OPAs	◐ – ●	○
	Rest time	○ – ◐	○
	PtH time	○ – ◐	○
	Lifetime	○ – ◐	●
	NPV	●	○ – ◐
High ($\geq 80\%$)	Number of OPAs	○ – ◐	○
	Rest time	◐ – ●	○ – ◐
	PtH time	◐ – ●	○ – ◐
	Lifetime	○	◐ – ●
	NPV	●	○

Table 5.3: Qualitative load profile, lifetime and NPV results for different system dimensions and target SoE without deadband use. The results are classified in high ●, medium ◐ and low ○ which each corresponds to one third of the whole results range.

Using the different deadband strategies, the share of rest time in operation increases significantly. At big system dimensions, up to 20% more rest time for the NormDb strategy and 30% more rest time for the SoE10Db strategy are reached. The deadband DoF is used to maintain the target SoE better. Therefore, for medium

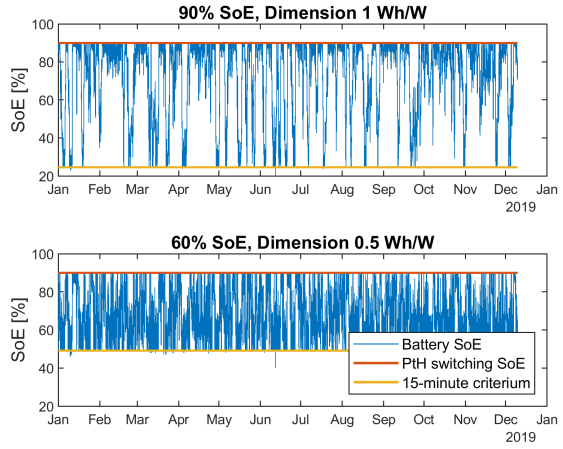

(a)

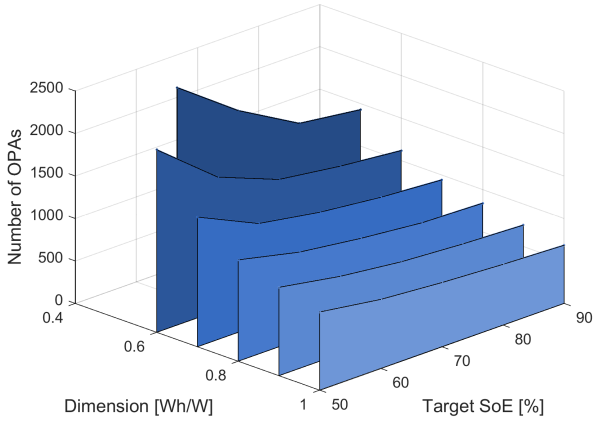

(b)

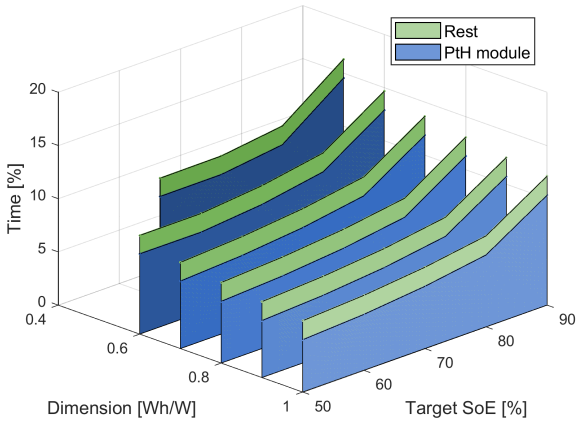

(c)

Figure 5.5: (a) Battery SoE over time for two example operating strategies. (b) Number of operating point adjustments (OPAs) and (c) percentage rest time and PtH module operation time on the first year of battery operation over the target SoE and system dimension without using the deadband DoF.

SoE, less OPAs and PtH module use is necessary with both deadband strategies. If the target SoE equals a switching SoE, the respective service is triggered more often. Comparing the two deadband strategies, the target SoE is better maintained with normal deadband use. For the example case with 90% SoE and dimensioning 0.5 Wh/W, the SoE is larger than 88% SoE in 33.4% of the time with the SoE10Db strategy. This value is increased to 39.3% with normal deadband usage NormDb.

5.5.2 Battery aging modeling

This subsection deals with the aging modeling results. First, the general model outcomes are discussed, including the SoC correction's influence on the capacity loss results. Afterwards, the lifetime results of different operating strategies are presented.

Aging modeling and SoC correction

In FCR operation, the battery storage is mainly subjected to very small DoD and low current rates. This is confirmed in the rainflow counting analysis. For a new battery storage, about 99% of the counted cycle ranges are below 10% DoD, and 77% are below 0.1% DoD. The average current rate is around 0.04C. Similar results have already been described in the literature [5, 39]. The mean SoC varies between the limits set by the 15-minutes criterion and the PtH switching. As the battery ages, the usable energy range of the storage decreases.

Figure 5.6 shows the modeled capacity loss plotted against time and the number of EFC for the example case of 90% target SoE and a system dimension of 0.5 Wh/W. Here, cyclic aging predominates capacity loss. The model results disagree with the widely used assumption that calendar aging determines the system lifetime in FCR application [5, 10]. The aging model was parameterized and validated on about one year of cyclic and calendar battery aging data. Furthermore, the results were plausible compared to literature results [39] and HyReK project field measurements [16] from four years of battery operation in FCR application [15]. Extrapolation to over 20 years of battery lifetime involves large uncertainties, such as differing single-cell behavior, system interconnection effects, and possibly changing dominant aging mechanisms. Cell chemistry-dependent long-term aging effects, such as increased cathode aging, are not considered in the model results and could increase the share of calendar aging. Furthermore, a shift in the ratio of the calendar to cyclic aging is possible due to different considerations of the anode overhang in

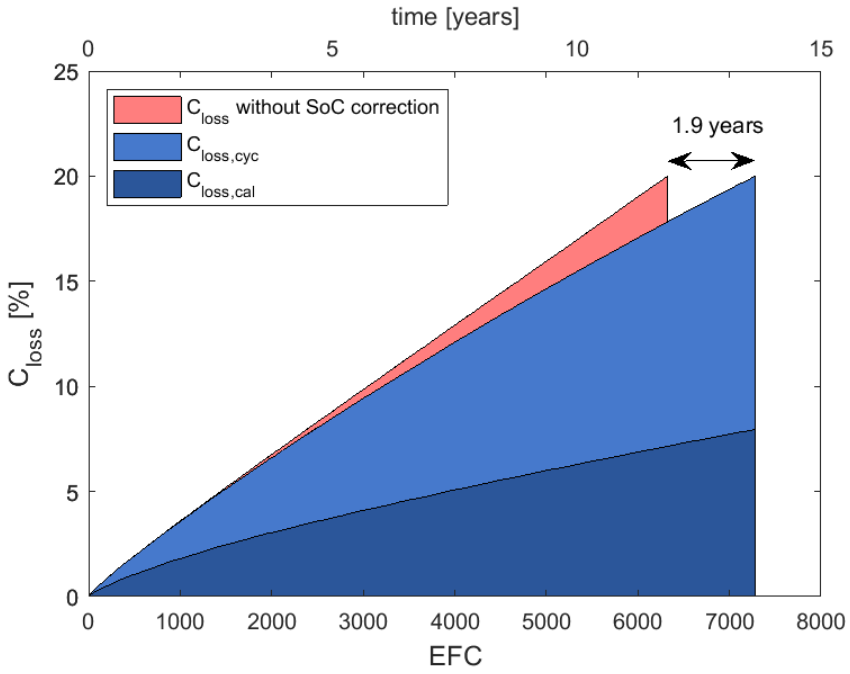

Figure 5.6: Modeled capacity loss at 90% target SoE, a system dimension of 0.5 Wh/W and normal deadband use over the time and number of EFC. The share of calendar and cyclic aging is marked. The overall model result without anode SoC correction is compared.

the respective aging models. In the calendar aging parameterization, the influence of the anode overhang was not modeled separately. It was described within the overall time dependence $t^{0.79}$. This may lead to an underestimation of the long-term capacity loss. At maximum, an increase of the time power factor to 1 is expected for the calendar SEI growth aging mechanism [40]. The possible underestimated capacity loss of calendar aging would be compensated in the cyclic aging model parameterization on data corrected by the modeled calendar capacity loss. This could lead to a shift in cyclic and calendar aging proportions. Even with this correction, LLI due to cyclic aging significantly contributes to the total capacity loss and should also be considered in future aging models. The capacity loss due to cracking in the active material is negligible in the case of FCR operation [15, 36, 37].

Considering the anode SoC instead of the battery SoC in aging modeling using Eq. (5.6) has a significant influence on the capacity loss results (Fig. 5.6). In the considered example case, a 1.9-year longer lifetime is predicted using the anode SoC. Without the correction, the cell ages faster because the anode SoC is still assumed to be high despite the occurring LLI. This amplifies the modeled calendar and cyclic aging. The huge lifetime difference underlines the importance of considering the

SoC correction.

Operating strategy dependence

Figures 5.7a and 5.7b show the modeled battery lifetime over target SoE and battery dimension with and without deadband use. With a larger system dimension, the battery lifetime increases. In a larger system, less power is demanded from each battery cell, reducing currents and DoD contributing to capacity loss in FCR operation. Furthermore, the operating range of the storage is extended to lower battery SoE, where aging is reduced. A lifetime minimum is reached at approximately 80% target SoE. This can be explained by the SoC dependency of the calendar and cyclic aging mechanisms at the graphite anode. At increased anode SoC above 80%, the mechanical stress on the anode active material and the SEI formed on it decreases because lithium-ions already occupy almost all graphite planes, and less volume change occurs during lithiation. Consequently, capacity loss due to cracking and reforming of the SEI decreases. This effect is reduced but not compensated by the increased chemical SEI reaction kinetics at higher anode SoC [15]. It should be noted that these are specific results of the model parameterization on the NMC cells considered. These showed a slight flattening of the capacity loss at higher SoC in calendar aging, which may be due to influences of cathode side reactions [14]. These were not described separately in the model relating to the graphite anode. The qualitative lifetime results are listed in Table 5.3.

Figure 5.7b visualizes the influence of deadband usage on lifetime. Deadband utilization causes a higher battery rest time and better maintenance of the target SoE (see subsection 5.5.1). The resulting change in lifetime is only small. At medium target SoE, the three surfaces defined by the different deadband strategies nearly overlap. The lifetime change with the SoE10Db strategy is also minimal for all other operating cases. At 90% target SoE, the strategy reduces the battery lifetime by up to 0.35 years. On the other hand, lifetime gains of up to 0.30 years are modeled at 50% target SoE. With the NormDb strategy, the lifetime increases by up to one year at high and low target SoE. This can be explained by better maintaining the border SoE, at which operating is particularly advantageous for the battery lifetime.

5.5.3 NPV analysis

Figure 5.8a shows the lifetime NPV depending on the system dimension for all considered target SoE. With a larger dimension, the NPV decreases due to higher PtH

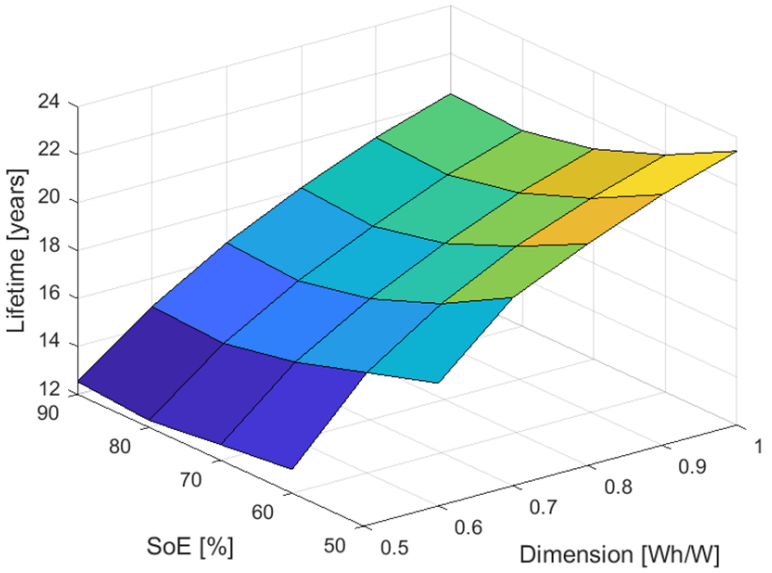

(a)

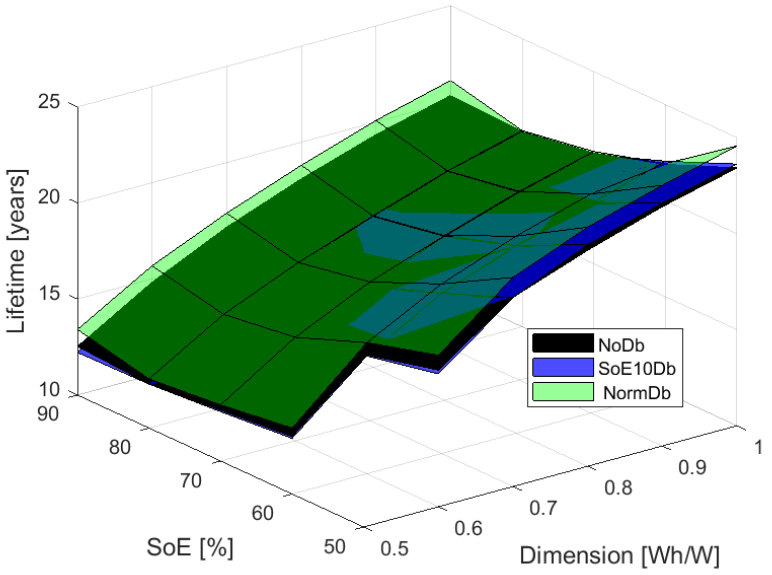

(b)

Figure 5.7: Battery lifetime over target SoE and battery dimensioning (a) without deadband DoF use (NoDb) (b) for different deadband strategies.

investment costs and lower FCR revenues. For high target SoE, neither the reduction in the number of OPAs and PtH module utilization time associated with larger dimensioning nor the additional FCR gains from extended battery lifetime compensate for these increasing costs. For low target SoE ($\leq$ 60% SoE), the maximum NPV is reached at a system dimension of 0.6 Wh/W. Especially at low SoE, the number of OPAs increases at smaller system dimensions, which causes rising recharging costs. Furthermore, profitability sinks for systems with smaller dimensions because of a lower battery lifetime. This complements the results of Schlachter et al. [13], who achieved an optimal hybrid system operation NPV at system dimensions smaller than 0.5 Wh/W without considering battery aging.
Figure 5.8b shows the NPV SoE dependency for different system dimensions. With a lower target SoE, the NPV increases for system dimensions bigger than 0.6 Wh/W. This is due to the reduced use of the PtH module, which is highly burdened with TLC. Furthermore, the battery lifetime increases below 80% SoE, which means the system can longer generate revenues by providing FCR. For smaller system dimensions, the NPV decreases towards 50% SoE and increases towards 90% SoE. The increased number of OPAs at small system dimensions and low target SoE causes that NPV decrease, especially considering the high electricity prices in 2021. The increase towards 90% SoE is attributable to the reduced number of recharges and the increased battery lifetime above 80% SoE. Without deadband use, the highest NPV result is achieved at 60% target SoE and a system dimension of 0.6 Wh/W.

The impact of the deadband strategies on NPV is shown in Figure 5.8c. The SoE10Db strategy has a negligible effect on the NPV results. The green peaks of the NPV bars show that the highest NPV can be obtained for all operating cases using the NormDb strategy. The highest NPVs are achieved for the 90% SoE and dimension 0.5 Wh/W operating strategy with 18.58 million euro and the 60% SoE and dimension 0.6 Wh/W operating strategy with 17.90 million euro. The strong increase in the NPV result at 90% SoE is mainly attributed to the higher battery lifetime due to normal deadband utilization. Because of this, the 90% SoE, dimension 0.5 Wh/W strategy surpasses the SoE 60%, dimension 0.6 Wh/W operation, which achieved the maximum NPV without considering deadband utilization. Again, it must be pointed out that the increase in battery lifetime over 80% SoC is a characteristic of the considered NMC battery cells and cannot necessarily be transferred to other battery cell chemistries.

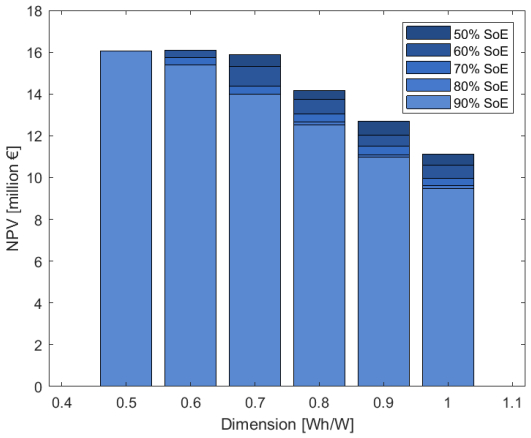

(a)

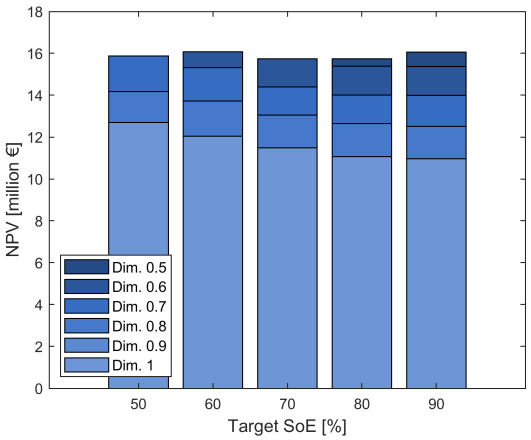

(b)

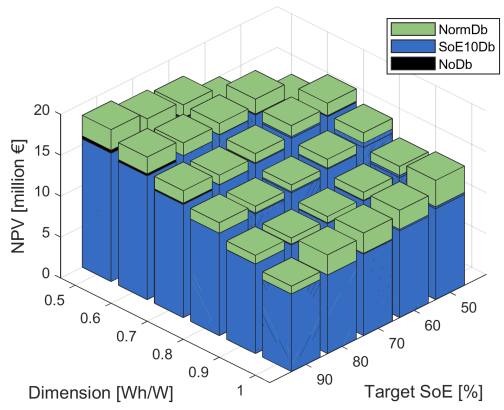

(c)

Figure 5.8: NPV over (a) the system dimension at different target SoE (b) the target SoE at different system dimensions without deadband utilization. (c) NPV over target SoE and dimension for different deadband DoF strategies.

5.5.4 Sensitivity Analysis

PtH module taxation, FCR price, recharging costs, and battery lifetime are essential factors determining the hybrid system's profitability. This publication focuses on considering battery lifetime in evaluating the most profitable battery operation. An open question is how much battery lifetime gain contributes to system profitability today and in future scenarios. To address this question, a two-step, one-factor-at-a-time sensitivity analysis is performed. The sensitivity of the NPV results to battery lifetime is investigated in three scenarios

1. fewer PtH TLC,
2. increased recharging costs,
3. lower FCR prices.

In the first step, the chosen scenario parameter is varied by 50%. In the second step, the NPV change under 50% increased battery life is determined. As a reference, the highest NPV operating strategy with 90% SoE, system dimension 0.5 Wh/W, and normal deadband utilization is chosen. Table 5.4 shows the corresponding results.

Scenario	NPV [million €]	NPV change with lifetime ↑ [million €]
Reference	18.58	8.73
PtH TLC ↓	20.33	9.13
FCR prices ↓	-1.71	2.50
Recharge costs ↑	16.76	7.90

Table 5.4: Sensitivity analysis results for the reference operating case 90% target SoE, dimension 0.5 Wh/W, and normal deadband use. Each parameter was varied by 50%; ↑ and ↓ indicate whether it has been raised or lowered.

The more the NPV changes with a parameter, the higher its sensitivity for it is. In the literature, a strong NPV dependence on the FCR price has already been determined [4, 12]. The NPV results confirm this. In the lower FCR prices scenario, the NPV rapidly decreases, and the system no longer amortizes. Recharge costs have a minor impact on NPV, closely followed by PtH TLC. However, the weighting of these factors shifts depending on the selected target SoE. Battery lifetime extension increases the NPV in each Scenario. With almost nine million euro NPV increase, the impact of an increased lifetime is significantly higher than that of changed PtH TLC and recharge costs. Therefore, at the considered high FCR price, battery lifetime is the most important influencing factor. In the case of reduced FCR prices the effect of an increased lifetime on NPV strongly decreases. The system can be operated longer, but the costs almost completely outweigh the additional profit. Therefore, FCR

prices are the most critical factor for system rentability. At low FCR prices, lifetime loses relevance compared to operating costs. At high FCR prices, it is crucial to optimize battery lifetime to increase the system profitability.

5.6 Conclusion

This study economically assessed the impact of the operating strategy and dimension of a hybrid system consisting of a lithium-ion battery storage coupled with a PtH module. The operating strategies included different battery target SoE and using the deadband DoF. Deadband utilization was considered in two strategies: normal deadband utilization (NormDb) and deadband utilization beyond the range of 10% SoE around the target SoE (SoE10Db). The analysis consisted of three steps: FCR load profile modeling, battery aging modeling, and NPV analysis. A focus was set on reliable aging modeling. The used semi-empirical aging model describing graphite anode aging mechanisms was introduced by Krupp et al. [14, 15]. It was extended by a method to calculate the anode SoC considering the aging modes causing capacity loss. Using the anode SoC instead of the battery SoC in aging modeling caused a huge predicted lifetime difference of up to two years.

The modeled power profiles were evaluated regarding the number of OPAs, PtH module usage time, and battery rest time. The closer the respective target SoE was to the upper or lower battery energy limit, the more frequently the PtH module was used or the battery was recharged. These effects were amplified for smaller system dimensions since the corresponding energy limits were reached more quickly. Deadband utilization caused a higher battery rest time and better maintenance of the target SoE.
Battery lifetime generally increases with bigger system dimensions and lower target SoE. The lifetime SoE dependency had a minimum at 80% SoE, which was attributed to the interaction of mechanical and chemical stress on SEI formation in the examined NMC cells aging model parametrization. Deadband usage had only little effect on battery lifetime. With the NormDb strategy, a lifetime gain of up to one year was reached at high and low target SoE.

The highest NPV results were achieved for smaller system dimensions. Without considering deadband utilization, the highest NPV is reached with 60% target SoE and a system dimension of 0.6 Wh/W. With too small system dimensions, the increased costs due to more use of the PtH module, more OPAs, and reduced battery lifetime outweigh the increased FCR revenues. Normal deadband usage

achieves the highest NPV in each operating case. Due to the positive impact of the NormDb strategy on battery lifetime at high SoE, the 90% SoE, dimension 0.5 Wh/W configuration reaches the highest NPV here. Deadband usage thus supports the advantageous hybrid system's operating strategy, where the battery is operated at high SoE and can therefore be dimensioned smaller.

In a sensitivity analysis, the FCR price was confirmed as the most important parameter influencing system profitability. For low FCR prices, the PtH TLC, recharge costs and battery lifetime have a comparable impact on NPV. Currently, PtH TLC overweight the profit from district heating, which inhibits the use of innovative sector-coupling operating strategies. In a market with high FCR prices, battery lifetime is the most important parameter. It is therefore essential to consider battery aging when optimizing the system's operation.

The results of the study refer to NMC cells of the HyReK 2.0 project battery storage. The detected increased lifetime at high SoC was modeled by anode aging mechanisms, but might additionally be caused by cathode side reactions. It is therefore not necessarily transferable to other graphite-based battery cells. Extending the aging model by the influence of different cathode reactions on capacity loss and including possible changing long-term aging behavior is a future task.

Author Contributions

Amelie Krupp: Main author of manuscript. Conceptualization, Methodology, Software, Validation, Formal analysis, Investigation, Data Curation, Visualization, Writing - Original Draft, Writing - Review and Editing, *Robert Beckmann*: Conceptualization, Methodology, Software, Formal analysis, Supervision, Writing - Original Draft, Writing - Review and Editing, *Patrick Draheim*: Conceptualization, Methodology, Data Curation, Writing - Review and Editing, *Eva Meschede*: Conceptualization, Methodology, Writing - Review and Editing, *Ernst Ferg*: Conceptualization, Methodology, Supervision, Writing - Review and Editing, *Frank Schuldt*: Conceptualization, Resources, Supervision, Writing - Review and Editing, Funding acquisition, *Carsten Agert*: Conceptualization, Resources, Supervision, Writing - Review and Editing

Acknowledgments

The results were generated in the framework of the project HyReK 2.0 (grant no. 03ET6147C). We thank the German Federal Ministry for Economic Affairs and Climate Action (BMWK) for funding.

References

[1] European Parliament. *Regulation (EU) 2021/1119 of the European Parliament and of the Council of 30 June 2021 establishing the framework for achieving climate neutrality and amending Regulations (EC) No 401/2009 and (EU) 2018/1999 ('European Climate Law')*. 2021. URL: https://eur-lex.europa.eu/legal-content/EN/TXT/?uri=CELEX:32021R1119 (visited on 10/21/2022).

[2] Katrin Schmietendorf, Joachim Peinke, and Oliver Kamps. "The impact of turbulent renewable energy production on power grid stability and quality". In: *The European Physical Journal B* 90.11 (2017). ISSN: 1434-6028. DOI: 10.1140/epjb/e2017-80352-8.

[3] Jan Figgener et al. "The development of stationary battery storage systems in Germany – A market review". In: *Journal of Energy Storage* 29 (2020), p. 101153. ISSN: 2352152X. DOI: 10.1016/j.est.2019.101153.

[4] Johannes Fleer et al. "Techno-economic evaluation of battery energy storage systems on the primary control reserve market under consideration of price trends and bidding strategies". In: *Journal of Energy Storage* 17 (2018), pp. 345–356. ISSN: 2352152X. DOI: 10.1016/j.est.2018.03.008.

[5] Tjark Thien et al. "Real-world operating strategy and sensitivity analysis of frequency containment reserve provision with battery energy storage systems in the german market". In: *Journal of Energy Storage* 13 (2017), pp. 143–163. ISSN: 2352152X. DOI: 10.1016/j.est.2017.06.012.

[6] Egill Thorbergsson, Vaclav Knap, Maciej Jozef Swierczynski, Daniel Ioan Stroe, Remus Teodorescu. "Primary Frequency Regulation with Li-Ion Battery Energy Storage System - Evaluation and Comparison of Different Control Strategies". In: *35th International Telecommunications Energy Conference 'Smart Power and Efficiency', INTELEC 2013* (2013).

[7] Maciej Swierczynski et al. "Primary frequency regulation with Li-ion battery energy storage system: A case study for Denmark". In: *2013 IEEE ECCE Asia Downunder*. IEEE, 3.06.2013 - 06.06.2013, pp. 487–492. ISBN: 978-1-4799-0482-2. DOI: 10.1109/ECCE-Asia.2013.6579141.

[8] Poria Hasanpor Divshali and Corentin Evens. "Optimum Operation of Battery Storage System in Frequency Containment Reserves Markets". In: *IEEE Transactions on Smart Grid* 11.6 (2020), pp. 4906–4915. ISSN: 1949-3053. DOI: 10.1109/TSG.2020.2997924.

[9] S. P. Melo et al. “Primary frequency control provided by hybrid battery storage and power-to-heat system”. In: *Applied Energy* 233-234 (2019), pp. 220–231. ISSN: 03062619. DOI: 10.1016/j.apenergy.2018.09.177.

[10] Jeanette Münderlein et al. “Optimization of a hybrid storage system and evaluation of operation strategies”. In: *International Journal of Electrical Power & Energy Systems* 119 (2020), p. 105887. ISSN: 01420615. DOI: 10.1016/j.ijepes.2020.105887.

[11] Julien Jomaux, Thomas Mercier, and Emmanuel de Jaeger. “Provision of frequency containment reserves with batteries and power-to-heat”. In: *2017 IEEE Manchester PowerTech*. IEEE, 18.06.2017 - 22.06.2017, pp. 1–6. ISBN: 978-1-5090-4237-1. DOI: 10.1109/PTC.2017.7980915.

[12] Patrick Draheim et al. “Business case analysis of hybrid systems consisting of battery storage and power-to-heat on the German energy market”. In: *Utilities Policy* 67 (2020), p. 101110. ISSN: 09571787. DOI: 10.1016/j.jup.2020.101110.

[13] Uli Schlachter et al. “Optimised capacity and operating strategy for providing frequency containment reserve with batteries and power-to-heat”. In: *Journal of Energy Storage* 32 (2020), p. 101964. ISSN: 2352152X. DOI: 10.1016/j.est.2020.101964.

[14] Amelie Krupp et al. “Calendar aging model for lithium-ion batteries considering the influence of cell characterization”. In: *Journal of Energy Storage* 45 (2022), p. 103506. ISSN: 2352152X. DOI: 10.1016/j.est.2021.103506.

[15] Amelie Krupp et al. “Semi-empirical cyclic aging model for stationary storages based on graphite anode aging mechanisms”. In: *Journal of Power Sources* 561 (2023), p. 232721. ISSN: 03787753. DOI: 10.1016/j.jpowsour.2023.232721.

[16] A. G. Stadtwerke Bremen. *SWB HYREK*. 2019. URL: https://www.swb.de/ueber-swb/unternehmen/nachhaltigkeit/hyrek (visited on 10/21/2022).

[17] ENTSO-E. *Frequency Containment Reserves: Information Page*. URL: https://www.entsoe.eu/network_codes/eb/fcr/ (visited on 10/21/2022).

[18] Dogan Keles and Hasan Ümitcan Yilmaz. “Decarbonisation through coal phase-out in Germany and Europe — Impact on Emissions, electricity prices and power production”. In: *Energy Policy* 141 (2020), p. 111472. ISSN: 03014215. DOI: 10.1016/j.enpol.2020.111472.

[19] Dmitriy O. Afanasyev, Elena A. Fedorova, and Evgeniy V. Gilenko. “The fundamental drivers of electricity price: a multi-scale adaptive regression analysis”. In: *Empirical Economics* 60.4 (2021), pp. 1913–1938. ISSN: 0377-7332. DOI: 10.1007/s00181-020-01825-3.

[20] Sanjeev Kumar Aggarwal, Lalit Mohan Saini, and Ashwani Kumar. “Electricity price forecasting in deregulated markets: A review and evaluation”. In: *International Journal of Electrical Power & Energy Systems* 31.1 (2009), pp. 13–22. ISSN: 01420615. DOI: 10.1016/j.ijepes.2008.09.003.

[21] Jan Figgener et al. “The influence of frequency containment reserve flexibilization on the economics of electric vehicle fleet operation”. In: *Journal of Energy Storage* 53 (2022), p. 105138. ISSN: 2352152X. DOI: 10.1016/j.est.2022.105138.

[22] The German Transmission Grid Operators, Regelleistung.net. *Datencenter, 2022*. URL: from:https://www.regelleistung.net/apps/datacenter/tenders/? (visited on 10/21/2022).

[23] European Energy Exchange AG. *KWK Index: Electricity price*. 4.10.2022. URL: https://www.eex.com/en/market-data/power/kwk-index (visited on 10/21/2022).

[24] German TSOs. *Präqualifikationsverfahren für Regelreserveanbieter (FCR, aFRR, mFRR)*. 3.06.2022. URL: https://pq-portal.energy/Download (visited on 10/21/2022).

[25] Alena Worschech et al. “Analysis of taxation and framework conditions for hybrid power plants consisting of battery storage and power-to-heat providing frequency containment reserve in selected European countries”. In: *Energy Strategy Reviews* 38 (2021), p. 100744. ISSN: 2211467X. DOI: 10.1016/j.esr.2021.100744.

[26] *Stromsteuergesetz (StromStG) vom 24. März 1999 (BGBl. I S. 378; 2000 I S. 147), das zuletzt durch Artikel 6 des Gesetzes vom 30. März 2021 (BGBl. I S. 607) geändert worden ist*. URL: https://www.gesetze-im-internet.de/stromstg/__3.html (visited on 10/21/2022).

[27] Wesernetz Bremen GmbH. *Preisblatt Netznutzung Strom: gültig ab 01.01.2022*. 21.10.2022. URL: https://www.wesernetz.de/geschaeftspartner/energielieferanten/stromnetz/entgelte-hb-bhv.

[28] *Erneuerbare-Energien-Gesetz vom 21. Juli 2014 (BGBl. I S. 1066), das zuletzt durch Artikel 4 des Gesetzes vom 20. Juli 2022 (BGBl. I S. 1353) geändert worden ist*. URL: https://www.gesetze-im-internet.de/eeg_2014/BJNR106610014.html (visited on 10/21/2022).

[29] *§ 19 StromNEV-Umlage*. URL: https://www.netztransparenz.de/EnWG/-19-StromNEV-Umlage/-19-StromNEV-Umlagen-Uebersicht (visited on 10/21/2022).

[30] *Abschaltbare Lasten-Umlage*. URL: https://www.netztransparenz.de/EnWG/Abschaltbare-Lasten-Umlage/Abschaltbare-Lasten-Umlagen-Uebersicht (visited on 10/21/2022).

[31] *Offshore-Netzumlage*. URL: https://www.netztransparenz.de/EnWG/Umlage-17f-EnWG (visited on 10/21/2022).

[32] *Konzessionsabgabenverordnung vom 9. Januar 1992 (BGBl. I S. 12, 407), die zuletzt durch Artikel 3 Absatz 4 der Verordnung vom 1. November 2006 (BGBl. I S. 2477) geändert worden ist*. URL: https://www.gesetze-im-internet.de/kav/BJNR000120992.html (visited on 10/21/2022).

[33] *KWKG-Umlage*. URL: https://www.netztransparenz.de/KWKG/KWKG-Umlagen-Uebersicht.

[34] Christoph R. Birkl et al. "Degradation diagnostics for lithium ion cells". In: *Journal of Power Sources* 341 (2017), pp. 373–386. ISSN: 03787753. DOI: 10.1016/j.jpowsour.2016.12.011.

[35] Matthieu Dubarry, Cyril Truchot, and Bor Yann Liaw. "Synthesize battery degradation modes via a diagnostic and prognostic model". In: *Electrochemical and Solid-State Letters* 219 (2012), pp. 204–216. ISSN: 0378-7753. DOI: 10.1016/j.jpowsour.2012.07.016.

[36] Mark Elliott et al. "Degradation of electric vehicle lithium-ion batteries in electricity grid services". In: *Journal of Energy Storage* 32 (2020), p. 101873. ISSN: 2352152X. DOI: 10.1016/j.est.2020.101873.

[37] S. G. Leonardi et al. "Investigation on the ageing mechanism for a lithium-ion cell under accelerated tests: The case of primary frequency regulation service". In: *Journal of Energy Storage* 41 (2021), p. 102904. ISSN: 2352152X. DOI: 10.1016/j.est.2021.102904.

[38] E. Thorbergsson, V. Knap, M. Swierczynski, D. Stroe and R. Teodorescu. "Primary Frequency Regulation with Li-Ion Battery Based Energy Storage System - Evaluation and Comparison of Different Control Strategies". In: *Intelec 2013; 35th International Telecommunications Energy Conference, SMART POWER AND EFFICIENCY* (2013), pp. 1–6.

[39] Kevin Jacqué et al. "The influence of frequency containment reserve on the cycles of a hybrid stationary large-scale storage system". In: *Journal of Energy Storage* 52 (2022), p. 105040. ISSN: 2352152X. DOI: 10.1016/j.est.2022.105040.

[40] Lars von Kolzenberg, Arnulf Latz, and Birger Horstmann. “Solid-Electrolyte Interphase During Battery Cycling: Theory of Growth Regimes”. In: *cssc* (2020). DOI: 10.1002/cssc.202000867.

6 Conclusion

Battery aging modeling is an important area of research that aims to predict and understand the decline in battery performance over time. It is essential to develop more efficient and reliable batteries, improve their safety, and optimize their usage. The complexity of the battery cell-specific electrochemical processes that depend on the application-specific aging conditions makes it challenging to develop accurate aging models. To address these challenges, scientists developed empirical and physics-based models for different purposes. While detailed physical-electrochemical models are well suited for understanding microscopic cell effects on short timescales, hybrid semi-empirical models are well suited for lifetime modeling. The current semi-empirical models still show potential for development in terms of efficient parameterization, extrapolatory, and transferability. Therefore, in this work, a new holistic semi-empirical aging model was developed to describe important graphite anode aging mechanisms. A focus was on developing innovative parameterization methods to reduce the measurement effort and increase the model accuracy. The model was parameterized on aging measurement data from NMC lithium-ion battery cells and finally used to economically assess the profitability of a sector-coupling FCR system considering battery lifetime.

The economic analysis included load profile simulation, aging modeling, and net present value calculation. The considered load profiles were characterized by the set system dimensioning, the battery storage target SoE and the deadband degree of freedom strategy used in the FCR provision. Although battery life was confirmed as a key influencing factor for system profitability, higher rentability was not accompanied by a longer battery lifetime in all operation cases. Under normal deadband utilization, the highest NPV was achieved at 90% target SoE and a system dimension of 0.5 Wh/W. The suitability of this operating strategy results from the nature of the sector-coupled system consisting of a battery and a power-to-heat module. Since the PtH-module can absorb energy at any time, the battery can operate at high SoE and be sized smaller, which reduces the investment cost. The comprehensive economic analysis confirmed the suitability of this strategy for the NMC battery cells considered, despite accelerated battery aging at high SoE. When applying this operating strategy, it must be considered that the effect of the high battery SoE on

aging could only be evaluated over part of the battery lifetime within the scope of this thesis. The 60% target SoE and dimension 0.6 Wh/W operating strategy achieved the second-highest NPV results and is associated with fewer risks in long-term aging. The following summarizes the features and development potentials of the introduced aging model.

In the developed aging model, the independently described calendar and cyclic capacity loss were superimposed. The calendar aging model considers the aging mechanism SEI growth during rest at different SoC and temperatures. In the model parameterization, a focus was set on evaluating and explaining the capacity loss caused by the regular characterization measurement performed in the aging test series. An initial capacity gain due to a decrease in internal cell resistance was observed, which can be explained by crack formation and restructuring of the active material during cyclization in characterization. It was accounted for in the model parameterization by correcting the measured capacity loss data by the capacity loss from a periodic characterization measurement. The corrected measurement data showed a typical root-shaped capacity loss in the first nine months of aging. Afterwards an accelerated capacity loss, especially at high SoC was observes, which might be caused by cathode side reactions. The introduced method to quantify and include the characterization effect in the model parameterization contributes to more reliable lifetime modeling considering only the actual battery aging.

The cyclic aging model describes the aging mechanisms SEI cracking and reforming and active anode material cracking considering the stress factors DoD, average SoC, current rate, and temperature. A model parameterization method was defined, which includes two parametrization stages on selectively chosen cyclic aging measurement data. Using ICA, the aging modes contributing to the loss of capacity were evaluated, distinguishing between LLI and additional LAM occurring. SEI cracking and reforming is connected to LLI. Therefore, only measurements in which predominant LLI was identified were used to parameterize the associated model equations. Measurements with visible additional LAM were used to parameterize the model equations describing cracking in the active material. The selective parameterization allowed a clear separation of stress factor sensitivities of individual aging mechanisms and thus contributed to the increased extrapolation capability of the model. An example of different stress factor sensitivities was that the NMC battery aging test series confirmed the negligibility of the current rate influence on SEI cracking and reforming. In contrast, a strong dependence of cracking in the active material on the current rate was found. The overall model could describe the nearly linear capacity loss caused by SEI growth, especially at cyclization with

small DoD, and the additional intense non-linear capacity loss when LAM starts to dominate at higher DoD and current rates.

To verify the transferability of the model results to batteries aged in application, the holistic model was validated on capacity loss data from a battery cell dynamically aged under FCR conditions. The modeled calendar and cyclic aging significantly contributed to the overall battery capacity loss. The long-term cyclic capacity loss might have been overestimated e.g. due to the different overhang effect considerations in the calendar and cyclic aging model. Nevertheless, the overall model described the summed capacity loss in the validation interval of about six months with a small absolute deviation of 0.2% capacity loss. Furthermore, the order of magnitude of lifetime and capacity loss predictions agreed with four-year long-term studies in the literature and own field measurements of the DLR HyReK 2.0 project.

In brief, this work contributed to the advancement and efficient parameterization of semi-empirical lithium-ion battery aging models and the operation strategy optimization of sector coupling FCR battery storages. The developed model can be applied to all graphite-based lithium-ion battery cells. Identified possible future works are described in the following outlook. The summary provides only a small insight into the challenges the scientific community faces to improve battery aging modeling. Anyway, with continued development, semi-empirical aging models have great potential to efficiently support the safe and optimized operation of battery systems today and in the future.

6.1 Outlook

Consideration of further stress factors and aging mechanisms

The presented model refers to graphite anode aging mechanisms. In the case of the used NMC battery, a flattening of the expected increase in capacity loss during calendar and cyclic aging at higher SoC was detected. This can be attributed to the influence of additional cathode side reactions. In this work, the impact of cathode effects on the capacity loss was indirectly considered in the model parameterization on empirical measurement data, but not modeled separately. Cathode side reactions should be described in independent model equations in the calendar and cyclic aging to further extend the model's extrapolation capability. Furthermore, the long-term effect of cathode reactions on battery aging needs to be studied in more detail.
Moreover, an extension of the presented model to consider stress factor ranges and

connected aging mechanisms occurring in more demanding applications is desirable. The stress factor ranges considered in this work's cyclic aging test series were specified based on typical load profiles of stationary FCR battery storage systems. This implies the assumption that the system is temperature-controlled, i.e., not subject to external temperature fluctuations. Furthermore, the batteries were symmetrically stressed in the cyclic aging analysis, i.e., no distinction was made between charging and discharging current rates. In mobile applications with fast charging requirements and fluctuating ambient temperature the model should be extended by the lithium plating aging mechanism. It occurs at battery charging, therefore a further differentiation of the charging and discharging current is reasonable. With consideration of further aging mechanisms, the presented parameterization method can also be extended. For example, intensive ICA can differentiate between LAM at the anode and cathode. Furthermore, additional characterization methods such as electrochemical impedance spectroscopy or relaxation measurements could be used to select relevant measurement data for parameterizing the aging mechanism model equations.

Battery long term aging

Modeling battery life is subject to significant uncertainties. Over the battery lifetime, the dominant aging mechanisms change depending on cell type and application load profile. This work found a change in the time and SoC dependence of the capacity loss in the first year of calendar aging. How it evolves over subsequent years could not be assessed on the existing data set. The capacity gain possibly caused by cathode reactions could turn into a rapid capacity loss at high battery SoC in the long term and therefore needs to be investigated in more detail. Furthermore, the main dynamic model validation was carried out on half a year of aging data. In battery aging modeling, there is a general need for long-term aging data for model parameterization, validation, and uncertainty quantification in lifetime prediction. Generating reliable long-term aging data (in the laboratory environment and from field measurements) and effectively making it available to the research community on a shared data platform is a current challenge and a subject of future research.

System effects

In this work, battery aging was measured and modeled at the cell level. The transfer to the system level was carried out assuming that all cells behave the same and no interconnection effects occur. Since the internal properties of interconnected cells always differ slightly, for example, unequal current distributions between cells connected in parallel occur. Furthermore, system characteristics such as module bracing, thermal interactions between individual cells and the cooling system, or the BMS balancing strategy influence battery aging. System effects coupled with cell-to-

cell variation lead to differing single-cell aging and a statistical distribution of cells at risk of failure in a system. Each further interconnection level is associated with its own thermal, electrical, and mechanical characteristics. Modeling approaches can thus become considerably complicated. Anyway, in the lifetime prognosis of battery systems, especially with high safety requirements, it is useful to consider system effects for a more reliable lifetime prognosis.

7 Appendix

7.1 List of publications

Publications in Peer-Reviewed Journals

Methodical basics presented in

* Amelie Krupp, Ernst Ferg, Frank Schuldt, Karen Derendorf, and Carsten Agert, Incremental Capacity Analysis as a State of Health Estimation Method for Lithium-Ion Battery Modules with Series-Connected Cells, *Batteries*, 2021, DOI:https://doi.org/10.3390/batteries7010002.

Scientific contribution dissertation in

1. Amelie Krupp, Robert Beckmann, Theys Diekmann, Ernst Ferg, Frank Schuldt, and Carsten Agert, Calendar aging model for lithium-ion batteries considering the influence of cell characterization, *Journal of Energy Storage*, 2022. DOI: https://doi.org/10.1016/j.est.2021.103506.

2. Amelie Krupp, Robert Beckmann, Theys Diekmann, Gerd Liebig, Ernst Ferg, Frank Schuldt, and Carsten Agert, Semi-empirical cyclic aging model for stationary storages based on graphite anode aging mechanisms, *Journal of Power Sources*, 2023, DOI: https://doi.org/10.1016/j.jpowsour.2023.232721.

3. Amelie Krupp, Robert Beckmann, Patrick Draheim, Eva Meschede, Ernst Ferg, Frank Schuldt, Carsten Agert, Operating strategy optimization considering battery aging for a sector coupling system providing frequency containment reserve, *submitted to the Journal of Energy Storage*, tbd.

Other Contributions

☆ Batteries Europe WG6 ST3, Amelie Krupp, Frank Schuldt, Antonios Marinopoulos, Maxime Montaru, Phuong Nguyen, Javier Olarte, Bernhard Fassler, Mika Kanninen, Luigi Lanuzza, Carlos Pueyo, Jesus Varela Sanz, and Matthias Vetter, ST3 Interoperable advanced BMS, 2021, *In Roadmap on Stationary Applications for Batteries*, Pages 25–27.

List of Figures

7.3 List of tables

List of Tables

Declaration

Erklärung gemäß § 12 der Promotionsordnung
Mit dieser Dissertation soll der Grad eines Doktors der Naturwissenschaften erlangt werden. Hiermit versichere ich, dass ich diese Arbeit selbstständig verfasst und keine anderen als die angegebenen Quellen und Hilfsmittel benutzt habe. Zudem erkläre ich hiermit, dass die vorliegende Dissertation bereits in Teilen veröffentlicht wurde, eine Liste der Publikationen ist dieser Dissertation angehängt. Diese Dissertation hat weder in ihrer Gesamtheit, noch in Teilen einer anderen wissenschaftlichen Hochschule zur Begutachtung in einem Promotionsverfahren vorgelegen, bzw. liegt einer anderen wissenschaftlichen Hochschule zur Begutachtung in einem Promotionsverfahren derzeit vor. Außerdem erkläre ich hiermit, dass die Leitlinien guter wissenschaftlicher Praxis an der Carl von Ossietzky Universität Oldenburg befolgt wurden, und im Zusammenhang mit dem Promotionsvorhaben keine kommerziellen Vermittlungs- oder Beratungsdienste (Promotionsberatung) in Anspruch genommen worden sind.

Oldenburg, den

Amelie Krupp